NORTHWESTERN UNIVERSITY

Nanoparticle Synthesis within Nanoreactor Templates and Their Applications

A DISSERTATION

SUBMITTED TO THE GRADUATE SCHOOL

IN PARTIAL FULFILLMENT OF THE REQUIREMENTS

for the degree

DOCTOR OF PHILOSOPHY

Field of Materials Science and Engineering

By

Liban Jibril

EVANSTON, ILLINOIS

June 2022

ABSTRACT

Nanoparticle Synthesis within Nanoreactor Templates and Their Applications

Liban Jibril

Nanotechnology research broadly encompasses the exploration of the unique chemical, optical, electronic, or biological properties of materials with dimensions < 1 μm. Inorganic nanoparticles are one such class of materials, with properties that are exceptionally sensitive to particle size and structure. This is especially evident in the field of heterogeneous chemical catalysis, where the surface of the material dictates the reaction outcome. However, synthesizing nanoparticles of a desired size, composition, or shape on demand is a persistent challenge, as conventional synthesis approaches often require extensive trial and error to synthesize the preferred particle product, assuming it is possible at all. This thesis introduces two nanoreactor-based strategies, that aim to push the limits of high-yield and modular particle synthesis compatible with chemical catalysis. It further aims to address challenges with measuring the reactivity of low areal-density polyelemental particles synthesized within nanoreactors, and in so doing, provide avenues towards high throughput screening of complex nanoparticle libraries.

Chapter One provides a comprehensive introduction to the state-of-the-art with regards to nanoparticle synthesis, and introduces the challenges associated therein. It further introduces the nanoreactor as a robust synthetic alternative, especially for applications in particle synthesis for rapid chemical catalyst discovery.

Chapter Two describes a method to synthesize nanoparticles by isolating small volumes of particle precursors within a nanohole reactor, followed by reductive annealing to yield site-isolated nanoparticles. The process described is materials-general and provides a significant degree of size-

control while maintaining monodispersity of the product population. Finally, it provides fundamental insight into the role of reactor geometry on the preferred final position of the particle products.

Chapter Three reports a solution-based nanoreactor synthesis scheme, which dramatically increases the throughput of particle synthesis. In this strategy, hollow silica shells are used to isolate and synthesize nanoparticles, and we discover via *ex situ*, *in situ*, and bulk-characterization strategies that polymer incorporation is key to a dramatic improvement in the yield of individual particles within each shell.

Chapter Four discusses strategies to address the challenge of probing gas-phase reactivity of a low particle-density planar catalyst. The challenge is separated into two steps, with this chapter focused on reactor cell design and testing. The chapter concludes with the proposal of a capillary tube-based strategy for locally screening a library of nanomaterials on a planar surface. Chapter Five describes gas-phase cryogenic distillation of product molecules as a worthwhile strategy to measure the reactivity of a small particle population. This strategy is used to selectively adsorb a hydrocarbon (1-butene) on an adsorbent powder, which can be detected by infrared spectroscopy.

Finally, Chapter Six provides an outlook on the field of nanoreactor templated nanoparticle synthesis and highlights several worthwhile future research directions.

Thesis Advisors: Profs. Chad A. Mirkin and Vinayak P. Dravid

ACKNOWLEDGMENTS

I thank my advisors, Professors Chad Mirkin and Vinayak P Dravid for their invaluable help over the course of my PhD. From Professor Mirkin I learned to never be satisfied with an empirical or phenomenological result, and to search for the fundamental reason or mechanism to explain my observations. I also learned from Chad a strict hypothesis-driven experimental style, and that academic talent is no substitute for hard work. From Professor Dravid, besides being a boundless source of electron microscopy wisdom, I learned enthusiasm in the face of adversity, the power of a strong network of colleagues, and what compassion in a professional setting looks like. For these lessons, I will be eternally grateful, and I hope to keep these ideas close to heart for the rest of my career and life.

I thank the other members of my committee, Professors Jiaxing Huang and Nathan Gianneschi, who each went out of their way to ensure they could serve at my defense. Their research careers are a source of inspiration, and I aspire to have a fraction of their professional success. I also thank the Mirkin and Dravid group office staff, including Drs. Sarah Petrosko, Tanushri Sengupta, Sara Rupich, Jenny Orbeck, as well as Elizabeth Forest, Pam Watson, Ruari McDonnell, and Lourdes Vasquez. Each of them helped me significantly, including coauthoring a manuscript in the case of Dr. Petrosko, and have significantly contributed to my PhD experience. I was fortunate to be mentored by a prolific scientist early in my PhD career, Dr. PengCheng Chen. I am excited to see what his independent research career entails, but I have no doubt that I wouldn't have achieved what I have without his support.

I thank my Northwestern University colleagues and friends. In particular, Drs. Rustin Golnabi, Eunbi Oh, Abha Gosavi as well as Donghoon Shin and Namrata Ramani who made for excellent office mates and close friends; I could not be luckier than to have landed in Ryan 2027 when I did.

We have diverged significantly in career direction (and soon physical location), but they were crucial protagonists in my PhD journey. Drs. Liliang Huang and Cindy Zheng have been great friends to me over the course of my PhD, with stellar careers ahead of them. Drs. Bo Shen and Minliang Lai were my friends before we began collaborating, and working with them has helped me understand how they became so successful as scientists. Matthew Cheng, my roommate, collaborator, and friend, has been crucial in helping maintain my sanity, I am grateful every day to have met him by blind luck during our MSE visit weekend in Spring 2017. Drs. Jordan Swisher, Selim Alayoglu, and Neil Schweitzer have been great sources of friendship, feedback and experimental wisdom, and I am grateful to each of them. I also acknowledge Drs. Yixin Wu, Xinpeng Zhang, James Hedrick, Ed Kluender, Maria Cabezas, as well as current students Carolin Wahl, Peter Winegar, Jungsoo Park, Nikhil Chellam, Alexa Wong, Zihao Ye, and Allen Guo for varied but significant academic and nonacademic support.

Prior to NU, I worked with a great team of researchers in the Lipomi group at UCSD. In particular, Professor Darren Lipomi has been one of my fiercest supporters, and his mentorship, friendship and encouragement are the key reason I pursued a PhD in the first place. Drs. Alex Zaretski, Adam Printz, Brandon Marin, Suchol Savagtrup, Daniel Rodriguez and Julian Ramirez were each responsible for building my confidence as a scientist, and in some part responsible for any academic achievements I have had since.

I acknowledge various friends who made the journey worthwhile, Kundiso Nyambirai, Deepal Patel, Neil Gandhi, Nathaniel Girma, Anamik Jhunjhunwala, Sam Dossou, Fernando Granizo, Sid Akkiraju, Anirudh Prabhakar, Ali Hamdok, Yutong Li, Norman Luu, Louis Wang, Chamille Lescott, Melissa Puga, Lucy Lee, Sri Suresh, Ruth Lee, Jann Grovogui, Tad Reese, Jeff Chen, and

Eden Aklile. I hope each of them recognizes how important they are to me, and if not, they can reach out for a reminder!

I thank my brothers, Dalmar and Hanad, and “brother-from-another-mother”, Peter Donahue. They each mean the world to me. I thank my aunts, uncles, and cousins, who have been a constant source of wisdom, affection, and kindness. They say it takes a village to raise a child, we certainly have the numbers to be called a village!

Finally, I thank my parents who sacrificed much to create opportunities for my brothers and me to thrive far away from their homeland in Somalia. They instilled in me my work ethic, taught me to enjoy academics, nurtured my love of science, taught me to trust my instincts, and prayed for me to achieve my goals. I would not have pursued this career without their love, guidance, and support, and having it made the journey sweeter. If they feel any pride from my accomplishment, it still does not begin to repay what they have given me. May Allah reward them in my stead.

DEDICATION

For my parents.

LIST OF FIGURES

LIST OF TABLES

CHAPTER ONE

Nanoreactors for Particle Synthesis

Portions of this chapter are based on work published in: Nat Rev Mater. **2022**. *Copyright 2022 Springer Nature.*

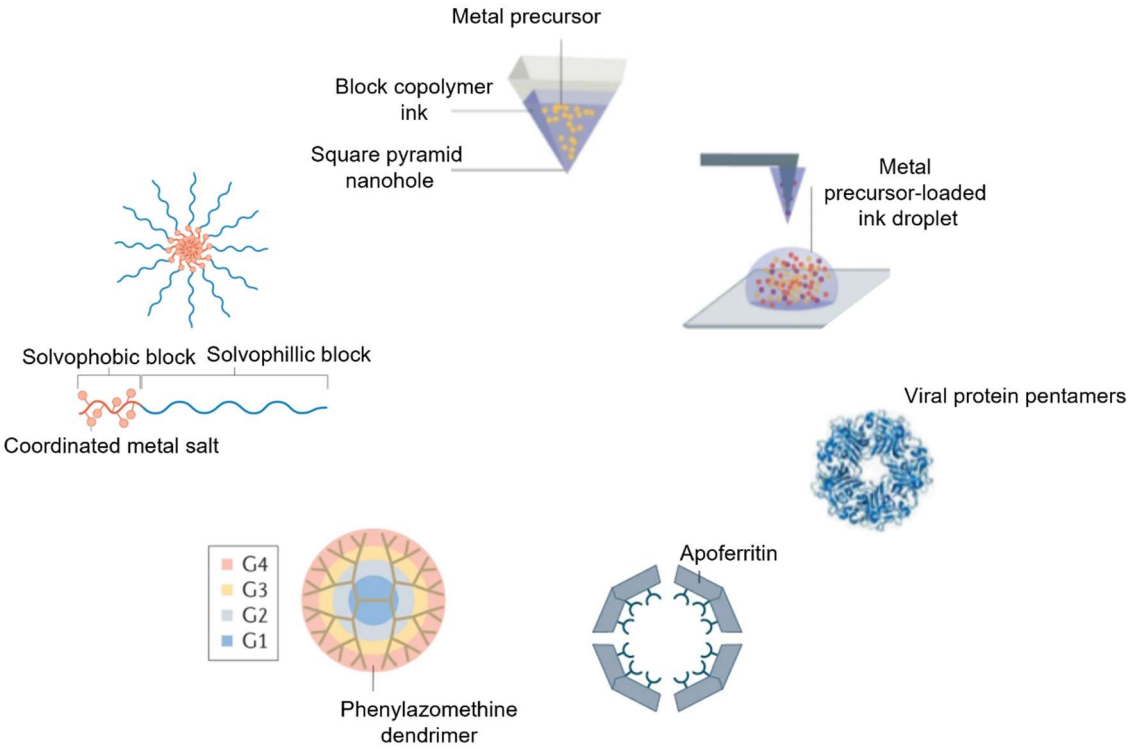

1.1 Motivation and Introduction

Nanoparticles are small clusters of atoms with dimensions between 1 nm – 1 μm. This class of materials have been utilized extensively over the course of human civilization, however the tools to image and understand the origin of their structure-function relationships only emerged in the 20th century. The pathway to reproducible synthesis and electron-microscopy examination of gold nanoparticles for example was demonstrated by Turkevich et al. in 1951.[1] In the range of relevant applications, chemical catalysts are an exciting frontier, due to the well documented discrepancy between the nano and bulk-scale catalytic properties of materials. An early key demonstration came from Haruta et al in 1987; in their seminal work, they demonstrated that oxidation of the exceptionally stable carbon monoxide molecule is possible on sub 10-nm gold particles, which was unheard of on macroscopic gold surfaces.[2] Today, chemical catalysis is a field of science crucial to numerous modern day technologies, facilitating in some shape or form as much as 80% or more of all industrial processes, ranging from chemical, petrochemical and biochemical to polymer and environmental protection processes (**Figure 1.1**).[3] The roughly 13 trillion dollar industry has continuous room for growth, due to the decreases in operating costs associated with improving catalyst performance, as well as a persistent trend towards more sustainable and environmentally friendly processes.[3,4]

In the practice of synthesizing industrially-relevant nanoparticle catalysts, several key performance metrics are: activity, selectivity, stability, cost (in manufacturing and raw materials), ease of recycling/reuse, and environmental and health hazard potential.[4,5] In this multivariate design space, incremental improvements in any of the listed performance metrics can translate to significant improvements to the economic feasibility of a given process. Indeed, it may render

reactions that were seemingly impossible accessible, such as the early demonstration of gasoline manufacture from coal or light alkanes by the Fischer-Tropsch reaction in the 20th century.[6]

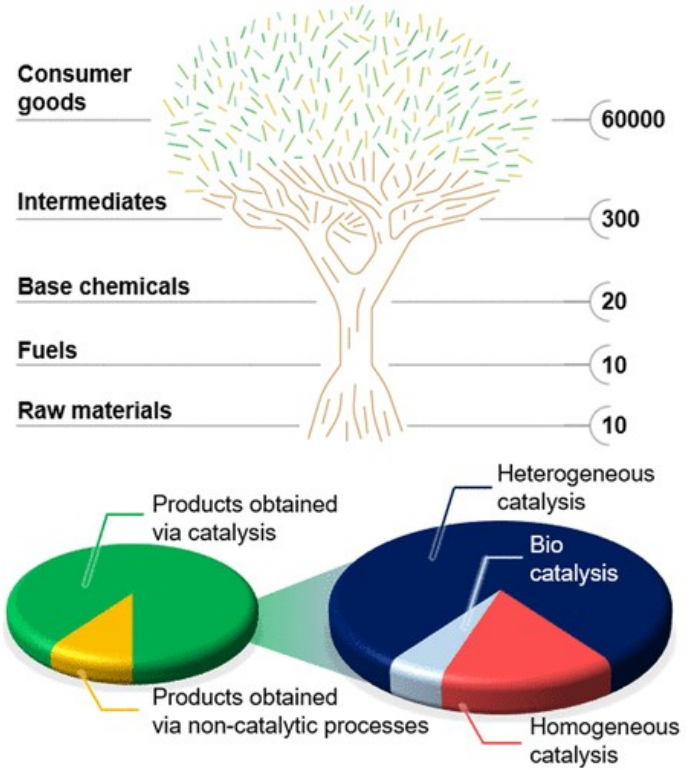

Figure 1.1: The landscape of chemical catalysis and its industrial relevance. Adapted from ref: [138]

Despite the significant improvements gained by utilizing nanoparticles in general, and complex nanoparticles in particular, several challenges prevent adopting particles synthesized in the lab practically in industry. Firstly, ensuring their stability under harsh typical reaction conditions, where many model catalysts fail.[7,8] Second, facile synthesis of multicomponent target structures, as traditional wet-chemistry approaches often require significant trial and error to achieve the desired size and stoichiometry due to fundamental differences in reduction kinetics between precursors.[9] Rapidly synthesizing target structures is crucial as the variety of performance metrics in heterogenous catalysis (conversion, selectivity, turnover frequency, long-term stability, recyclability, disposal, etc.) would otherwise make scaling-up untenable, and thus industrial

catalysts are biased towards simple active sites.[4] Finally, squeezing the distribution in size, composition, and crystal structure of the catalyst is key to facile identification of the relevant active sites, and porting knowledge from lab-scale to kg scale. Typically solution synthesized particles have an excellent size and composition distribution, but conventionally synthesized nanoparticle catalysts often do not (spray pyrolysis, bulk machining etc.)[10–12]

In this dissertation, I will describe how nanoreactors can work to significantly simplify the synthesis process for a desired particle product, and potentially bridge the gap between strategies preferred by chemists vs. those preferred by chemical engineers. Nanoreactors are simply confined templates that isolate reaction media with maximum dimensions < 1 μm.[13] The nanoreactor context provides significant means to improve the modularity of the nanoparticle synthesis, with fine-control over reaction outcomes. I will thus describe how nanoreactors may serve to not only allow access to monodisperse populations of particles hypothesized to have exceptional catalytic relevance, but also to accelerate the discovery process of exceptionally active materials.[13,14]

1.2 Nanoparticle Catalysis

The improvement in catalytic properties of a material with decreasing size are highly system specific, but can be generally attributed to several effects:[15–17] the increased surface area to volume ratio (**Figure 1.2A**), the accompanying increase in density of low-coordinated atoms, variation in the electron density/oxidation state, and/or assorted metal-support effects (i.e. 'strong metal-support interaction', SMSI).[4,18,19] Further, incorporation of 2+ elements in a single nanoparticle has been demonstrated to be a robust method of improving catalytic performance.[9,15] In this case, either alteration in the choice of exposed facets or fine tuning of the electron density at the particle

surface and subsequent abstraction of adsorbing molecules is responsible for the remarkable improvements in activity. This has been robustly demonstrated, for a variety of alloy nanoparticles and structures.[20–25]

In certain circumstances, the effects of nanoparticle alloying or fine-control over particle composition can be predicted. One notable example is with regards to the Sabatier principle that describes a scaling-relation observed in several heterogeneous catalysis systems.[26] In this plot, we observe that the reaction rate vs. bond strength of a molecule to the metal surface results in a characteristic 'volcano' shape (**Figure 1.2B**). This effect indicates that an intermediate binding strength to the metal surface is ideal to achieve high reactivity; too low results in no chemisorption, too high results in products being unable to dissociate. Researchers have accordingly attempted to take advantage of this scaling relation by combing less noble metals with the goal of engineering a surface with intermediate binding strength that can facilitate a high particle activity.[27,28] However broadly speaking, as particle composition becomes more complex, the relationship between its structure and properties becomes more difficult to predict as well. One example is the ammonia synthesis catalyst based on Fe particles, which often incorporates alkali metal promoters and a metal oxide support.[12] The complex interplay between these components has given rise to many fundamental studies to explain why this material performs so well, such as: the d-band energy shift (with respect to the Fermi level, **Figure 1.2C**), strong-metal support interactions and the effects of the peripheral atoms close to the support, hydrogen spillover, and sinter-resistance from the support.[29–32] Understanding these complex phenomena is highly challenging, and lends credence to the notion that rapid synthesis and testing may be a suitable means to short-circuit the decades of fundamental research necessary to explain a catalyst's exceptional performance comprehensively.

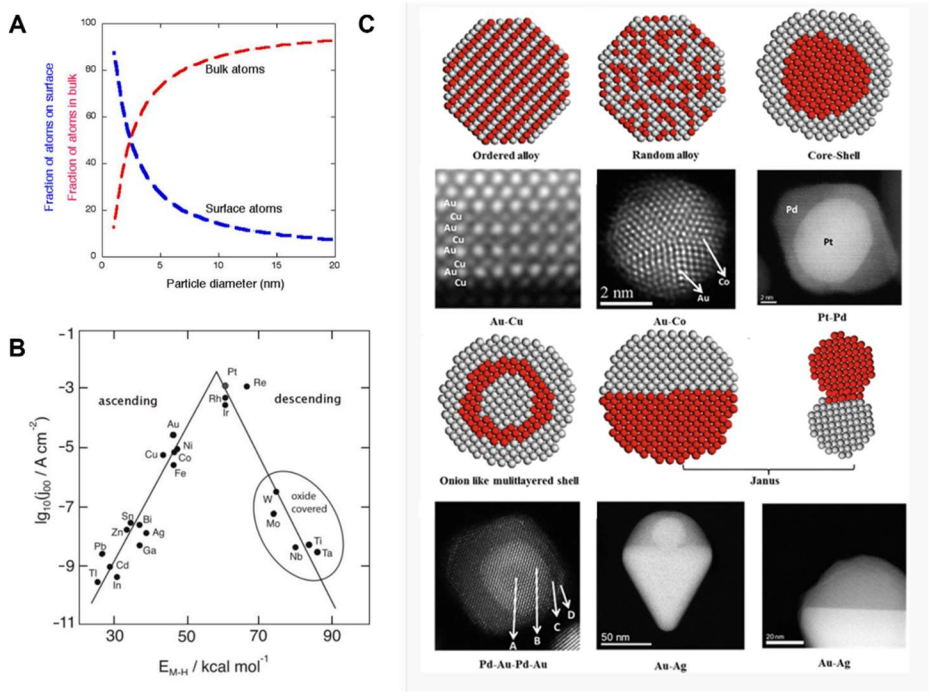

Figure 1.2: Particle size, composition and structure dictate reactivity. A) One feature that describes the particle size-dependence is the increasing ratio of surface to bulk atoms. B) A characteristic volcano plot describes the scaling relation between metal-adsorbate bond strength and reactivity, implying a maxima in activity at intermediate binding strength. C) Two component particle systems and some resultant structural motifs, each with unique effects on particle surface chemistry. Adapted from refs:[26,33]

1.3 Conventional Synthesis of Nanoparticles

The methods used to synthesize particles by researchers in the lab varies significantly from those used in industry.[4,32] In the nanoparticle synthesis research field, wet-chemistry approaches dominate, and enable access to exceptional improvements in particle size-control,[34,35] shape-control,[28,36] and composition control.[37–40] Solution phase nanoparticle synthesis typically relies upon three components: a metal precursor (i.e.$HAuCl_4$), a reducing agent (often $NaBH_4$, ascorbic acid, or hydrazine), and a stabilizing ligand (citrate, alkyl thiol, or more common recently cetyltrimethylammonium bromide (CTAB)).[41] Typically, the metal precursor is dissolved in an aqueous medium, and a reducing agent is incorporated either in the aqueous phase, or in a vigorously mixed organic phase with the help of a metal precursor phase-transfer catalyst (such as

tetraoctylammonium bromide (TOAB)).[41] Subsequent reduction results in nucleated metal particles which grow until an equilibrium size in which their surfaces are saturated with the stabilizing ligand, preventing further aggregation (**Figure 1.3**). The ligand stabilizer can operate either by electrostatic repulsion in the case of ionic surfactants such as $CTA^+ + Br^-$, or by steric hindrance with nonionic surfactants such as polyethylene glycol (PEG).[41] Based on these techniques, nanoparticles of most catalytically active transition metals have been synthesized, including but not limited to: Pt, Pd, Rh, Ru, Co, Ni, Fe, Au, etc.[32]

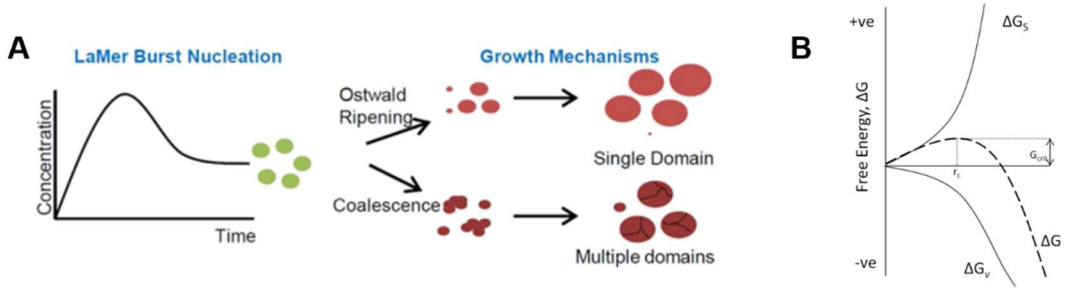

Figure 1.3: A) Schematic illustration of the mechanism of colloidal nanoparticle synthesis per the LaMer theory. Precursor salts are reduced and can result in single-crystal or polycrystalline particles depending on the subsequent growth mechanism. B) The free energy diagram describes the balance of bulk and surface free energies, the sum of which describe a critical nucleus over which nucleation is favored. Adapted from ref: [42]

Further, synthesis of alloys of these metals has similarly proceeded, by the co-precipitation technique, in which chemical reduction occurs either in tandem or in sequence.[41] For example, monodisperse 8 nm Co-Ni and Fe-Pt alloy nanoparticles have been demonstrated, and their crystallinity explored, representing a small fraction of the available catalytic composition space. [43] thermal decomposition or 'thermolysis', seed-mediated growth, or galvanic exchange. Thermolysis relies upon thermal decomposition of organometallic precursors, and controlled growth of the resultant particles.[41] An improved modularity can arise by utilizing bimetallic organometallic precursors, as demonstrated in various iterations for FePt nanoparticles from $Fe_3Pt_3(CO)_{15}$ for example, eliminating the need for extensive tuning of the reaction mixture.[44–46]

Seed-mediated growths consist of controlled nucleation of a single nanoparticle population, followed by either a) complete overgrowth, b) selective/facet-dependent growth or c) interpenetration of the second material.[47] This can give rise to core-shell, janus type, or alloy/intermetallic nanoparticles respectively. Yang and coworkers demonstrated an early iteration of this procedure to form core-shell nanoparticles of cubes, cuboctahedra, and octahedra.[48] These structures are catalytically fascinating in their own right, as the Xia group amongst others discovered that core-shell strain effects, as well as a large high-index facet density improves catalytic activity.[36,49,50] Finally, galvanic exchange is a powerful technique towards synthesizing a variety of structures inaccessible via conventional means, especially with respect to semiconductor nanoparticles.[51] The Schaak group in particular has demonstrated the power of these techniques to form a library of heterostructure nanoparticles of astounding complexity.[52,53] In this case, they rely upon cation exchange reactions, which are governed by solvation energy and Lewis acid-base interactions. By operating partial exchange reactions, only a fraction of the cations are replaced, resulting in a phase-segregated heterostructure of various metal sulfides. This can be repeated sequentially in assorted exchange solutions to prepare heterostructures of increasing complexity, with each exchange denoted by a generation number (i.e. first generation, 'G-1' was CuS) (**Figure 1.4**). This synthesis procedure offers significant improvements in modularity, as the newly exchanged cation occupies the position adjacent to the previously exchanged region, and hierarchical structures can be formed. However, this process is typically suited to forming custom heterostructures as opposed to alloy particles, as well as being focused on traditionally catalytically inactive materials. Finally, the high-temperature stability of the structures formed remains uninvestigated; multi-interfacial structures are known however to be severely kinetically trapped, implying use of these exciting structures under harsh reaction conditions would likely be difficult.

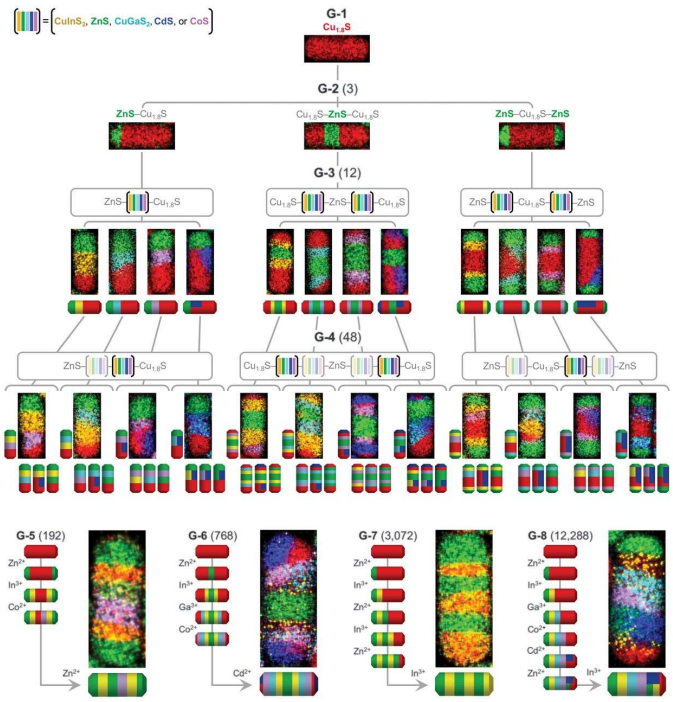

Figure 1.4: Synthetic pathways to 16,380 distinct G-3 through G-8 nanorods. Reaction diagram showing the pathways by which G-1 Cu1.8S nanorods can be transformed to 3 distinct G-2 ZnS/Cu1.8S derivatives, which can subsequently be transformed into assorted higher generation nanorods through various combinations of Zn2+, In3+, Ga3+, Co2+, and/or Cd2+ cation-exchange steps. STEM–EDS element maps, are shown for 28 of the 16,380 possible G-3 through G-8 members of this family. Drawings indicate the additional accessible G-4 nanorods, as well as pathways to selected G-5, G-6, G-7, and G-8 nanorods. STEM-EDS signals from the Cu Ka, Zn Ka, In La, Ga Ka, Co Ka, and Cd La lines are shown in red, green, yellow, teal, purple, and blue, respectively. Adapted from ref: [53]

As described previously, although the particles synthesized in this manner have exceptional control over reaction outcome and dispersity, they are often less stable under harsh reaction conditions, they are difficult to scale, and the surfaces are often covered with stabilizing ligands which ensure the particles are stable as a colloid, but also block the active sites for downstream catalysis.

In contrast, in industry, synthesis procedures such as incipient wetness impregnation, spray pyrolysis, and bulk machining[11,54] are common, that sacrifice fine-control over structure, in exchange for a particle product distribution which is robust and unlikely to change significantly during reaction conditions (perhaps after including an ‘activating’ calcination step for example).

This is reasonable, as an intermediate catalyst with long-term stability may often be preferrable to the processing steps associated with regenerating a high-performing catalyst more regularly.[4] The challenges therein, however, include the difficulty of understanding the evolution of the ensemble catalytic properties, as each particle and the active sites on its surface are unique. Further, while simple active sites are preferred in industry, it stands to reason that much of the fundamental research obtained on model complex particle catalysts may be translatable to industry. The question is: how?

1.4 Nanoreactor Templated Nanoparticle Synthesis

Nanoreactors are small reaction vessels with maximum dimensions in the nanometer range (sub-1-µm dimensions, yoctolitre to femtolitre volumes (10^{-24}–10^{-15} l)). They allow chemical reactions to occur within them while isolated from the surrounding environment and they can be used either to achieve large-scale chemical transformations or to template the synthesis of complex nanoparticles.[55] Nanoreactors have emerged as exceptional alternatives to traditional methods of synthesizing nanoparticles,[14] because their confined volumes provide an isolated space for particle nucleation and growth (**Figure 1.5**), where the morphology and chemical contents of the reactor and its subsequent processing dictate the final particle structure.

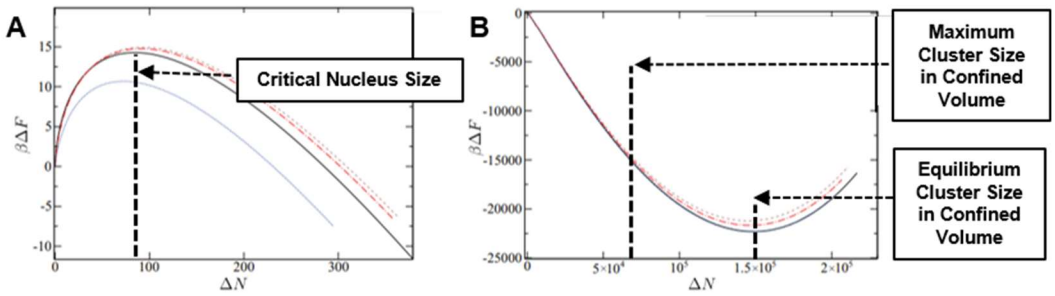

Figure 1.5: A) Helmholtz free energy as a function of cluster size, ΔN, depicting a high magnification plot of the leftmost region in 3B (small cluster sizes). This plot shows the nucleation barrier, and critical nucleus size below which particle nucleation is impossible. B) Low magnification (larger cluster sizes) plot of the free energy as a function of crystallite size. The minima in free energy represents the equilibrium cluster size, however in confined systems the total mass of the crystallizing phase may be completely depleted before achieving the equilibrium size. The various lines represent different nucleation theories (classical, modified etc.), but remain qualitatively similar. Adapted from ref:[56]

Indeed, although the ways of forming and modifying the reactors vary significantly, the unifying theme is that the nanoreactor size, shape, chemical content and position can dictate these same characteristics in the product particle (**Figure 1.6**). Compared with bulk solution-phase syntheses, nanoreactor techniques are more easily generalized to the preparation of novel materials

using new precursors because they do not rely upon dynamic reduction and highly material-specific ligand adsorption processes to control particle architecture.[42]

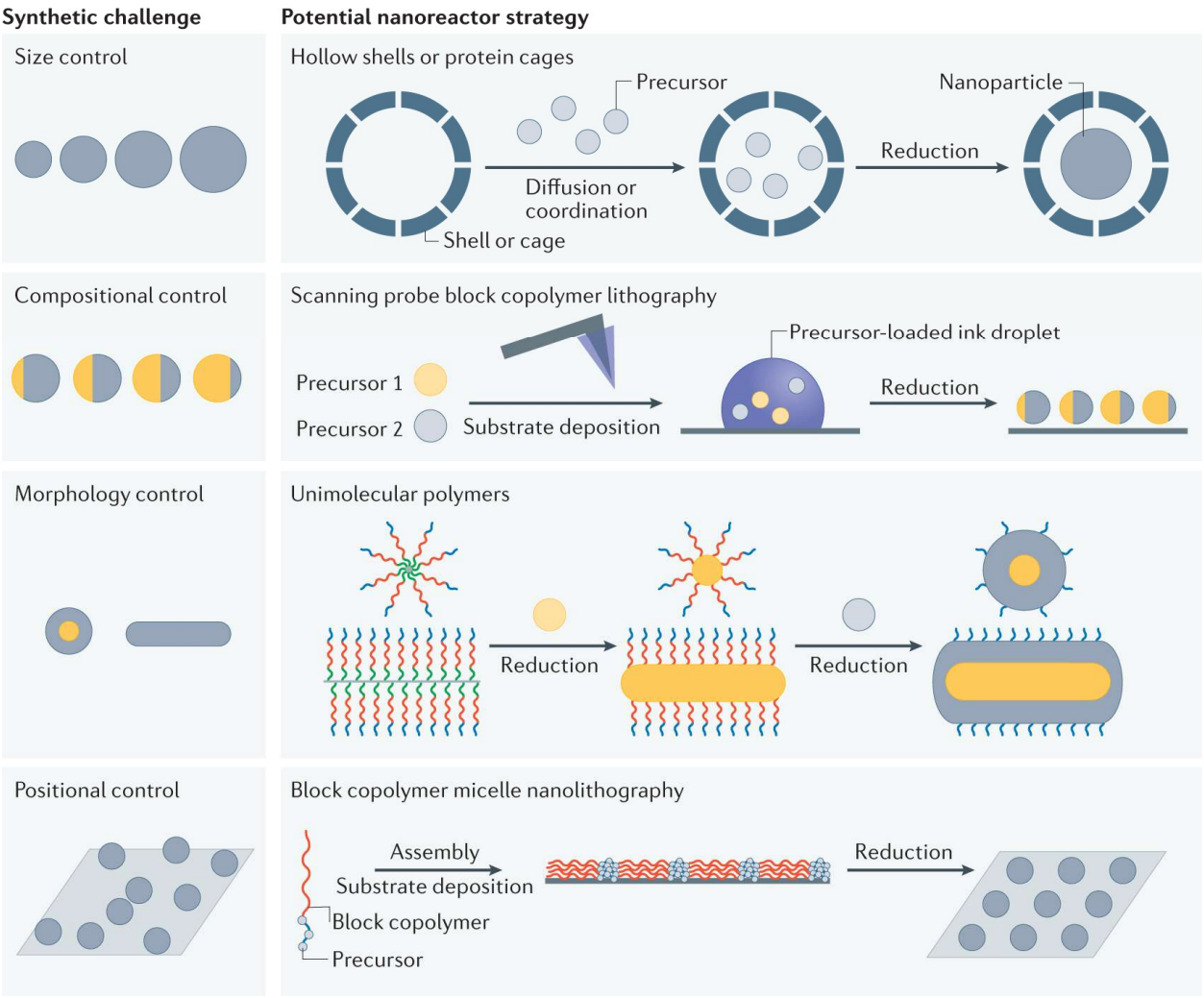

Figure 1.6: Example nanoreactor techniques used to overcome common synthetic challenges in attaining certain nanoparticle structural characteristics. Using nanoreactors, particles can be prepared for a variety of applications, spanning plasmonics, catalysis, magnetics and therapeutics. Adapted from ref:[13]

An additional advantage of the nanoreactor approach is that if high temperature annealing/calcination is involved in the synthesis process, subsequent heat-treatment required during reaction operation would be less likely to result in particle sintering, as the particles have likely already adopted their Wulff/Winterbottom-defined equilibrium configuration.[57] Utilizing nanoreactors to template nanoparticle synthesis is a well-studied area, with extensive research on

dendrimer/molecular templates,[58,59] block-copolymer templates,[60–62] and even physically defined templates.[63–65] Nanoreactor templates can be classified into solution-based reactors, where the template and reaction occur in a colloidal solution, and substrate-defined where the reactor is isolated on a surface. Some excellent examples of solution-based reactors include molecular cages and dendrimers (**Figure 1.7**), while some examples of surface-defined reactors include 3D porous media templates and micelle nanolithography defined reactors (**Figure 1.8**).

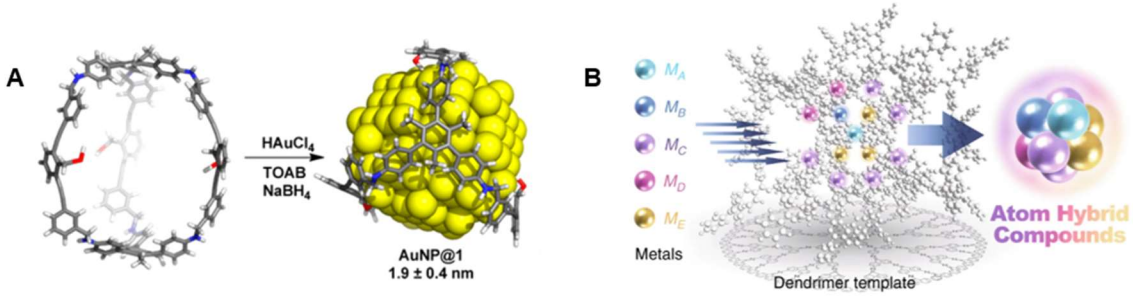

Figure 1.7: A) An organic molecular cage approach to synthesize gold nanoparticles, with binding moieties along the interior of the cage. TOAB is a phase-transfer catalyst mediating the two-phase liquid-liquid particle synthesis.[66] B) A dendrimer template approach containing phenylazomethine moieties which maintain an intramolecular potential gradient for step-wise complexation of metal salts from the inner sites to the outer. Adapted from refs: [66,67]

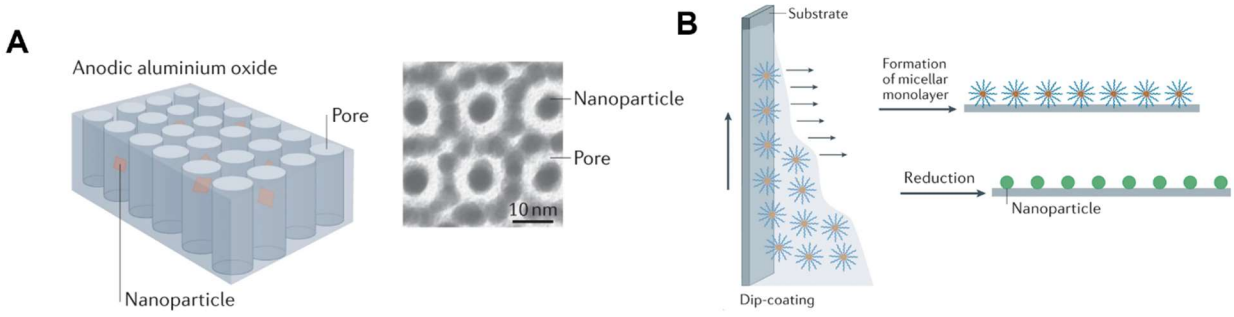

Figure 1.8: A) Left: Schematic of the use of anodic aluminum oxide to template nanoparticle synthesis. Right: Photoreduction-based synthesis of Pt nanoparticles within mesoporous silica. B) Dip-coating of a substrate into a micelle-containing solution with metal precursors loaded within enables formation of a micelle monolayer with a characteristic quasi-hexagonal pattern.

Subsequent reduction yields individual nanoparticles within each micelle nanoreactor. Adapted from ref:[13]

In 2010, the Mirkin group demonstrated the deposition of small volumes of a polymer mixed with a particle precursor upon a surface via an Atomic-Force Microscope (AFM) tip, called Scanning Probe Block Copolymer Lithography (SPBCL).[68] This technique provides many significant advantages over several nanoreactor generation techniques previously explored. Specifically, the particles are extremely stable to fairly high temperatures due to extensive annealing,[69] the particle composition reflects the nanoreactor composition—enabling modular synthesis of multimetallic particles in any stoichiometric ratio,[70–72] and the site-isolated particles enable facile assignment of processing, structure, property relationships especially with regards to catalysis.[73–75] As a scientific tool, this technique has borne great dividends (**Figure 1.9**), however the small scale of the synthesis makes heterogenous catalysis experiments extremely difficult due to low total product concentrations (for example in the reaction effluent stream as measured by GC-MS). In order to address this challenge, novel nanoreactor generation techniques are required to extend the advantages of SPBCL to systems of sufficient particle density to produce a quantifiable reaction output.

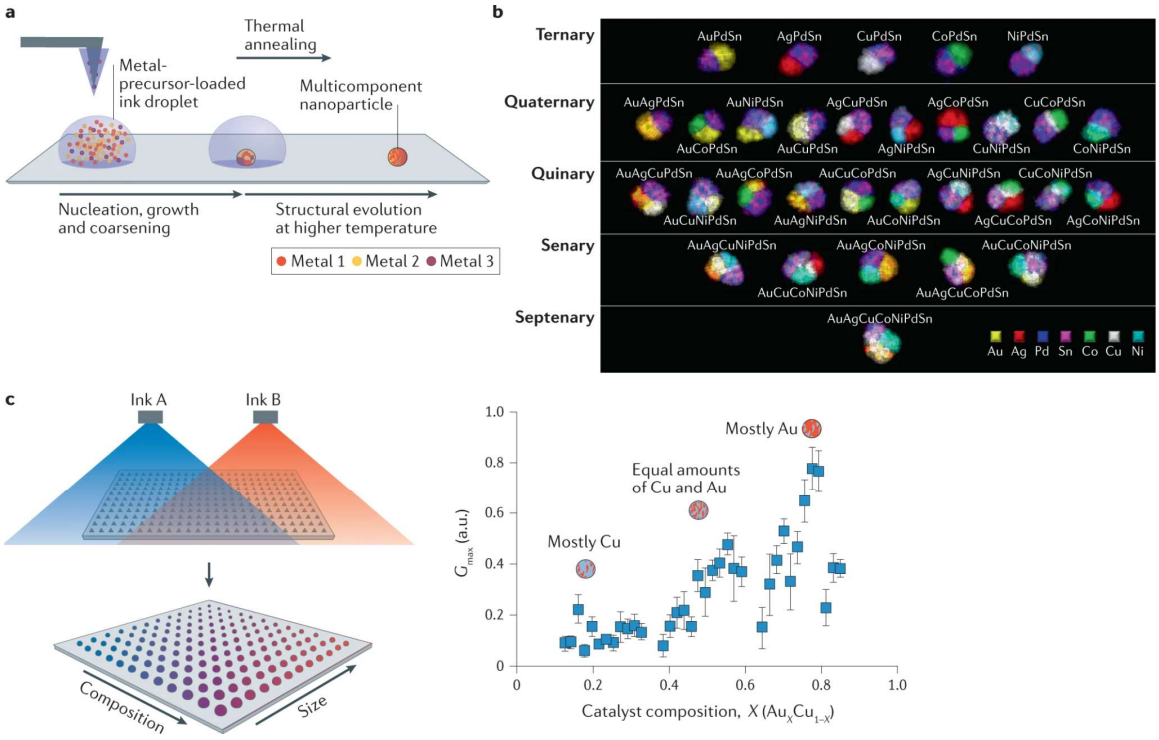

Figure 1.9: Atomic force microscopy tip-directed droplet deposition generates a block copolymer ink droplet loaded with metal precursors. A) The template confinement ensures that reductive annealing yields confined particle nuclei, which, upon further growth, yield a single multicomponent nanoparticle per droplet. B) Building from the work in ref[71], a seven-component combinatorial library was developed, demonstrating the complex phase behaviour of immiscible metals during single-particle formation. C) A megalibrary of nanoparticles (1 million unique compositions) was synthesized upon a surface consisting of pre-prepared micropillars by scanning probe block copolymer lithography. Gradients of metal precursor concentration were prepared by overlapping spray profiles of multiple precursor inks upon polymer pen scanning probes and a size gradient is produced by offsetting the spraying nozzles towards one edge of the pen array (left). The nanoparticles were screened as carbon nanotube growth catalysts by laser heating, which enables localized nanotube growth on an individual pillar, and simultaneous Raman spectroscopy of the nanotubes. Screening of AuCu alloys for carbon nanotube growth catalysts indicated Au3Cu as a promising composition. Gmax refers to height of the G stretch in the Raman spectra, associated with graphitic carbon (right). Adapted from refs: [70–72,74]

With this backdrop in mind, some of the questions that this research seeks to address are: 1) To what degree can the concept of confined block-copolymer inks as nanoreactors be generalized? 2) Which experimental factors control the nucleation and growth of nanoparticles in a confined volume? 3) How can these experimental variables be tuned to dicate the number and

composition of nanoparticles within the nanoreactor? 4) Can these particles be synthesized in a density and size/composition so as to be catalytically relevant?

CHAPTER TWO

Massively Parallel Nanoparticle Growth within Anisotropic Nanoreactors

Portions of this chapter are based on work published in: ACS Nano **2019**, *13* (11), 12408–12414.

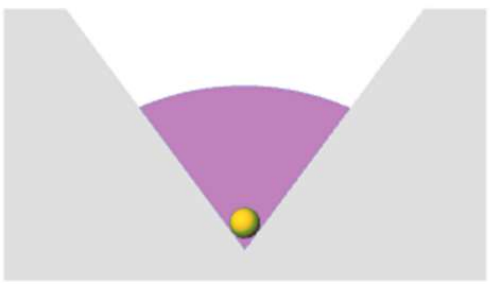

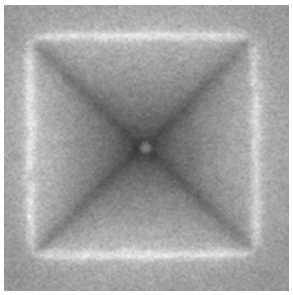

2.1 Introduction

The key advantage of nanoreactor based particle synthesis, as compared to traditional solution phase syntheses, is facile control over size and composition of the resulting particle, without the need to tune reduction kinetics, solvent compatibility, or precursor addition order and speed of introduction. However, key challenges for synthesizing with nanoreactors pertain to low throughput and control over resulting particle position. SPBCL[68,69] involves dissolution of particle precursors in a block copolymer ink, which upon tip-directed printing onto a surface yields hemispherical dome-shaped nanoreactors that template subsequent nanoparticle formation.[70] Since nanoparticle composition reflects the nanoreactor composition, dissolving multiple precursors in the ink solution enables high yield synthesis of single particles with as many as seven different elements.[72] When combined with large area cantilever-free scanning probe lithography methods,[76] SPBCL, has also been used to produce megalibraries consisting of millions of particles of varied composition on a single substrate.[74] These libraries have enabled promising insights into polyelemental nanoparticle phase segregation,[71] heterostructure engineering,[72] and multimetallic catalysis.[70,73,74]

While extremely useful, such techniques still require the use of scanning probe tools to fabricate the reactors and synthesize the particles that make up said libraries, limiting scale and throughput. Thus far, SPBCL has been utilized to synthesize a large material library of metals, metal oxides, and one semiconductor exclusively from water stable salts.[71,72,75,77] Herein, we report a method that aims to address these challenges by combining the concepts of reactors based upon nanoholes, and block copolymer inks pre-loaded with particle precursors. In doing so, we have developed a high-throughput synthetic method that can be utilized with water-sensitive precursors. In addition, we report that the use of pyramidal reactors, as opposed to cylindrical holes, not only

allows one to control particle size and composition, but also the placement of such particles with sub-5 nm resolution, **Figure 2.1A**.

2.2 Principle of Precursor Deposition within an Anisotropic Nanohole Template

In a typical SPBCL process,[78] metal salts are tightly confined in a hemispherical dome-shaped polymer droplet in order to force all precursors within to coarsen into a single particle. If the polymer droplet is above a certain critical size (>450 nm diameter for the systems studied thus far),[68,70] the precursor confinement effect is incomplete, and more than one particle forms within the polymer reactor. This is a hallmark of an Ostwald ripening process, as the driving force for particles re-dissolving into the matrix decreases significantly as the particle size increases.[79] When multiple particles grow unconfined in a large polymer volume, they typically exhibit a large distribution in size and, in the case of multimetallics, composition, eliminating a key advantage of nanoreactor templated syntheses. Thus, isolation of polymer droplets in small nanoreactors is key to ensuring complete aggregation of metal precursors, which in turn results in a small distribution in size and composition. Therefore, we hypothesized that in a nanohole templated synthesis, distributing small, isolated polymer droplets in each nanohole will inhibit transport of atoms from one hole to another. This morphology will minimize hole-to-hole interference and result in the desired single particle per nanohole scenario. We further hypothesized that this morphology could be achieved by altering the surface contact angle of the nanoholes using a nonpolar self-assembled monolayer which induces polymer dewetting.[80]

Silicon nanohole templates were prepared in a three-step process. First, photoresist was patterned into a square array of posts by solvent-assisted nanoscale embossing (SANE).[81] The uncoated areas eventually become a hard mask to resist silicon etching. Second, chromium was deposited onto the patterned substrate by thermal evaporation with subsequent liftoff in acetone.

This results in a pattern consisting of Cr features and exposed silicon. Finally, wet-etching of the silicon with aqueous KOH and subsequent Cr removal using a nitric-acid-based commercial Cr etchant yields the desired array of nanoholes, **Figure 2.1B, C**. In this proof-of-concept demonstration, the pyramidal holes were designed to have an array spacing $a_0 = 400$ nm and exhibit an edge length $d \approx 200$ nm.

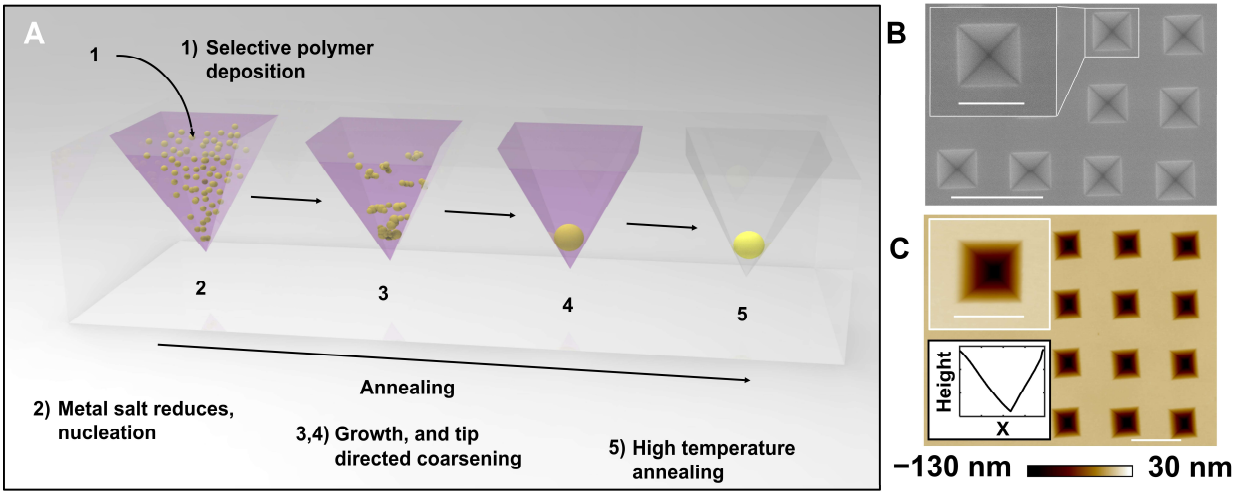

Figure 2.1: Tip directed nanoparticle synthesis. A) Scheme depicting the stages of nanoparticle synthesis in nanoholes. Polymer ink loaded with metal salt dewets into the nanoreactor followed by annealing. The tip of the nanohole directs the final particle position. B) Scanning electron microscope (SEM) and C) atomic force microscope (AFM) images of empty nanoholes. The width of the nanohole is approximately 200 nm, and its height is ~175 nm. The AFM linescan image is a zoomed-in region of the 150 nm length section over the apex of the pyramid. Scale bars are 500 nm, insets are 200 nm.

Prior to use, the arrays were treated with O_2 plasma and modified with various adsorbates with non-polar tails, to alter the polymer wetting properties. The wetting properties of the nanohole array are important in the context of the nanoparticle synthesis. As ethanol is the polymer solvent of choice, we systematically varied the surface chemistry, and investigated the effect on ethanol wetting properties and polymer morphology after spin-coating.

2.3 Surface Energy-Dependent Dewetting to Induce Selective Precursor Deposition

An unmodified nanohole substrate has an ethanol contact angle of 0° (**Figure 2.2**), which favors complete wetting of the poly(ethylene oxide)-*block*-poly(2-vinyl pyridine) (PEO-*b*-P2VP) copolymer material, **Figure 2.3A (i,ii)**. The low brightness and poorly defined nanohole edges in the SEM are indicative of a thin film coating the silicon surface. Furthermore, an AFM line-scan shows that the polymer residue leaves a concave morphology over the nanohole, implying strong polymer wetting, which results in minimal dewetting at the nanohole edges.[82] This is detrimental to controlled particle synthesis. Indeed, when the polymer solution was loaded with $HAuCl_4$, prior to spin-coating, and then thermally annealed in a H_2 atmosphere, nanoparticles (79 ± 35 nm) form in random locations all over the surface as opposed to within the nanoreactors, **Figure 2.3A (iii)**. In this experiment, the continuous polymer film prevents the desired isolated and locally controlled synthesis of nanoparticles in the reactors.

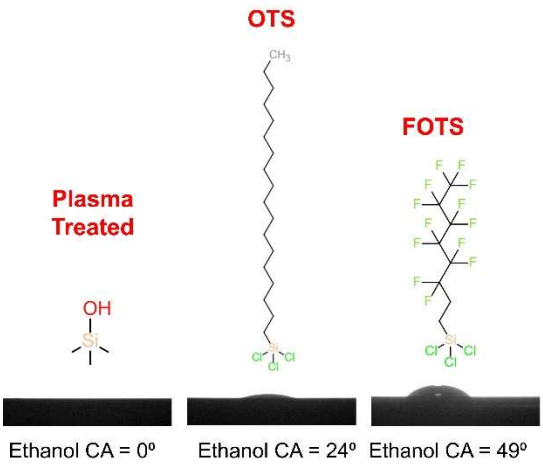

Figure 2.2: Measured contact angle as a function of surface treatment, along with chemical structure. Plasma treated, OTS (alkylsilane)-treated, and FOTS (fluorosilane)-treated silicon wafers.

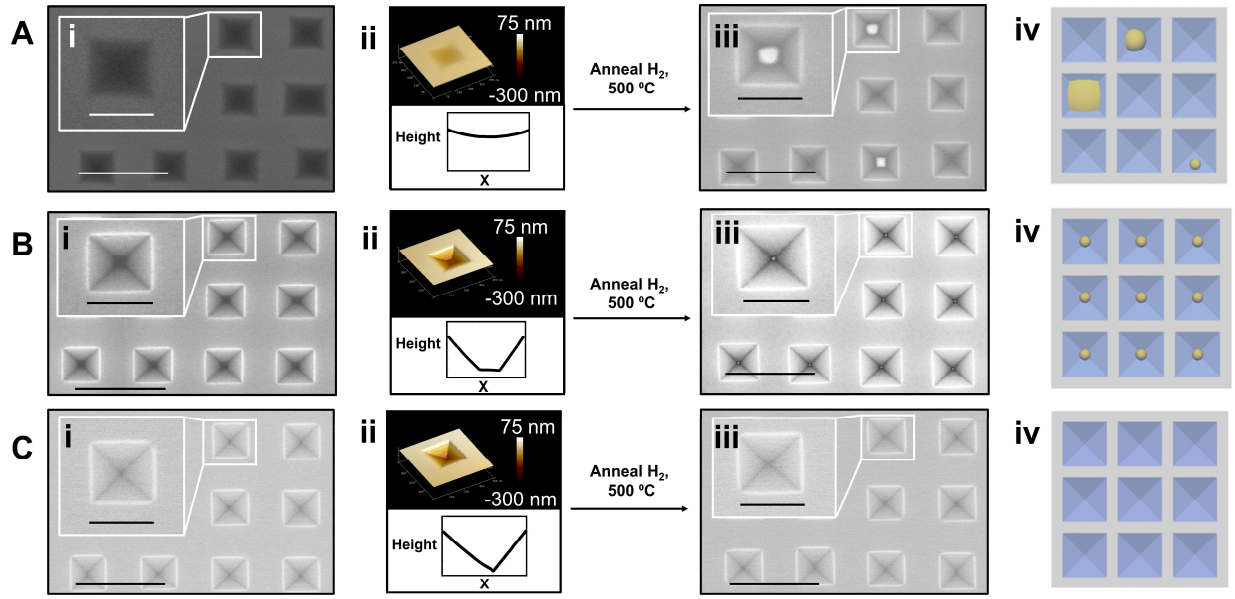

Figure 2.3: A) i) Polymer morphology in SEM and ii) AFM of low contact angle substrates loaded with polymer. AFM linescan images are all zoomed in to 150 nm length sections at the apex of the pyramid to clearly see the polymer features. Subsequent annealing yields iii), iv) large particles due to coarsening between wells. B) i), ii) Intermediate contact angle substrates via alkylsilane surface treatment yields isolated polymer in each well. Subsequent annealing results in iii), iv) single nanoparticles in each well. C) i), ii) High contact angle substrates induce complete dewetting and no residual polymer remains on the wafer. iii), iv) No nanoparticles are visible after annealing. Scale bars are 500 nm and insets are 200 nm.

Spin-coating on a nanohole substrate with an alkylsilane-modified surface with an intermediate ethanol contact angle of 24° (**Figure 2.2**) yields dramatically different polymer wetting behavior, **Figure 2.3B (i, ii)**. In this case, individual polymer droplets can be clearly seen in each nanohole, as regions of decreased brightness at the apex of the pyramid. In general, ethanol contact angles in the range of 22−35° were measured after coupling with this nonpolar alkylsilane, and all result in similar polymer morphologies. In addition, the AFM line-scan reveals that the nanoholes, post polymer deposition, exhibit a truncated pyramid shape, a consequence of the polymer filling the tip of the hole (compare the line-scan in **Figure 2.3B (ii) with Figure 2.1C**). By measuring the average nanohole volume before and after adding polymer, we measured a

decrease in nanohole volume of 30 ± 10%. We thus report an average polymer nanoreactor volume of 433 zeptoliters trapped in each nanohole. By comparison with previous reports,[82,83] this polymer morphology is a result of a low adhesion force between the polymer and silicon, causing most polymer to spin off the surface. However, polymer residues within the nanoholes are trapped due to an inadequate force necessary to exit the nanohole. This results in the desired discontinuous polymer droplet morphology, with polymer isolated within each nanoreactor, **Figure 2.3B (iii)**. Upon thermal annealing under H_2, single gold nanoparticles form in each reactor across the entire array. Nanoholes were imaged from all corners of the substrate (**Figure 2.4**), and successful nanoparticle synthesis was reproducible on more than 50 arrays. Each array yields approximately 6 million isolated polymer nanoreactors in parallel during a 1-minute spin-coating step.

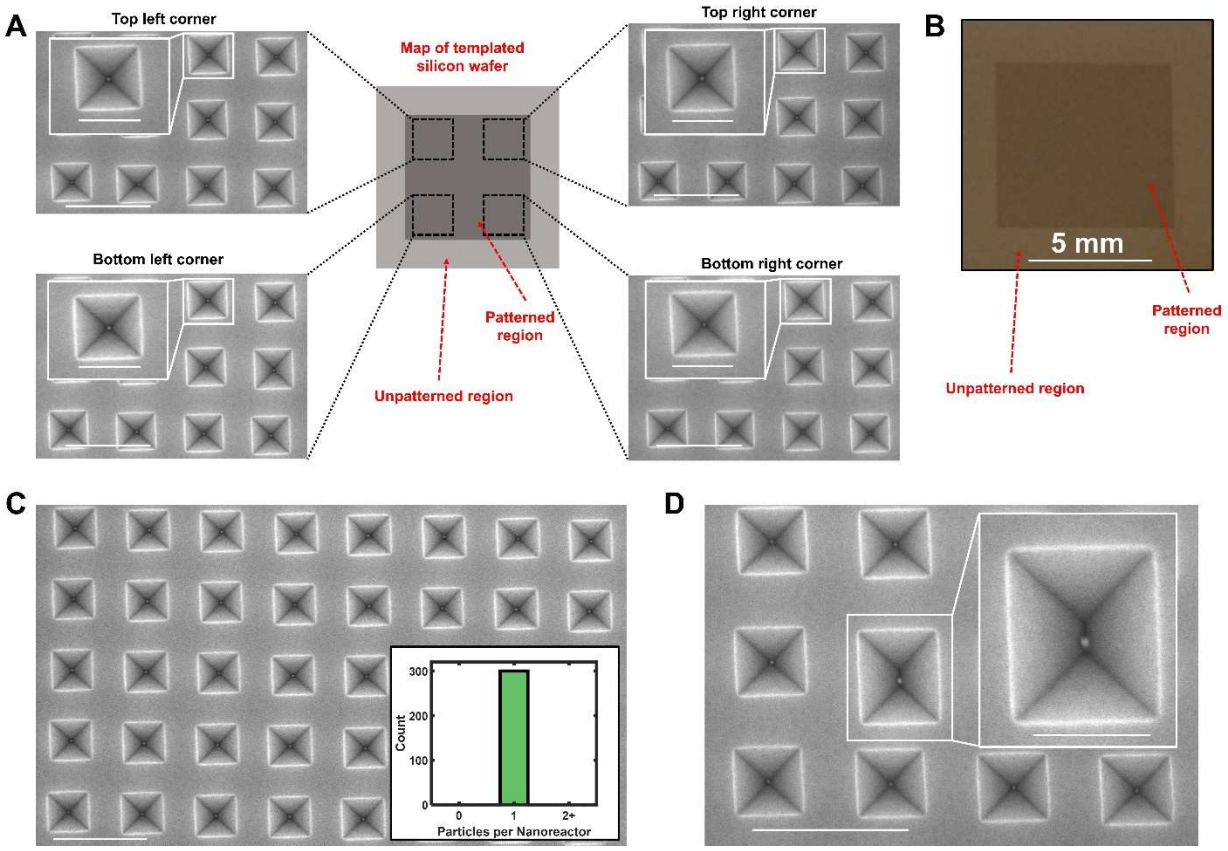

Figure 2.4: A) SEM images of the four corners of the nanohole substrate after annealing. Nanoparticles are formed via the template in massively parallel manner. B) Optical image of a typical wafer with diffraction pattern arising from the square pyramidal array. C) Low magnification image and observed yield of individual particles per nanoreactor. D) Single nanoparticles still form even in irregularly shaped nanoreactors, demonstrating defect tolerance. SEM scale bars are 500 nm and insets are 200 nm.

Further increasing the ethanol contact angle of the nanoreactor array to approximately 50° (**Figure 2.2**) with a fluorosilane-modified surface completely impedes polymer trapping, and upon annealing, no nanoparticles form, **Figure 2.3C**. The AFM line-scan shows that the sharp tip of the nanoreactor remains even after polymer spin-coating, indicating complete spin-off of the polymer. This result is as anticipated, as fluoroalkyl molecule-modified substrates tend to have extremely low adhesion force to polymers.[82]

2.4 Generalized Synthesis of Inorganic Nanoparticles within Nanohole Templates

By successfully realizing a nanoreactor templated synthesis in pre-patterned silicon substrates, generalization to directed particle synthesis from varied water sensitive salts becomes possible. To demonstrate this generality, nanoparticles from various salt precursors were synthesized, including semiconductor and metal precursors such as $GeCl_4$, $SeCl_4$, and $Ta(EtOH)_2$, that are known to hydrolyze upon contact with water,[84–86] but are stable in ethanol. It is important to note that in the absence of metal salt, nanoparticles do not form, **Figure 2.5A**. In addition to Au nanoparticles, Ag, Cu, Co, Ni, Ge, Se, and Ta particles were formed in analogous fashion from the appropriate salts dissolved in the ethanol polymer solution, *via* the same two-step reductive annealing process. This annealing process is crucial to forming individual nanoparticles, as previous SPBCL studies have shown that on average 3-4 particles form per nanoreactor for annealing times less than 1 hour, and that particle coarsening continues until at least 12 h have elapsed at 500 °C in H_2.[78]

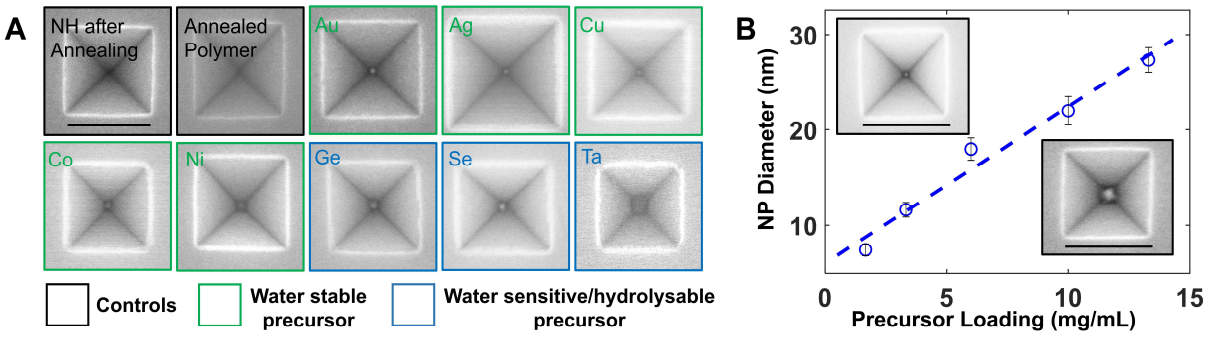

Figure 2.5: A) Material general synthesis of single-element nanoparticles. Initial controls of an empty nanohole annealed without polymer, and a nanohole with polymer but no metal salt loading. Bright features arise in the SEM due to nanoparticle synthesis directed to the tip. Water stable (green outline) and water sensitive (blue outline) salts are utilized. B) Size control experiments with gold salt to vinyl pyridine loading ratio between 1:4 and 1:0.5. Mean Au NP

Sizes are 7.4 ± 1.2 nm, 11.8 ± 1.4 nm, 18 ± 2 nm, 22 ± 3 nm, 27 ± 3 nm. N = 30 particles for each size, and correlation coefficient R^2 for best fit line is 0.98. Scale bars are 200 nm.

Prior studies correlating contact angle with electron energy loss spectra have shown that after coupling, the octadecyltrichlorosilane may be cleaved along the carbon backbone at these temperatures, but the siloxane head group remains intact at temperatures below 800 °C.[87]

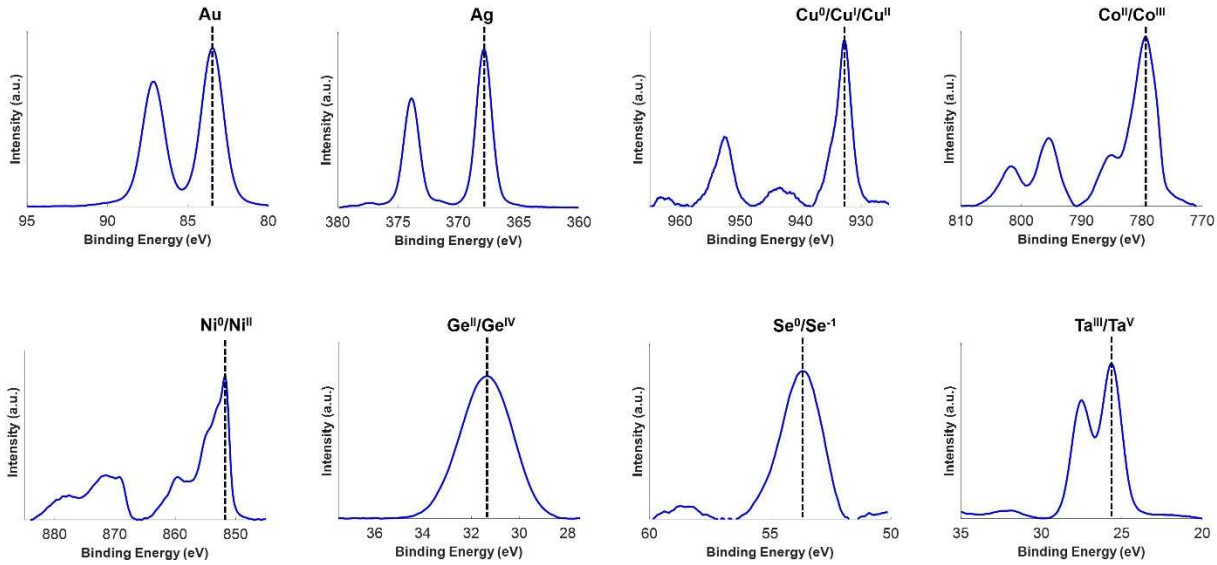

Figure 2.6: X-ray photoelectron spectra confirm presence of the anticipated materials after heat treatment. Samples were prepared by depositing the polymer precursor ink solution onto a flat silicon wafer, and subsequent high temperature annealing. Peak position and number of peaks provide oxidation state identification via Thermo-Fischer ESCALAB peak-fitting procedure.

Au, Ag, and Se exist in the reduced state (**Figure 2.6**). On the other hand, Cu, Co, Ni, Ge, and Ta exist, at least, as partial oxides. Since XPS is a highly surface sensitive technique, it is difficult to determine if oxide formation is a consequence of air exposure or beam damage.[88,89] In all cases, nanoparticle size can be altered by simply changing the precursor concentration in the initial ink, shown for gold with size tunability in the 7 to 30 nm range, **Figure 2.5B**. While the diameter of the particle has a cube-root dependence on precursor loading, a linear fit was used for simplicity over the size range selected. We found that significantly higher metal loadings (greater than 15

mg/mL of gold precursor for example) approach the solubility limit in the polymer ink, and thus were not explored further. Slightly higher metal loading was used for materials with a low contrast in order to improve visibility (metal:pyridine ratios of 1:1 were used for Au, Ag, Se, and 2:1 for the other materials). Despite some intermediate variability between materials (also potentially due to oxide penetration) the variability on a single substrate is typically low, as evidenced by the consistency in particle diameter measured *via* SEM, **Figure 2.4 and Figure 2.5B** (note error bars).

2.5 Nanoreactor Anisotropy Encodes a Preferred Particle Nucleation and Growth Site

Finally, it was hypothesized that anisotropic pyramidal nanoholes will direct the nanoparticle formation position to the apex of the tip. In order to investigate the importance of nanoreactor anisotropy, an array of cylindrically shaped nanoholes was generated for comparison by deep reactive ion etching (DRIE) into the silicon, as a replacement to the anisotropic KOH silicon etching step. This yields holes with comparable feature sizes and identical periodicities, but each hole has an isotropic cylinder shape, as opposed to the anisotropic pyramidal shape previously discussed. By using the alkylsilane surface treatment, followed by Au precursor ink deposition and annealing, nanoparticles similarly form in these isotropic holes. **Figure 2.7A**, **B** schematically depict the observed variance in particle position between anisotropic and isotropic nanoholes respectively. **Figure 2.7C** shows that both pyramidal and cylindrical nanoholes have an average interparticle distance in the array of ~400 nm. However, while the anisotropic square pyramids have a sharp gaussian distribution, with a standard deviation of ± 3 nm around the mean, isotropic cylindrical nanoholes have an order of magnitude larger standard deviation, at ± 40 nm. For the anisotropic pyramidal nanoreactor, nanoparticles form consistently at the apex of the pyramid, typically overlapping with the reactor center, **Figure 2.7D**, whereas isotropic cylindrical nanoreactors yield particles all around the reactor periphery, even on the reactor edges. This

variation in final particle position for isotropic nanoreactors is in agreement with previously reported results,[64] and leads to the aforementioned large standard deviation in the interparticle distance plot.

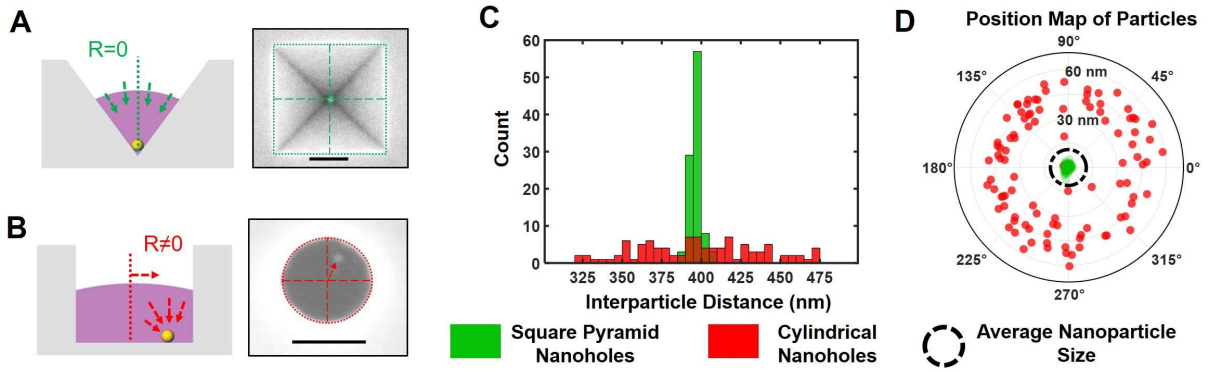

Figure 2.7: A) Anisotropic nanoreactor cross section scheme and observed final position. B) Isotropic nanoreactor cross section scheme and observed nanoparticle position. C) Histogram of interparticle distance for square pyramid (anisotropic) and cylindrical (isotropic) nanoholes in nm. D) Position map for the distance between nanoparticle center and reactor center. Average nanoparticle size (11 nm) provided for comparison. Scale bars are 100 nm.

The reason we observe an order of magnitude improvement in precision of nanoparticle position can be understood by analogy with experiments on solid-state dewetting of evaporated thin films on square pyramidal holes. In previously reported work,[90] the strong dependence of the local excess chemical potential, $\Delta\mu$, on the substrate curvature, κ has been exploited to create microparticle arrays. This can be understood with reference to the Gibbs-Thomson equation; $\Delta\mu = \kappa\gamma\Omega$, where κ is the curvature, γ is the interfacial energy, and Ω the atomic volume. In that work, the authors argue that the curvature, and proportionally the chemical potential, decrease with depth inside a pyramid, approaching negative infinity at the tip. This induces a diffusional flux of atoms from high chemical potential to low, per Fick's law. We propose that similarly in our system, during reductive annealing, atoms become mobile and experience curvature-induced diffusion through the polymer solution towards the apex of the pyramid. A local supersaturation of neutral atoms consequently arises at the tip, resulting in early nucleation of super-critical radii

nanoparticles. Subsequently, particle coarsening provides an additional source of diffusional flux towards the single largest apex-nucleated particle. The proposed mechanism suggests that substrate geometry is the dominant force directing the initial nucleation site of the nanoparticles; thus, regardless of material type, all nanoparticles should form at the pyramid tip, which is in agreement with our results.

This proposed mechanism gives significant insight into the observed particle position maps for other nanoreactor shapes as well, including cylindrical or even hemispherical SPBCL nanoreactors. The cylindrical nanoreactor is isotropic, as the curvature does not vary with depth of the reactor. However, this shape contains sharp 90° corners, implying that primary nucleation and growth should preferentially occur along the reactor periphery, where the curvature deviates from 0. This explains the observation that nanoparticles typically form at the edges of the reactor, as opposed to the center, and due to the circular isotropy, particles form in a variety of polar angles. This makes it difficult to achieve a uniform interparticle distance in the array. In contrast with SPBCL, a hemispherical nanoreactor is formed on a horizontal substrate, implying the curvature, and equivalently local excess chemical potential, are 0 throughout the nanoreactor. Upon annealing, supercritical radii particles form with no directing force, either radially or in polar angle. After coarsening, this yields a single particle without position control within the nanoreactor (**Figure 2.8**).

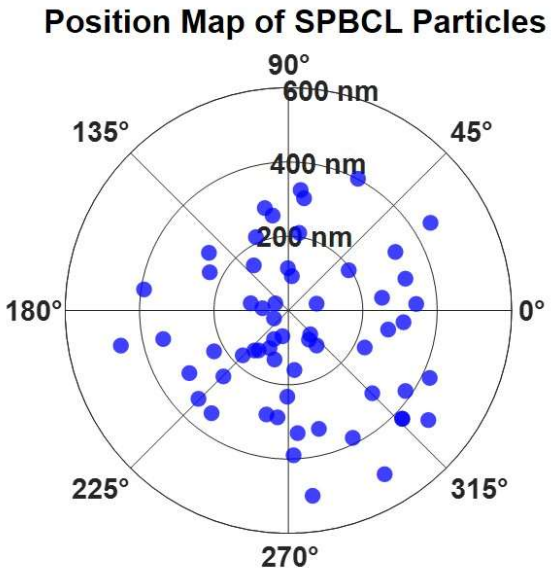

Figure 2.8: Position map of particles formed on horizontal substrates via scanning probe block copolymer lithography. 60 nanoparticles were formed from hemispherical 500 nm diameter nanoreactors on a flat substrate and their positions were overlaid.

2.6 Experimental Methods

Experimental/Methods

Nanohole Generation Process. Cr thin film patterns for nanohole synthesis were formed by SANE, thermal evaporation, and liftoff.[81,91] The result is a thin film of 8 nm Cr on Si, with holes in the film exposing bare Si. The regions of the wafer without Cr defined the nanohole. Next, the wafer was etched in potassium hydroxide (KOH) (Sigma Aldrich, 90% semiconductor grade) to generate anisotropic square pyramids, as the KOH etchant preferentially etches along the silicon <100> axis. A 1.5 M solution of KOH was prepared (200 mL) and heated to 70 °C, while 40 mL of isopropanol (Sigma Aldrich) was added when the solution was at 60 °C. The wafers were etched in this solution for 90 s, before removing and immersing in a water bath. Next the wafer was exposed to an air plasma at 200 mTorr and 30W (Plasma etch Inc. PE-50) for 2 mins to improve

the Cr etchant wetting of the surface. Finally, the Cr layer was etched for 45 mins in Chromium Etchant 1020 (Transene electronic chemicals) at ~60 °C, leaving pyramidal nanoholes in silicon, which were characterized by scanning electron microscopy (Hitachi SU-8030). Cylindrical nanoholes were formed *via* deep reactive ion etching using literature methods.[63,64]

Nanohole Surface Treatment. High surface energy nanoholes with low contact angle were formed by plasma treating the nanohole substrate immediately prior to deposition of the polymer-metal salt blend. Again, a 2 min, 30W process was used. This exposes free silanol groups which ensure complete wetting of the surface, where the ethanol contact angle was confirmed using a contact angle goniometer (Rame-Hart Instruments), as depicted in **Figure 2.2**.

An intermediate contact angle was obtained using a process similar to previously reported methods, in search of the so called 'bread-loaf' morphology, of polymer dewetting.[82] The modified process proceeds by first plasma treating the bare silicon nanoholes (2 min, 30 W) to expose reactive silanol groups crucial for silane coupling. The wafers were then incubated in a solution of the alkyl-silane octadecyltrichlorosilane (OTS, Sigma-Aldrich) in a volume ratio of 1:2 with solvent, which was a mixture of n-hexadecane and chloroform (both Sigma-Aldrich), in a 7:3 volume ratio. After incubating for 15 minutes and subsequent rinsing in chloroform, the ethanol contact angle was measured. As the OTS solution undergoes hydrolysis when exposed to trace ambient water, the purchased vial was stored in an Ar glovebox. However, as the solution ages, longer incubation times (30 to 45 min) can compensate to ensure a comparable ethanol contact angle, and qualitative de-wetting phenomenon. Results are shown in **Figure 2.2.**

Extremely high ethanol contact angles were achieved by deposition of a highly nonpolar silane, Trichloro (1H,1H,2H,2H-perfluorooctyl)silane (FOTS, Sigma Aldrich). The silicon surface was plasma treated as described above, and then placed in a glass beaker, alongside a small vial

containing the neat FOTS solution and covered. The beaker was set on a hot plate to a temperature of 100 °C for 15 min to increase the vapor pressure of the silane, thermally evaporating on the adjacent wafer. Contact angle measurements were again performed, as in **Figure 2.2.**

Polymer Nanoreactor Generation. The prepared nanoholes were then used as substrates, upon which a polymer loaded with various metal salts in ethanol (Sigma Aldrich) was spin-coated. Ethanol was chosen as the polymer solvent because: 1) several hydrolyzable metal and semiconductor salts are soluble and stable in it, 2) it has a lower surface tension, and 3) higher vapor pressure than water, features all crucial for polymer dewetting.[82] The polymer was poly(ethylene oxide)-*block*-poly(2-vinyl pyridine) (PEO-*b*-P2VP, Polymer Source, PDI 1.15) in a molecular weight ratio of 2300:1500, respectively. The metal salts used were $HAuCl_4 \bullet 3H_2O$, $AgNO_3$, $Cu(NO_3)_2 \bullet 2.5H_2O$, $Ni(NO_3)_2 \bullet 6H_2O$, $Co(NO_3)_2 \bullet 6H_2O$, $GeCl_4$, $SeCl_4$, and $(CH_3CH_2O)_5Ta$ (all Sigma Aldrich, 99.98% trace metals basis or higher.) A typical solution was prepared by dissolving 5 mg/mL of polymer in ethanol, followed by addition of acid (HCl for chloride salts, or HNO_3 for nitrate salts) to decrease the pH to 1, which improves coordination between metal salts and the P2VP unit, as well as the solubility of the metal salts. It was observed that in the case of gold, for example, high acid concentration (~1.5 M final concentration of HCl) was crucial to prevent the formation of micelles, which turned the solution turbid and unusable. Metal or semiconductor salt precursors were added to the acidic polymer solution, as this enabled metal to P2VP ratios as high as 2 to 1, or as low as 1 to 16, depending on the desired final size. Larger sizes were favored for particles with low SEM contrast, to improve visibility. In summary, metal:pyridine ratios of 1:1 were used for Au, Ag, Se, and 2:1 for the other materials. Finally, the metal loaded polymer ink was used to completely coat the nanohole substrate, followed by spin coating at 3000 RPM for 1 min at 1500 RPMs ramp (Laurell Technologies Inc, WS-650Mz-

23NPPB). If de-wetting was successful, the wafer should look identical to before spin-coating, with no polymer residue outside of the holes. Occasionally low areal density small droplets/residues (3-4 drops/cm^2) remain due to incomplete self-assembled monolayer formation, but these regions may be cut and excluded as necessary. The polymer nanoreactor formation was confirmed by atomic force microscopy (Bruker, Dimension ICON).

Heat Treatment. The polymer precursor-filled nanoholes were annealed in a H_2 environment in two steps, as per previous reports on polymer-mediated synthesis.[78] Briefly, the nanoholes were loaded into a quartz crystal tube furnace, and ramped to 150 °C in 15 min, then held for 12 h, followed by ramping to 500 °C in 1 h, and holding for 6 h. The furnace was allowed to cool to room temperature.

Scanning Electron Microscopy. The nanoparticles were characterized by scanning electron microscopy (SEM) (Hitachi SU-8030), using an accelerating voltage of 5 kV, operating current of 20 μA, and working distance of 2 mm. To avoid bias in the calculation of the interparticle distance, Fiji (distribution of ImageJ)[92] was used to automate the process, using binary thresholding, and the find maxima function to evaluate the particle positions. The output nanoparticle positions in cartesian coordinates were subsequently run through a custom MATLAB script used to evaluate and plot interparticle distance.

Atomic Force Microscopy. The nanoreactors were characterized by atomic force microscopy (AFM, Bruker, Dimension ICON), operating in standard tapping mode, with a 1 Hz scan rate, 512 bits/line. Measurements on an empty nanohole, which had been treated with the silane of interest, was typically conducted in advance, to confirm that polymer features were not due to tip convolution or a damaged AFM tip. Once a reference surface was imaged, in which sharp

nanoholes were observed, the same AFM tip was used to study the polymer morphology on spin-coated substrates.

X-Ray Photoelectron Spectroscopy. Positive controls for nanoparticle formation were provided by X-Ray Photoelectron Spectroscopy (XPS, Thermo Scientific ESCALAB 250XI). The samples for XPS analysis were nanoparticles synthesized on flat wafers to increase the XPS signal. A standard XPS workflow was followed,[89] with charge compensation enabled. The peaks were all shifted using the carbon 1s peak to calibrate the peak position and determine the oxidation state. Thermo-Fischer Avantage software was used to identify different chemical states. Nanoparticle confirmations are provided in **Figure 2.6.**

2.7 Conclusions and Outlook

This work is important for the following reasons. First, it shows how square pyramidal nanoholes in silicon serve as an excellent template for the precise deposition of polymer precursor and subsequent particle synthesis. Second, it introduces a straightforward way of controlling polymer morphology by altering surface wetting properties, which is crucial for eliminating interference between neighboring nanoreactors. Finally, the use of anisotropic nanoholes provides a materials general route to synthesizing nanoparticles with excellent position control (an order of magnitude improvement in precision over isotropic nanoreactors). Taken together, this work outlines a comprehensive strategy for materials chemists to quickly synthesize particle-based structures over large areas in a site-specific manner. Given the importance of nanoparticles in catalysis, the energy sciences, electronics, and optics, this methodology may become quite useful for studying and screening large libraries of structures for exceptional chemical and physical properties.

CHAPTER THREE

Polymer-enhanced Nanoparticle Growth within Hollow Silica Shell Nanoreactors

Portions of this chapter are based on submitted work currently in revision.

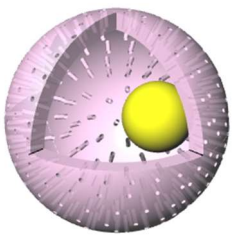

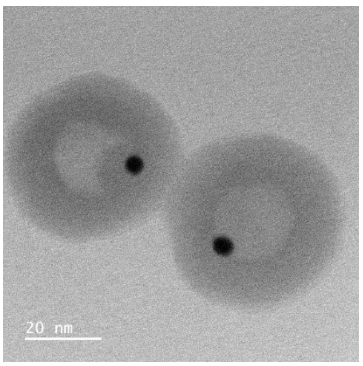

3.1 Introduction

Methods are needed to rationally design and synthesize nanoparticle products with specific sizes, shapes, and compositions because these features dictate their electrical,[93–95] optical,[96,97] or chemical[32,38,98,99] properties, and thus their performance in downstream applications.[50,100–102] Nanoreactor-based strategies have emerged as a promising means to tune particle size,[35,103–105] composition[67,106] and structure,[72,75] in ways that exceed what is possible with traditional syntheses that depend on tailoring reduction kinetics and ligand chemistry.[13,42] Nanoreactors operate by confining reactants within nanoscale volumes in order to deterministically drive complete conversion of reactants to particle products. For example, scanning probe block copolymer lithography (SPBCL)-generated polymeric domes on surfaces have been extensively used as reactors for the synthesis of a wide variety of particle types,[68,71,72,75,107] and then screened for properties of interest.[70,73,74] With this methodology, many independent attoliter polymeric domes each confine the reactants for the synthesis of a single particle positionally encoded on a substrate of interest. Up to seven element particles have been synthesized to date,[72] and libraries with a million different structures (so called "megalibraries") have been generated in chip-based format and subsequently used as discovery tools.[74] However, the scale-up of structures identified through such studies presents challenges.

A promising solution-based nanoreactor strategy that involves the large-scale generation of particles of interest relies on pre-loading metal salts into hollow silica shells followed by reductive nanoparticle growth. This methodology yields a high degree of particle size control (2-5 nm range),[108] and the amorphous silica support material is stable at high temperatures ($T_m \approx$ 2000 K), which prevents excessive particle sintering.[30] However, at present, it is difficult to synthesize particles of uniform size and composition (with respect to the numbers and types of

elements).[27,109–111] Indeed, processing conditions that favor particle coarsening often result in particle escape and sintering outside of the reactor, while conditions that do not favor coarsening result in polydisperse mixtures of particles that reflect the random fluctuations in their local chemical environments during synthesis.[27,112]

Herein, taking inspiration from SPBCL, we postulated that a polymer matrix employed in the synthetic strategy involving hollow silica shell nanoreactors would enable the synthesis of larger and more uniform nanoparticles from metal ion reactants (compared to when hollow shells without polymer were used). The rationale was that the polymer matrix would serve to facilitate ion/atom diffusion at lower temperatures typically dominated by particles polydisperse in size. To test this hypothesis, water-in-oil microemulsion droplets were loaded with $HAuCl_4$ and aqueous polymer, and silica shells were grown around them; then, reductive annealing was conducted in a tube furnace. Three different polymers, poly(ethylene oxide) (PEO), poly(acrylic acid) (PAA), and poly(ethylene oxide)-*b*-poly(2-vinylpyridine) (PEO-*b*-P2VP), were explored in this process; these polymers were chosen because they have varying interaction strengths with the metal salt and synthetic microemulsion environment. The highest yield of single gold nanoparticles within the nanoreactors was obtained when polyethylene oxide (PEO) was used; when polymer was not used, multiple particles were often observed in each nanoreactor. This result along with correlative electron microscopy indicates that the presence of a polymer matrix that facilitates diffusion of the reduced metal is important for producing the desired single particle products in this process.

3.2 Incorporation of Polymer within Hollow Silica Shell Nanoreactors

Water-in-oil microemulsion droplets were loaded with metal salts and aqueous polymers to investigate the role of the polymer in the coarsening dynamics and single-particle yield within hollow silica shells. The microemulsion droplets were loaded with metal salts before silica shell growth to ensure precursor confinement, and prevent non-specific growth or particle growth within the shell itself.[113] Briefly, the metal salt ($HAuCl_4$) and the polymer were dissolved in water before being introduced to a vigorously stirred solution of the oil-phase solvent n-decane and two surfactants (Igepal CO-520 and n-hexanol) (**Figure 3.1**).

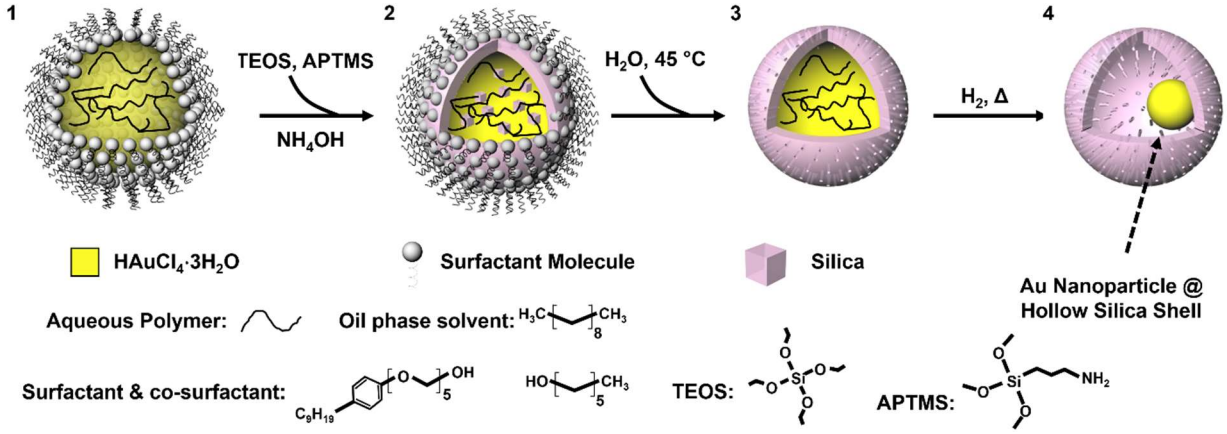

Figure 3.1: Scheme showing the four stages in the synthesis process of gold nanoparticles within silica shells. 1) Metal salt and polymer molecules dissolved in water are dispersed in an oil-phase solvent stabilized by two surfactants. 2) Silane precursors are introduced, with a base catalyst to commence silica shell formation. 3) Warm water is used to remove surfactants and residual uncondensed silica. 4) Reductive thermal annealing is carried out in two stages in a tube furnace to promote the formation of single metal nanoparticles.

3.3 Bulk Characterization of Nanoparticle Products

This large molar volume solvent was selected rather than typical a cyclohexane microemulsion as this increases the equilibrium aqueous phase droplet diameter.[114] This facilitates simpler characterization through electron microscopy of the resultant particles, but also increases the difficulty of achieving complete coarsening given the larger dimensions of the nanoreactor. Next, silane precursors were introduced along with ammonia hydroxide catalyst to form the silica

shells, and after three days of stirring, the shells were washed twice via centrifugation to remove residual surfactant, organic molecules, and residual silica within the cores. Finally, the shells were annealed in a reductive H_2 environment, typically in two steps at 200 °C (below the decomposition temperature of the polymer) and 600 °C (above the decomposition temperature of the polymer) (**Figure 3.2A**). The lower temperature step facilitates nanoparticle nucleation and growth, while the higher temperature step facilitates further structural evolution analogous to that seen in the SPBCL-based system.[69,115] PEO was utilized in this synthetic scheme because it is water soluble, facilitates particle diffusion,[116] and is relatively residue-free after thermal annealing (> 99 % mass loss above 500 °C, **Figure 3.2B,C**), leaving the metal particle surface clean for further use.

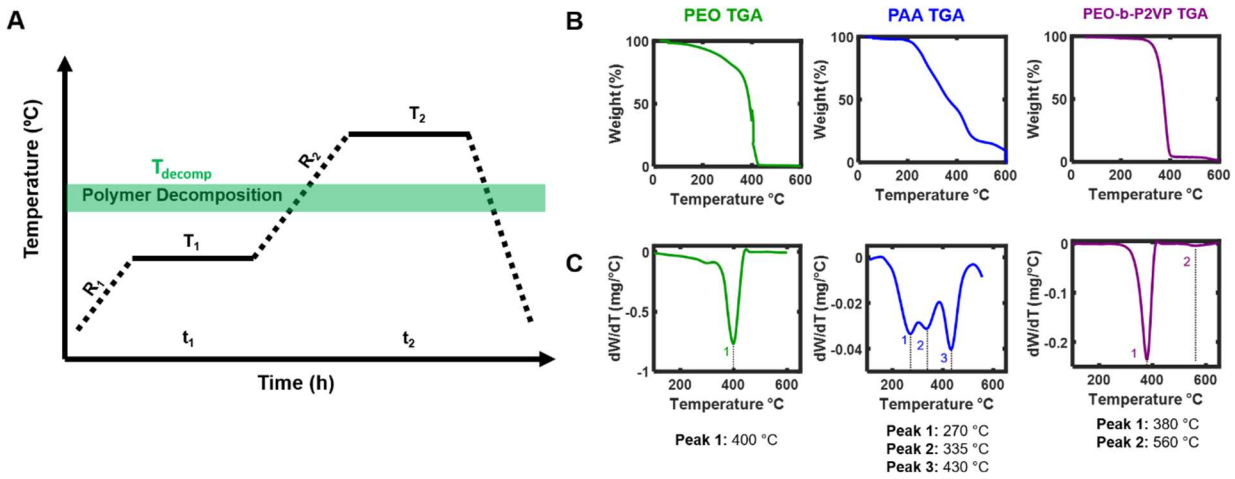

Figure 3.2: A) Two-step reductive annealing profile for nanoparticle growth within hollow silica shells. B) Thermogravimetric analysis showing weight vs. temperature for the three tested polymers. C) Derivatives of the TGA data show peaks in weight loss at certain temperatures for each polymer.

The reaction products were imaged using scanning electron microscopy (SEM) and scanning transmission electron microscopy (STEM). Further, energy-dispersive x-ray spectroscopy (EDS) was used to map the chemical identities of the shell contents. Hollow spherical shells were

observed, with diameters (40 ± 6 nm) dictated by the microemulsion templating process (**Figure 3.3A**); the low-contrast region within each shell observable in transmission or high-angle annular dark-field microscopy modes indicates that they are hollow (**Figure 3.3A, 2B,i.**). Higher contrast, smaller diameter (5.7 ± 0.7 nm) spheres were observed within the hollow shells that were comprised of gold metal (**Figure 3.3B,ii.**). The X-ray diffraction pattern of these structures matched that of FCC Au (i.e., powder diffraction files from the International Center for Diffraction Data (ICDD)) (**Figure 3.3C**); the amorphous silica only contributes a broad background to the diffraction pattern. UV-vis spectroscopy also revealed the presence of a plasmon absorption band centered at approximately 540 nm (characteristic of gold particles of this size) that was not present before annealing (**Figure 3.3D**).[117] Finally, X-ray photoelectron spectroscopy was used to monitor the oxidation state of the gold before and after the reductive annealing steps (**Figure 3.3E**).

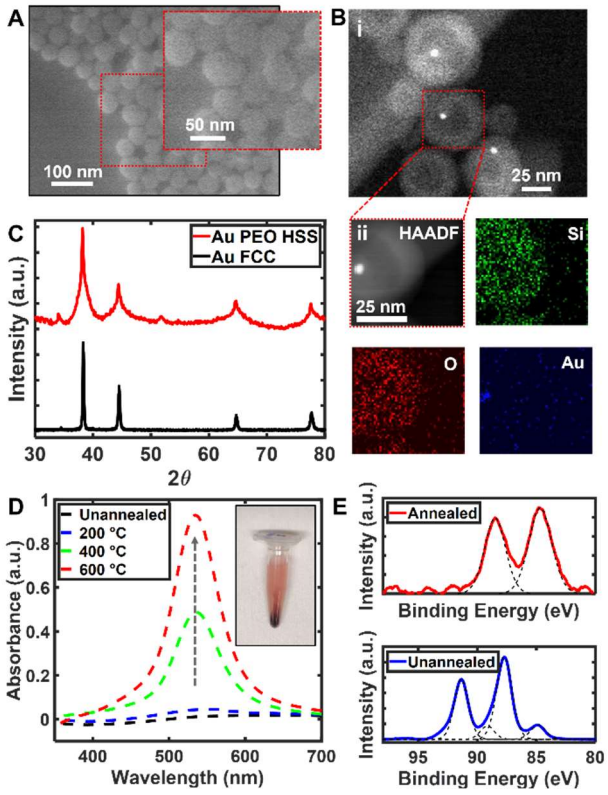

Figure 3.3: Characterization of the Au metal salt-PEO ink incorporated within hollow silica shells (HSS). A) A SEM image of the external surfaces of the silica shells, and B) i) a STEM image and ii) elemental map of gold particles isolated within silica shells. C) XRD data and literature powder diffraction pattern showing the presence of FCC gold in the annealed samples. D) UV-vis data shows the emergence of the LSPR band that is characteristic of Au nanoparticles. The inset shows a photograph of a small vial containing the collected products after reductive annealing. E) XPS data of the unannealed and annealed samples, showing a clear decrease in the oxidation state of the Au 4f electrons after reductive annealing. The dotted lines represent peak deconvolution into contributions from oxidized gold (higher binding energy) and reduced gold (lower binding energy); indicating the presence of zero-valent Au in the final product.

Before reductive annealing, some quantity of gold salt was in reduced form, perhaps due to photoreduction from the ambient light or impinging X-rays,[88,89] but the majority of the gold present was in the 3^+ oxidation state. After reductive annealing, two peaks corresponding to the spectra from zero-valent Au 4f photoelectrons were observed, indicating that the metal ions were reduced to metallic solid particles. The surface area and porosity were revealed based on N_2 adsorption isotherms (**Figure 3.4**); the pore-size distribution was bimodal including smaller

mesopores on the surface of the silica shell (d < 5 nm), and then a large cavity arising from the hollow silica shell itself (d ~ 40 nm).

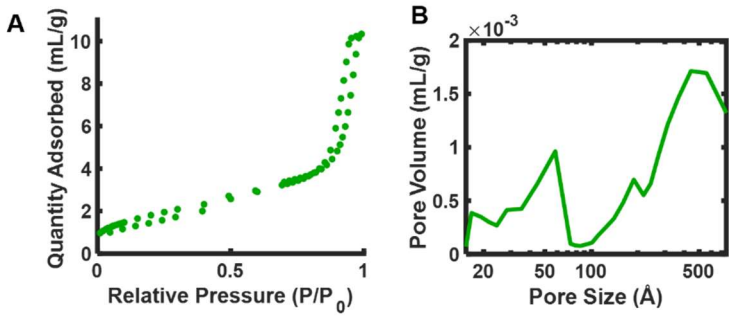

Figure 3.4: A) N_2 adsorption isotherm after reductive annealing and synthesis of gold nanoparticles with PEO polymer incorporated within hollow silica shells. B) Pore size distribution showing bimodal pore distribution, including small mesopores on the surface of the silica shell, and a larger cavity within the silica shell. Specific surface area using the Brunauer-Emmett-Teller (BET) method: 6.6 m^2/g.

3.4 Polymer-ink Dependent Coarsening within Hollow Silica Shell Nanoreactors

As a control, the same reaction was run with silica shells that did not contain polymer, and the reaction also was run with shells that incorporated PAA or PEO-*b*-2VP, instead of PEO. These polymers also coordinate or associate with the metal salts, and the block copolymer PEO-*b*-2VP, in particular, is known to increase the mobility of metal salts and atoms leading to large single nanoparticle formation in the SPBCL system.[70] Qualitatively, a higher yield of individual nanoparticles within each reactor was observed when a polymer was used (**Figure 3.5A**); the polymer-free system yielded a large number of shells with multiple particles, indicating that coarsening was incomplete (**Figure 3.5B**). The highest yield of single particles (76%) was attained when PEO was used. The average particle size also increased when PEO was used, and the particle size distribution decreased (no polymer: 3.1 ± 1.7 nm, PEO: 5.7 ± 0.7 nm), indicating

that the polymer-containing silica shell is acting as an effective nanoreactor and driving all trapped precursors into a single particle product (**Figure 3.5C**). The single particle yields and final particle sizes and size distributions for the PAA and PEO-*b*-P2VP systems (PAA: 54%, 4.0 ± 1.3 and PEO-*b*-P2VP: 50%, 3.6 ± 0.9 nm) were found to be in between those of the polymer-free and PEO systems.

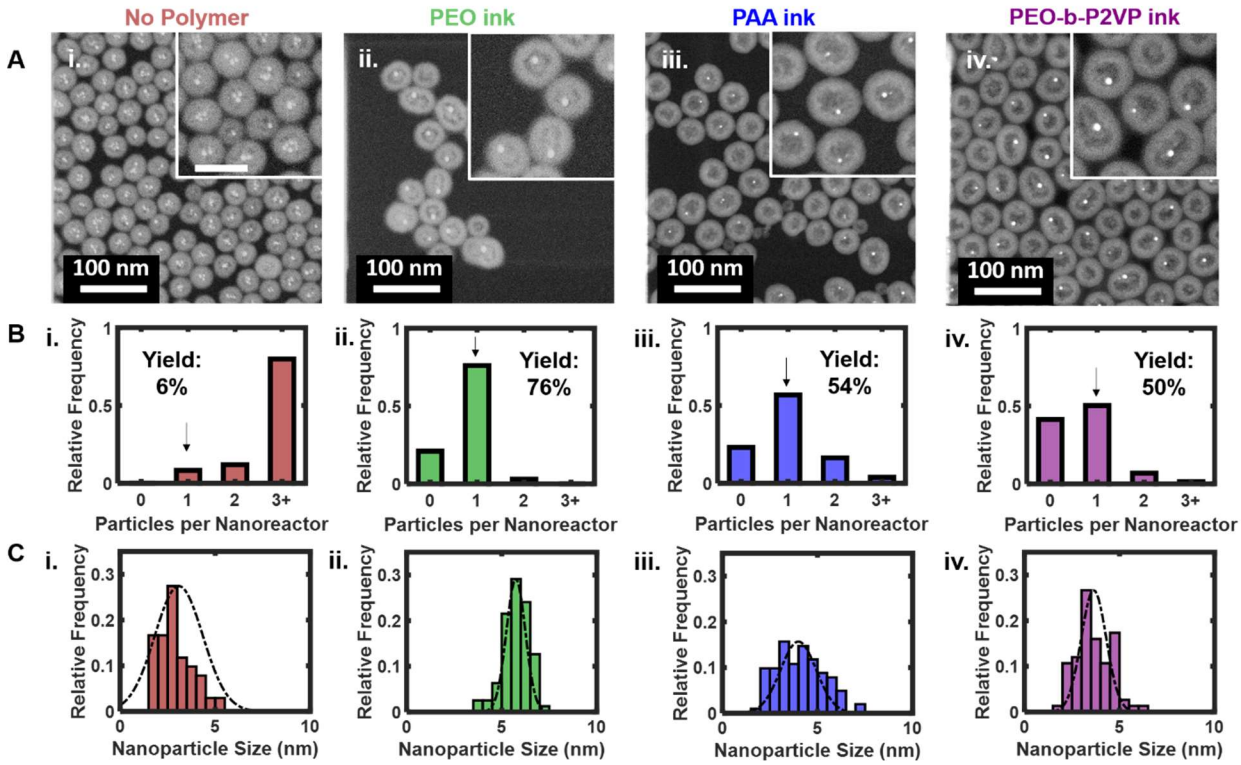

Figure 3.5: Particles per nanoreactor and particle sizes as a function of presence and type of incorporated polymer. A) STEM images of the nanoparticles after reductive annealing with i. no polymer incorporated, ii. PEO incorporated, iii. PAA incorporated, and iv. PEO-*b*-P2VP incorporated. All of the images in the insets were taken at the same magnification, and the scale bar for the inset in i. is 50 nm. B) Histograms showing the number of nanoparticles per nanoreactor for each polymer type, and the yield of individual, single nanoparticles in each case. C) Histograms of the nanoparticle sizes and associated dispersity as a function of polymer presence and type. The dotted lines represent the fit with a normal distribution. The sizes are: no polymer: 3.1 ± 1.7 nm, PEO: 5.7 ± 0.7 nm, PAA: 4.0 ± 1.3, and PEO-*b*-P2VP: 3.6 ± 0.9 nm.

The role of polymer chemistry on nanoreactor single particle yield can be understood based on three general factors: the reduction dynamics of the metal salt, the mobility of the metal ions and

atoms in the polymer, and the effect of the polymers on the structure of the microemulsion droplets. Given the weakly coordinating nature of the ether subunits within the PEO polymer,[118–120] it was hypothesized that the dynamics of the transition from metal salt to reduced metal atoms that occurs within the hollow shell system may be modified when PEO is present. To test this hypothesis, temperature programmed reduction was applied to monitor the uptake of H_2 of the metal salt $HAuCl_4$ x 3 H_2O in the absence and presence of PEO. When PEO is not incorporated, we observe two large H_2 consumption peaks, as well as HCl evolution, which we associate with the reduction of the metal salt (**Figure 3.6**).

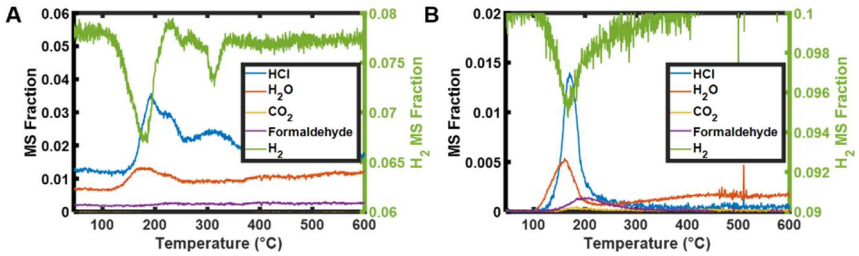

Figure 3.6: Temperature programmed reduction for metal salt precursor $HAuCl_4$ x 3 H_2O, and the metal salt mixed with PEO. A) Mass spectrometry of the effluent stream from the gold salt alone during reductive annealing in H_2. Two H_2 absorption peaks are observed, which broadly overlap with HCl production, with maxima at T = 170 °C and 310 °C. B) Mass spectrometry of the effluent during H_2 reduction of $HAuCl_4$ mixed with PEO in the same mass ratio (2:1) as within the silica shells. One collective peak is observed at T = 165 °C, overlapping with that of HCl production. Carbon peaks due to the decomposition of the polymer are monitored with the CO_2 and formaldehyde produced.

This process occurs in the range of approximately 120 °C to 350 °C, and the two-step reduction process in this temperature range has been previously attributed to two-stage reduction from Au^{3+} to Au^{+} and then from Au^{+} to Au^{0}.[121] However, the difference in the H_2 consumed and HCl produced between the two peaks implies that some quantity of gold salt may be fully reduced in the first stage. In contrast, when PEO is incorporated in the same mass ratio as utilized in the hollow shell experiments, we observe one slightly broader collective H_2

consumption peak, which strongly overlaps with the HCl production peak, occurring at 165 °C. Based on this evidence, it appears that the PEO serves as a weak reducing agent, which is in agreement with past reports,[122,123] and leads to completion of the reduction process at a lower temperature (~ 250 °C vs. 350 °C) in our experiments. Based on this evidence, we infer that within the silica shells, despite using the same thermal treatment, PEO incorporation may accelerate the reduction process and therefore jump-start the nucleation and growth of reduced metal atoms.

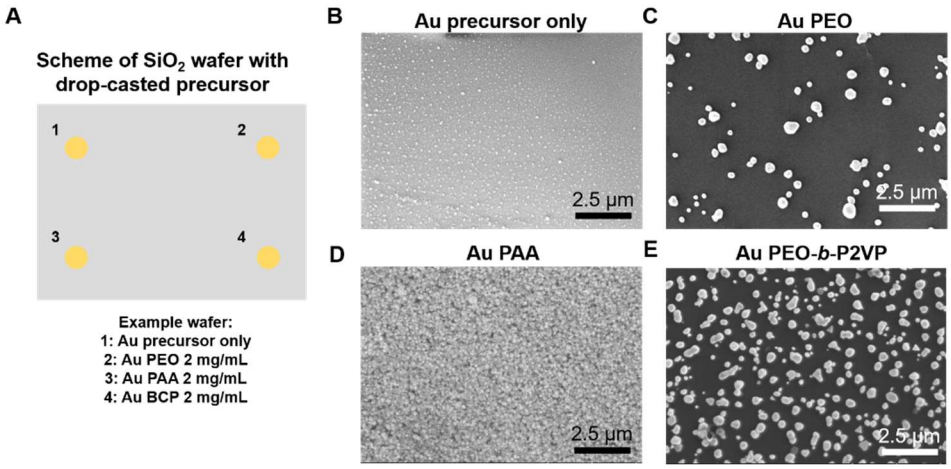

Figure 3.7: A) Schematic representation of drop-casted precursor on the same wafer to compare how polymer inks effect coarsening. B) Polymer-free, C) PEO-containing, D) PAA-containing, and E) PEO-b-P2VP-containing inks were used to prepare these nanoparticle-coated wafers. All inks contained polymer at 2 mg/mL and metal salt at 4 mg/mL. The particle diameters were calculated based on higher magnification images.

In order to directly investigate the mobility of the metals with the three polymers used, polymer-metal ink mixtures were drop-cast onto untreated silicon wafers and subjected to reductive annealing (**Figure 3.7**). Because the wetting of the inks on the wafers were similar (**Figure 3.8**), it was assumed that the observed differences in coarsening were caused exclusively by differences in diffusion through the dried polymer-matrix. When inks of the same concentrations were subjected to identical annealing conditions as those used for the shell-based

reactions, significantly more coarsening was observed for inks containing PEO and PEO-*b*-P2VP compared to those containing PAA or those not containing polymer (**Figure 3.9**). For example, the gold nanoparticle diameter produced in the no-polymer system was 19 ± 7 nm; it was 150 ± 60 nm in diameter when PEO was used. These results imply that PEO and PEO-*b*-P2VP facilitate diffusion to a greater extent than PAA, and that more diffusion occurs when polymers are present. This information helps one interpret the low yield of single particles in the presence of PAA (54%). Based on the observed data, the strength of the interaction of the ligand to the metal salt itself is not highly predictive of the degree of coarsening observed in unconfined media. Indeed, the average particle size is not correlated with the spectrochemical series for the repeat units within each polymer; their interaction strengths are comparable and depend on metal ion oxidation state/geometry, but generally decrease in the order: pyridine > ether > acrylate.[120,124–127] This observation implies that the diffusion of the reduced metal through the polymer dictates final particle size rather than the interaction of the unreduced metal salt with the polymer.

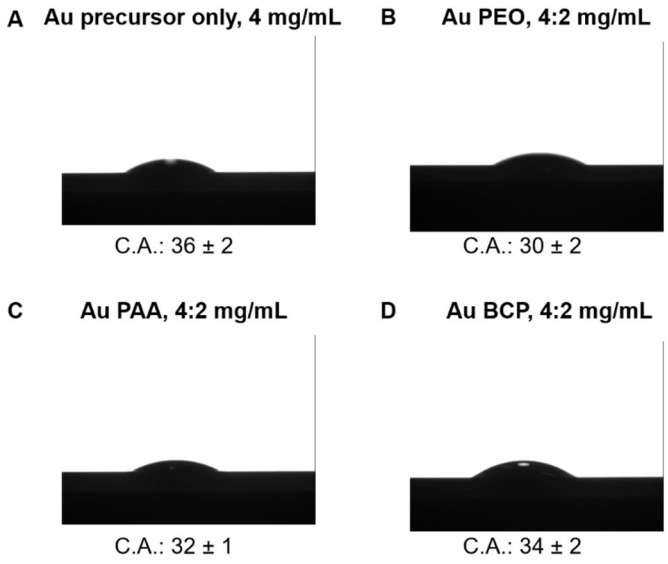

Figure 3.8: Contact angle goniometry data from gold precursor solutions that are A) polymer-free, b) PEO-containing, c) PAA-containing, and D) PEO-b-P2VP-containing. The similarity in contact angles demonstrate that the polymer incorporation does not significantly change the surface tension.

The effect of the structure of the microemulsion droplets, as dictated by the choice of polymer, also plays a role on particle formation. This structure is particularly relevant in the case of PEO-*b*-P2VP, for which we would expect, but do not observe, a high yield of single particles based on the polymer's high mobility. However, while the 2VP units on PEO-*b*-2VP are initially approximately 30% protonated (at pH 4),[128] the base catalyst added to initiate silane condensation may lead to further deprotonation, rendering the polymer hydrophobic. As a result, the polymer may be acting as a pore-templating agent, allowing metal to escape during, or even after, shell formation. In addition, PEO-*b*-P2VP has a larger molecular weight than PEO (2.8 k g/mol vs. 1.1 k g/mol), and so templates the formation of larger shells (**Table 3.1**),[129] and therefore larger pore sizes, which may also facilitate metal escape. This explanation is consistent with the observation that, in the PEO-*b*-P2VP case, a significant number of unencapsulated particles were observed (three times more than when PEO was used, **Table 3.1**). The low yield

of single particles in the case of PEO-*b*-2VP is largely therefore a result of the significant number of empty shells (approximately 40%), rather than a result of the observation of multi-particle shells as seen in the polymer-free case. Thus, appropriate polymer selection in this context implies the need to balance metal escape with an improved metal atom mobility.

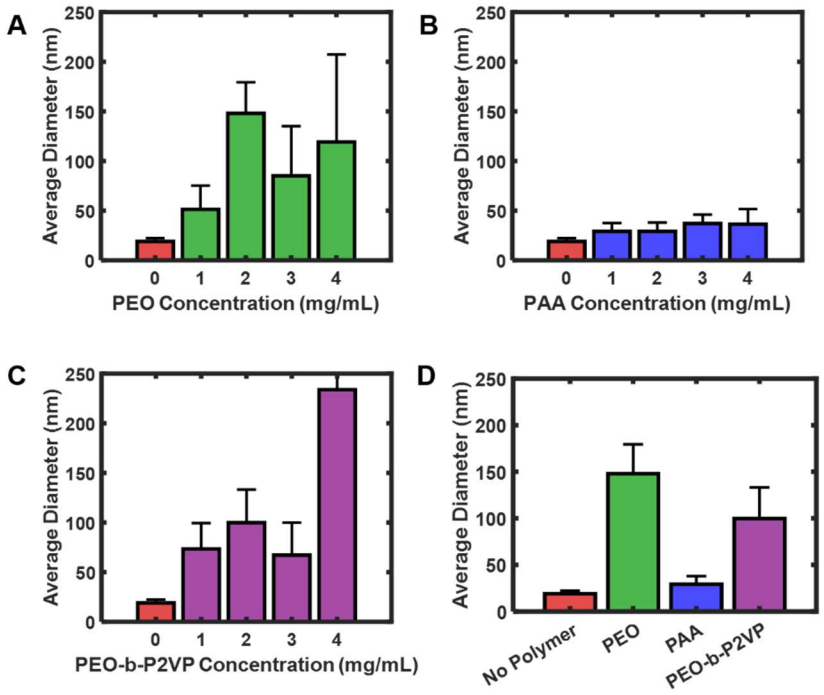

Figure 3.9: Nanoparticle average diameter attained via drop-coating ink on Si/SiO_2 wafers as a function of concentration and polymer type for A) PEO, B) PAA, and C) PEO-b-P2VP. D) Summary figure showing particle sizes as a function of polymer at 2 mg/mL, the same polymer concentration as was used in the experiments with silica shell nanoreactors.

Table 3.1: Summary of Nanoparticle Data for each Ink Type

Ink Type	Single Nanoparticle Yield (%)	Unencapsulated Particles/100 shells	Average Particle Diameter (nm)	Average Shell Size (nm)
No Polymer	6%	0.02	3.1 ± 1.7 nm	36 ± 7 nm
PEO	76%	0.03	5.7 ± 0.7 nm	40 ± 6 nm
PAA	54%	0.04	4.0 ± 1.3 nm	45 ± 5 nm
PEO-***b***-P2VP	50%	0.10	3.6 ± 0.9 nm	46 ± 6 nm

3.5 In situ Observation of Polymer-Enhanced Coarsening within Hollow Silica Shell Nanoreactors

Finally, if polymer-mediated metal nanoparticle growth is facilitated by increased diffusion, coarsening should mainly be observed at temperatures below the polymer decomposition temperature. *In situ* scanning/transmission electron microscopy was performed at discrete temperature steps to determine the effect of annealing temperature on particle coarsening. The *in situ* STEM experiments were conducted in a 10% H_2 environment (90% Ar) at atmospheric pressure using a commercial sealable gas chip and a TEM holder, which mitigates metal evaporation and creates a reducing atmosphere isolated from the high-vacuum environment within the TEM column. In these experiments, silica nanoreactors with metal salts in the absence or presence of PEO were monitored during reductive annealing. The PEO-containing shells were imaged with a lower e-beam dose (120 e/Å^2 vs. 800 e/Å^2) than the polymer-free shells due to e-beam-induced carbon redeposition. After the initial nucleation burst, most particle coarsening occurs by 400 °C (the degradation temperature of the polymer) when PEO is used, and coarsening continues at higher temperatures in the polymer-free case (**Figure 3.10A**). Furthermore, the particle growth rate is significantly larger when PEO is used, especially at temperatures below 400 °C, and a larger average particle size persists thereafter (**Figure 3.10B**). Similarly, after the initial nucleation-burst event where the number of particles per reactor spikes (**Figure 3.10C**), the number of particles drastically decreases and reaches a minimum very rapidly (1.3 ± 0.5 NPs/nanoreactor at T = 300 °C). As the temperature is increased above approximately 300 °C, the number of particles per reactor and particle diameters do not change significantly, defining a polymer-enhanced growth region. In order to control for e-beam-induced coarsening, the process was monitored after reaction completion at a temperature of 700

°C (**Figure 3.10, Figure 3.11**). The slight decrease in average particle size and increase in particles per reactor observed implies a small, but not insignificant, degree of e-beam-induced coarsening, which is more pronounced in the polymer-free case (**Figure 3.12**).

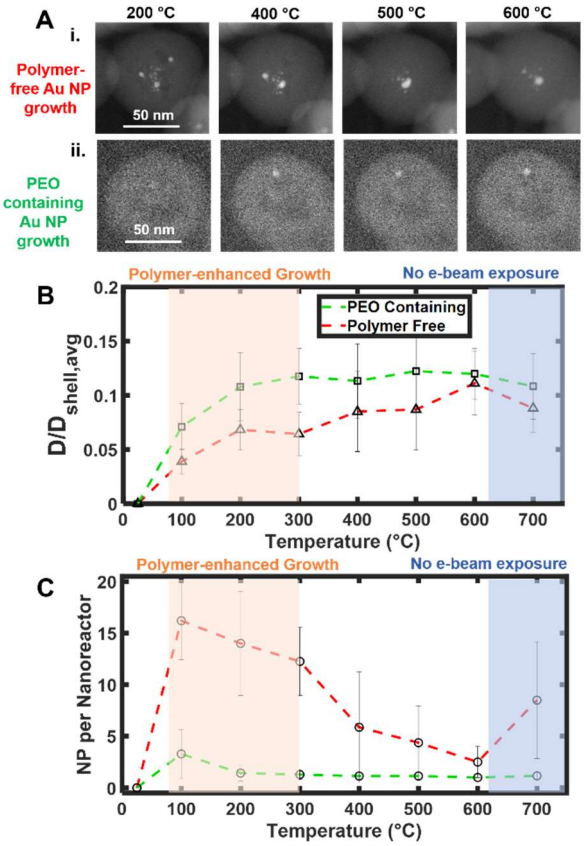

Figure 3.10: *In situ* monitoring of gold nanoparticle growth in a reductive H_2 environment. A) HAADF STEM images monitoring i. polymer-free nanoparticle growth, and ii. PEO-based nanoparticle growth in a specific region as a function of temperature. A decreased e-beam dose was utilized with the PEO-containing system to prevent excessive e-beam-induced sintering and carbon redeposition (120 vs. 800 e/Å^2). B) Nanoparticle relative diameter (divided by average shell size in each case) and C) nanoparticles per nanoreactor as a function of annealing temperature for polymer-free and PEO-containing nanoreactors. A separate region is imaged at 700 °C to examine the effect of e-beam exposure (which is qualitatively large with the polymer-free system).

These data show that the majority of the coarsening in PEO-containing shells occurs at temperatures below the polymer degradation temperature (400 °C), supporting the hypothesis that the polymer matrix facilitates coarsening by promoting diffusion. We have also observed

that PEO promotes reduction at a lower temperature, which may accelerate the process of nucleating metal atoms. Of the two coarsening mechanisms (i.e., Ostwald ripening and particle migration/coalescence), Ostwald ripening tends to dominate at smaller particle sizes immediately after particle nucleation,[57,130] which may explain the rapid decrease in particles per reactor that was observed early on in the annealing process (**Figure 3.10**). Further, based on the classical mean field growth velocity describing particle coarsening, the rate of change of particle size (i.e., the coarsening/growth rate) is linearly proportional to the diffusivity of particle atoms in the surrounding matrix.[131] Thus, it is inferred that increases in the diffusivity at temperatures less than 400 °C leads to higher growth rates and the rapid formation of large single particles (**Figure 3.10, Figure 3.13**), before a drop in the growth rate above this temperature (due to both polymer decomposition and the lack of remaining free gold atoms).

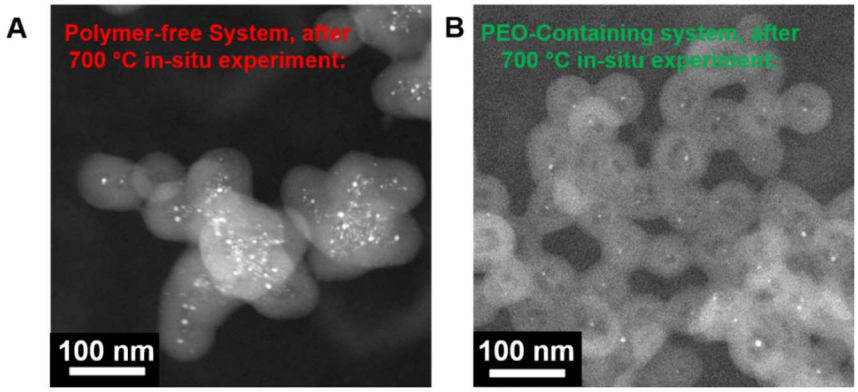

Figure 3.11: HAADF STEM images taken after in situ ramping to 700 °C and holding for 30 mins in a non-e-beam-exposed reference region. A) Without e-beam exposure, the coarsening conditions are not sufficient to drive large single nanoparticle growth within individual shells

without polymer incorporation, due to the shorter annealing times. B) Regardless of e-beam exposure, the PEO-containing system yields large single nanoparticles at 700 °C.

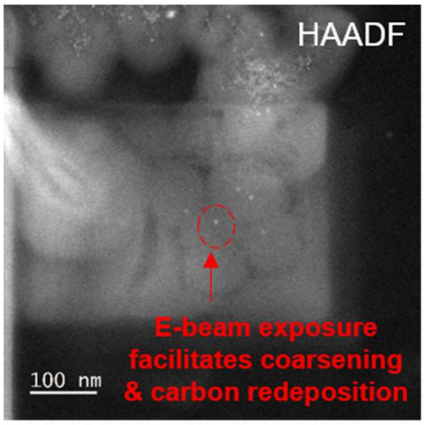

Figure 3.12: HAADF STEM images taken at 60 °C during initial stages of the in situ experiment resulting in significant carbon redeposition as well as gold particle coarsening (clear when compared with the unexposed region). Continuous e-beam examination at high magnification (approximately 1 M x, 15 µA emission current, 200 kV acceleration voltage) appears to significantly challenge the ability to produce results similar to those seen for ex situ experiments.

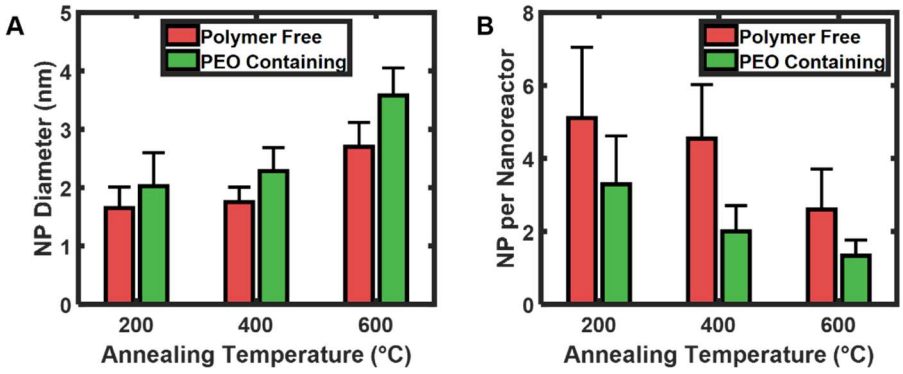

Figure 3.13: Ex situ samples taken with extremely brief annealing times (1 h at maximum temperature) for comparison to in situ data. A) Polymer-containing nanoparticles are larger at every temperature range, indicating that polymer fosters the coarsening process starting at low temperatures. B) The number of nanoparticles per nanoreactor varies significantly in the polymer-free system, while the polymer-containing system quickly produces single particles (although many multi-particle shells remain with these brief annealing times).

3.6 Characteristics of Particle Products With and Without Incorporated Polymer

With the polymer-free shells, it is exceptionally difficult to produce coarsening conditions that yield a monodisperse particle population; at low and intermediate temperatures (T < 750 °C), small freshly nucleated particles form that are not uniform in size, while at high temperatures (T > 750 °C), particles escape and potentially enter adjacent silica shells (**Figure 3.14**). In contrast, polymer (specifically, PEO) incorporation results in particles with uniform sizes at intermediate temperatures (600 °C < T < 750 °C), where particle escape from the silica shell is also prohibited. There is therefore a large temperature range (T < 750 °C) in which these particles can be used, where they remain unaffected by temperature, and do not undergo further coarsening or escape.

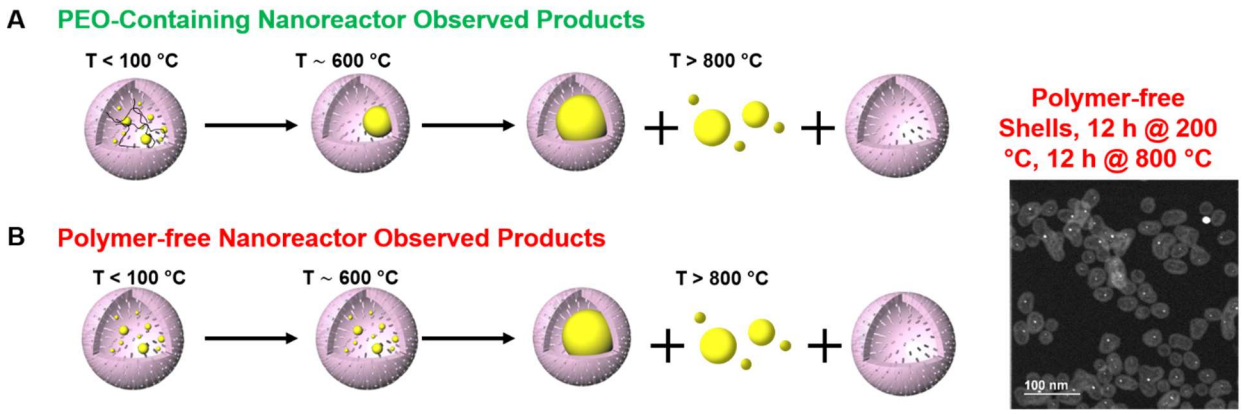

Figure 3.14: Schematic of the observed products with and without polymer. A), B) At low temperatures, nucleation bursts occur, and metal salts are reduced to zero-valent atoms. At intermediate temperatures, PEO-containing shells support complete coarsening into large single nanoparticles, while polymer-free shells retain multiple particles. At excessively high temperatures, global coarsening is promoted, and the particles escape the shells to grow un-templated or enter adjacent shells (regardless of polymer incorporation).

To finally confirm that the polymer residue does not result in dead catalyst, a test reaction of CO oxidation was also performed (**Figure 3.15**), and the temperature necessary to achieve 50% conversion (T_{50}) was significantly lower than that of the control system (310 °C vs. 480 °C), using a low mass-loading (0.001 wt.%). On the basis of this evidence, these polymer-containing

silica shells can be defined as nanoreactors, as control over the degree of conversion of the contents is fully exploited and complete confinement is achieved, while leaving the surfaces intact for downstream applications.

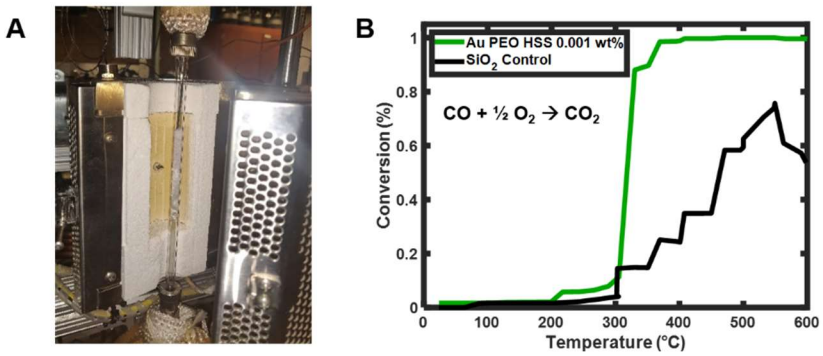

Figure 3.15: Catalytic oxidation of CO in the presence of O_2 over the metal particles was attempted in order to confirm that any polymer residue present in the system does not prevent catalytic activity. Directly after reductive annealing, the PEO containing silica shells are active even at low mass loading of 0.001 wt%, with a 50% conversion temperature of T_{50} = 310 °C, compared to 480 °C for the inert SiO_2 control (representing purely thermal oxidation).

3.7 Experimental Methods

Polymer-Incorporated Hollow Silica Shell Synthesis. Hollow silica shells based on water-in-oil microemulsions were formed by preparing an aqueous ink mixture consisting of gold salt ($HAuCl_4$ x 3 H_2O, Sigma Aldrich, 99.99 %) and aqueous polymer typically in a mass ratio of 2:1 metal to polymer (e. g., 4 mg/mL and 2 mg/mL). The polymer is omitted in the polymer-free systems. The polymers, poly(ethylene oxide) and poly(acrylic acid) (Sigma Aldrich), and poly(ethylene oxide)-*block*-poly(2-vinyl pyridine) (Polymer Source) had molecular weights of 1.1 k, 2 k, and 1.8 k-*b*-1 k g/mol, respectively. The oil solution was prepared by mixing 10 g of n-decane (Sigma Aldrich, 99.9%) with 0.6 g of Igepal CO-520 (Sigma Aldrich), and 0.2 g of n-hexanol (Sigma Aldrich, 99.9%). Practically, larger volumes were mixed to minimize error, and then volumes corresponding to 10.8 g of the oil mixture were aliquoted into 20-mL vials and

stirred. After stirring for 5 minutes, 70 µL of aqueous ink solution was injected, and the sample was stirred for another 5 mins to form a stable microemulsion. The silanes used were tetraethyl orthosilicate (TEOS, 99 %) and (3-aminopropyl)trimethoxysilane (APTMS, Sigma Aldrich, 97%). The APTMS was diluted in ethanol (Sigma Aldrich, 99.5 %) in a ratio of 1:7 silane to alcohol by volume (e.g., 100 µL:700 µL). The two silanes - 40 µL of TEOS and 8.5 µL of ethanolic APTMS - were then introduced to the microemulsion simultaneously. After 2 hours of stirring at room temperature, 100 µL of ammonia hydroxide (Sigma Aldrich, 28-30 %) was added to initiate silane condensation. After three days of stirring, the microemulsion was disrupted with ethanol, and washed twice by centrifugation. The dry solids were then mixed into 15 mL of warm water and stirred at 45 °C for 1.5 hours. Finally, the mixture was isolated by centrifugation and placed in a ceramic combustion boat (Thermo Fisher) for reductive annealing.

Reductive Thermal Annealing. Reductive annealing was performed in a tube furnace (Thermo Fisher) fitted with a quartz tube. The gas was ultra-high purity H_2, flowed at 100 sccm. The annealing process proceeds in two steps (**Figure 3.2A**) - a lower temperature step at 200 °C for 10 hours, and then a higher temperature step at 600 °C for 10 hours. The ramp rates were typically 3-5 °C/min. For the supplemental *ex situ* experiments, the annealing process was drastically shortened to simplify comparison with the *in situ* experiments, and the higher temperature annealing step was only performed for 1 hour (**Figure 3.11**). This change introduces some error because the time spent ramping and cooling (1-2 h) is approximately as long as the annealing time, and with non-forced/natural convective cooling processes, the total heat transfer applied during ramping and cooling for the high temperature *ex situ* measurements is likely larger than desired.

Bulk Characterization. X-ray photoelectron spectroscopy (XPS, Thermo Scientific ESCALAB 250XI) experiments were performed on particles within silica shells deposited on flat silicon wafers. A standard XPS workflow was followed,[89] and charge compensation was enabled. The peaks were all shifted using the carbon 1s peak to calibrate the peak position and determine the oxidation state. Thermo Fisher Avantage software was used to identify the different chemical states. X-ray diffraction (XRD, Rigaku Ultima) data was collected using a Cu Kα source and compared to the ICDD's online powder diffraction file, PDF: 01-071-4073. UV-vis (Agilent Cary-60) data were collected using dilute solutions of the unannealed or reduced particles in silica shells. Surface area and pore-size distribution measurements were collected using N_2 adsorption and desorption isotherms (Micromeritics, 3Flex) at 77 K. The specific surface area was determined using the Brunauer−Emmett−Teller (BET) model from the N_2 sorption data. Pore size distributions were obtained using the Barrett-Joyner-Halenda (BJH) method. Contact angle goniometry (Rame-Hart Instruments) was used to investigate the wetting properties of the dilute metal-polymer mixtures. Thermogravimetric analysis (TA instruments, Discovery) on the polymer inks was conducted in a N_2 environment with a 10 °C/min ramp rate. Temperature programmed reduction (Altamira, AMI-200) was accomplished in a quartz U-boat with a flow rate of 30 sccm H_2 in N_2 (10%), and a ramp rate of 10 °C/min. The effluent was monitored using a sampling mass spectrometer (Stanford Research Systems, Universal Gas Analyzer MS). Inductively-coupled plasma optical emission spectroscopy (Thermo iCap7600 ICP-OES) was used to quantify the metal loading. The catalytic oxidation was achieved in a packed bed reactor (Altamira, BenchCat 4000) with an inline gas chromatography sampling the effluent (Agilent 7890A GC).

Scanning and Scanning Transmission Electron Microscopy. The nanoparticle-containing silica shells as well as the nanoparticles themselves were characterized by scanning electron microscopy (SEM) (Hitachi SU-8030), using an accelerating voltage of 5 kV, operating current of 20 μA, and working distance of 2 mm. Scanning transmission electron microscopy (STEM) images were taken with either a Hitachi HD-2300 STEM or an aberration-corrected JEOL JEM-ARM 200CF S/TEM. Both microscopes operate with an acceleration voltage of 200 kV. Energy dispersive X-ray spectra were collected using the ARM 200CF. The Lα peaks of Au and the Kα peaks of Si and O in the energy-dispersive x-ray spectroscopy (EDS) spectra were used for elemental mapping.

***In Situ* Reductive Annealing.** The *in situ* gas experiments were carried out using an aberration-corrected JEOL JEM-ARM 200CF S/TEM, using a commercially available gas-delivering TEM holder (Protochips Atmosphere gas system). This microscope was equipped with a cold field emission gun and dual EDS silicon drift detectors. Before assembly, the two wafer-chips used for imaging the samples were cleaned with methanol and acetone before being plasma-cleaned in O_2 for 1.5 mins at 30 W to render them hydrophilic. The inner surface of one chip was used to disperse the sample and then it was sandwiched with a second chip, which seals against an elastomeric O-ring. The gas lines were purged using ultra high-purity (UHP) Ar gas in a pump/purge process. The samples were imaged at room temperature, and then a pre-bake process was applied, where O_2 was introduced at 0.1 sccm, 760 torr to the holder, and the system was warmed to 80 °C at 1 °C/s to purge any adventitious carbon. This process drastically decreases carbon build-up during imaging. The polymers within the silica shells do not degrade in this temperature range (**Figure 3.2B,C**). After that step, 10 % H_2 in 90% Ar process gas was introduced at 0.1 sccm and 760 torr, and heated at 0.45 °C/s to each set point temperature (e.g.,

100 °C, 200 °C) for imaging. Due to challenges with carbon build-up, and e-beam-induced coarsening during continuous monitoring (**Figure 3.11**), the samples were imaged only at set intervals of temperature. After heating to the final temperature, the images were collected outside of the region directly exposed to the e-beam for comparison. STEM imaging convergence angle and high angle annular dark field (HAADF) image collection angle ranges were 27.5 or 20.6 mrad, and 90-370 or 68-280 mrad for the polymer-free and polymer-containing systems, respectively. The emission current was 15 μA, with a constant acquisition time of 20.97 s. At a magnification of 500k, the e-beam dose was therefore approximately 800 e/Å^2. Due to carbon build-up in the polymer-containing silica shells as well as to minimize any e-beam induced coarsening, these samples utilized a slightly lower e-beam dose (with a smaller convergence angle and lower image magnification of 300k), resulting in a nominal dose of approximately 120 e/Å^2.

3.8 Conclusions and Outlook

This work establishes polymer incorporation as a means to control particle coarsening within hollow silica shell nanoreactors. At all of the annealing temperatures studied, in the polymer-free systems, the precursors are not converted into single particle products, and incomplete confinement and particle escape occurred. Our results show that both the metal precursor and polymer must be present for enhanced coarsening to occur (whether in confined or unconfined volumes, under the conditions explored), supporting the argument that enhanced diffusion through the polymer matrix drives particle coarsening. Finally, by looking at three different polymers in this synthesis scheme, it was discovered that for the polymer to mediate single-particle coarsening in the nanoreactors, it must promote metal atom diffusion while not adversely affecting the structure of the microemulsion. Taken together, these experiments provide design

rules for preparing effective nanoreactor systems, as well as offer a method to improve the uniformity of single particle products within hollow silica shell reactors. Given the large number of downstream experiments or applications where fine-control over particle structure is important while remaining scalable (e.g., catalysis, optics), this methodology may become useful towards preferentially forming desired complex particles.

CHAPTER FOUR

Fabrication of a Reactor cell and Capillary Probe towards Rapid Discovery of Heterogeneous Catalysts

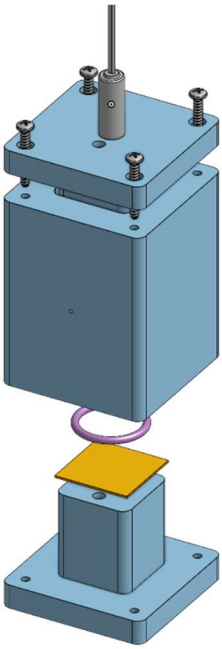

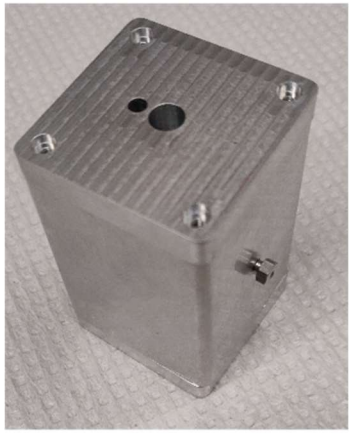

4.1 Introduction

Measuring the catalytic properties of multicomponent particles synthesized by SPBCL has only been demonstrated in isolated situations, such as for carbon nanotube growth,[74] nitrobenzene hydrogenation,[70] and electrochemical catalysis (i.e. hydrogen evolution reaction).[73,107] Thus far the gas-phase catalytic properties have not been demonstrated. The challenge stems from the lack of active sites available for catalytic turnover, the planar substrate geometry, and therefore the challenges associated with measuring the gaseous products. The small number of total active sites results from the low maximum achievable particle density on the planar substrate ($\sim$1 NP/μm^2)[70]. If a 2 cm × 2 cm wafer is completely coated with particles patterned by PPL, the total number of active sites are still saturated with a large excess of gaseous reactants, not to mention a significant likelihood of gas-slip over the planar geometry.[5] Further, one of the most promising elements of the SPBCL system is the ability to fabricate libraries of unique materials with varying size and composition.[74] However, the challenge of probing the gas-phase reactivity of these particles is further exacerbated when the goal is to probe the reactivity of a small portion of the wafer, rather than measuring the wafer as a whole.

To address this challenge, the following two chapters introduce a strategy to measure the gas-phase catalytic turnover of complex nanoparticles synthesized by SPBCL. The challenge therein consists of firstly fabricating a reactor cell to probe the wafer as a whole, or probe local regions of the wafer if a library of materials has been patterned upon it. The second challenge consists of designing a technique to increase the concentration of the products in the effluent gas-stream, as the typical product concentrations are often in the ppb range, below the detection limit of most conventional strategies (e.g. GC/MS, FTIR).[5]

4.2 Design of a High Temperature Reactor Cell for Planar Catalysts

Understanding the design constraints for the gas-phase reactor cell begins with understanding the SPBCL wafer and particles it supports. In a conventional SPBCL synthesis based on PPL,[74] nanoparticles are patterned onto a silicon wafer, with a particle density of ~1 NP/μm^2. The particles can be patterned such that they are all homogenous in composition, or such that a gradient in composition is present in one dimension, and a size gradient is present in the other dimension. The first demonstration of a gas-phase reactor cell begins with measuring the reactivity of a homogenous wafer with all the same composition and size.

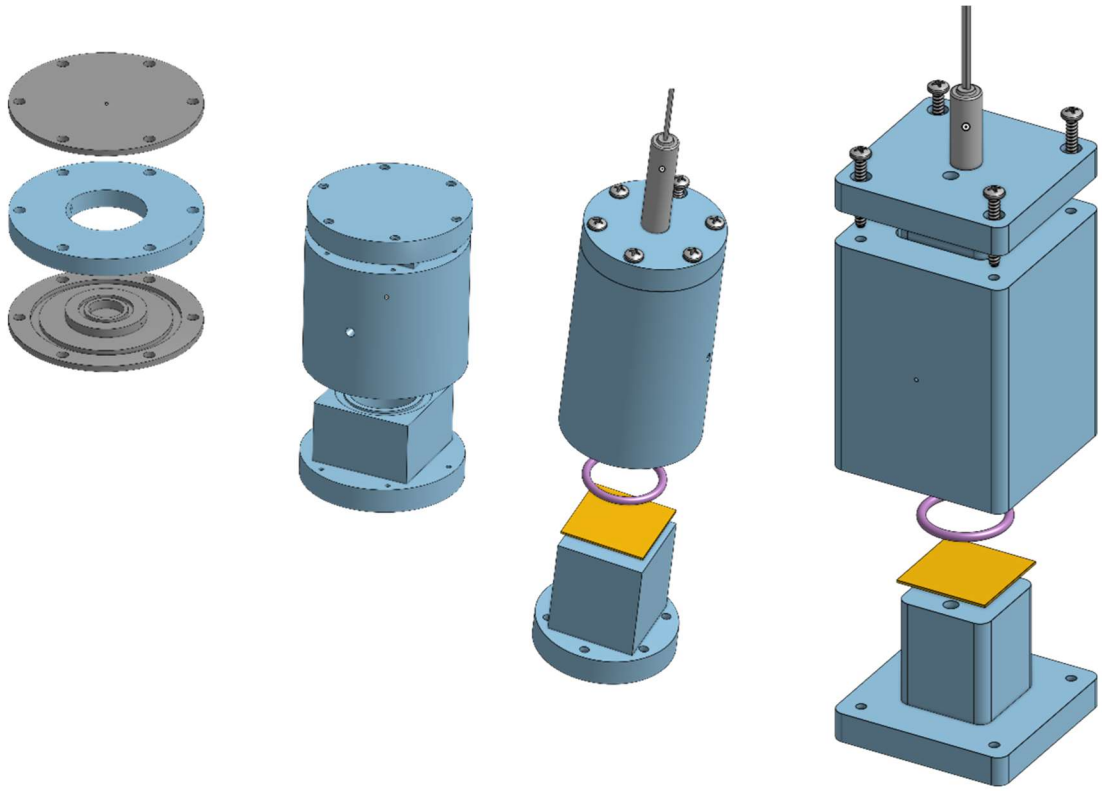

Figure 4.1: Evolution of the reactor cell design, with the final iteration being a symmetrical 'sandwich' design, which presses two homogenous SPBCL-coated wafers towards the interior and flows gas through a cavity in the middle.

Several design constraints were applied to facilitate the fabrication of such a gas-phase reactor cell. Firstly, the interaction between the gaseous reactants and the wafer substrate should be maximized, to minimize the degree of slip (gas which does not interact with the particle surface).

Further, the reactor cell must be amenable to heating in order to increase the turnover frequency to a measurable range. Finally the cell should allow low-pressure gases to be circulated without leaks from the external environment, as these can interfere with the gas-concentrating step down-stream and detection processes.

The design of the reactor cell commenced with several designs investigated (**Figure 4.1**) including two wafers facing externally, compared to two wafers facing internally. The final design was a symmetrical 'sandwich' design, which is rectangular on the external faces to facilitate machining. The components and final design are listed in **Figure 4.2**.

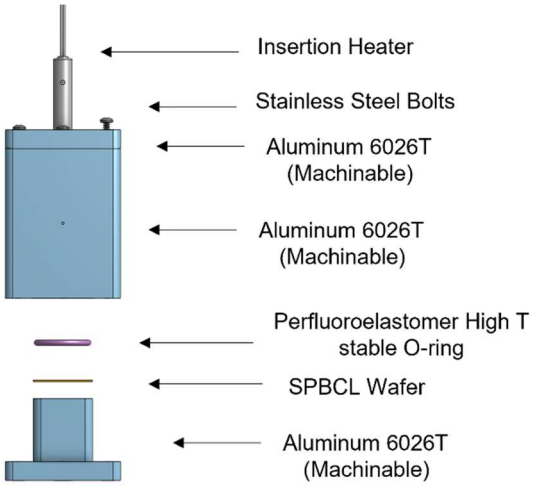

Figure 4.2: Components and materials for aluminum reactor cell machined to hold two SPBCL wafers, and seal on the surface of the wafers. All materials are high temperature compatible, and a thermocouple probe (not shown) can be inserted next to the insertion heater.

The reactor cell as designed is high-temperature stable to 600 °C at least, given the perfluoroelastomer O-ring and all metal/ceramic components included. The cavity within the cell

allows gas to be flowed through a 1/32” hole drilled with a proprietary fitting (Valco Instruments). The symmetrical reactor top/bottom and the reactor middle are displayed in **Figure 4.3**.

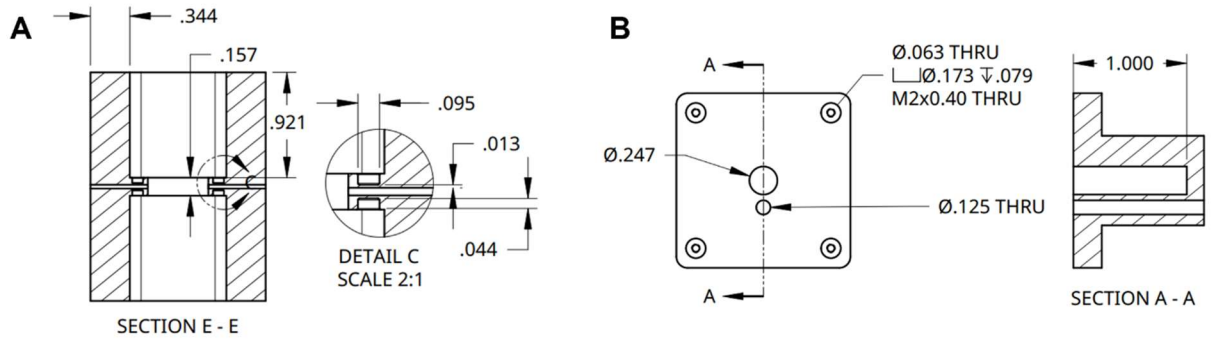

Figure 4.3: Reactor schematics with dimensions listed in inches. A) Reactor middle cross-section, and a section view detail of the gas inlet. B) Reactor top/bottom drilled such that two holes are available for an insertion heater (central blind hole) and thermocouple (off axis thru hole) respectively.

The cell as designed enables isolation of the SPBCL particle-coated wafers from the ambient atmosphere, followed by continuous flow of low pressure gas with low concentrations of reactants (~5 psi range, 100 ppm – 1% range). This ensures that low product concentrations in the 100 ppb – 10 ppm range will not be overwhelmed by the background from the reactants regardless of detection scheme (GC/MS, FTIR etc).

4.3 Experimental Realization of High Temperature Reactor Cell

The reactor cell as designed was custom-machined by a commercial machine-shop (Xometry Ltd), and the specialty small dimension ports were drilled at 1/32” dimensions with tight tolerance commercially as well (Valco). The resulting reactor cell looks as shown in **Figure 4.4**.

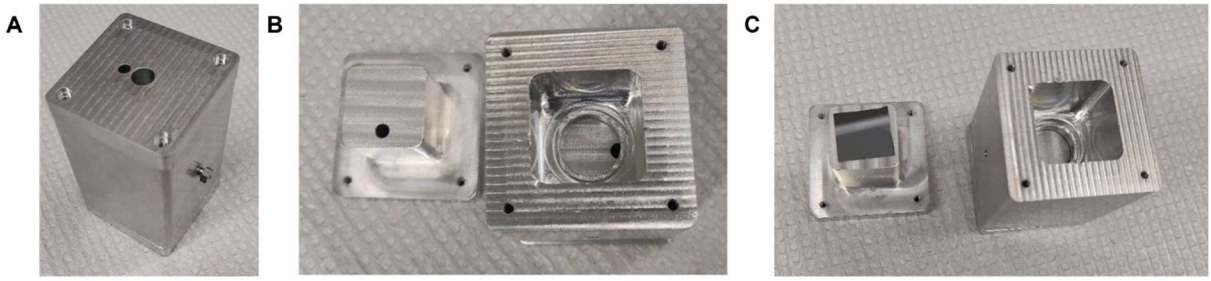

Figure 4.4: Photographed images of the as fabricated custom reactor cell. A) The reactor cell as closed, with a side-port for inlet gas displayed, and top ports for a thermocouple and insertion heater. B) Images of the reactor cell upon opening, with an O-ring groove and seat for each wafer visible. C) The wafer sits on the reactor top as shown and can be inserted smoothly into the reactor cell.

As visible in the photographs, the machined aluminum cell mates well, and can be sealed with a silicon wafer cut to size within.

4.4 Capillary Probe-based Gas-Phase Catalysis for High Throughput Screening

Finally, the isolation of two wafers with an identical particle composition for gas-phase reaction is an exciting endeavor. However, in order to study the reactivity of a library of materials towards high-throughput discovery of superb catalysts, the proposed strategy must be extended.

To address this challenge, a capillary-tube based distribution system is suggested, which would be suitable for locally releasing reactants and then probing the products locally as well.

The working mechanism involves a pair of concentric gas tubes, the inner tube delivers gas at a low total pressure towards a SPBCL wafer substrate. The gases react on the surface of the particles, and then they are pumped back into the second outer tube capillary which is at a lower relative pressure. The entire chamber must operate below atmospheric pressure, again to create a product concentration which is within 3 orders of magnitude of the reactant concentration (in the effluent). The detailed schematic is shown in **Figure 4.5**.

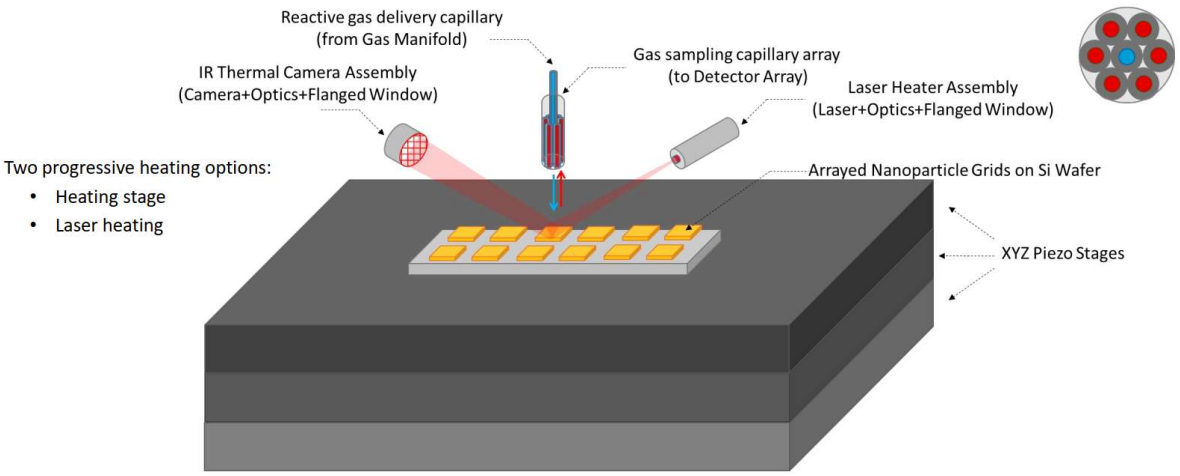

Figure 4.5: Schematic of the operating principle for the low pressure capillary-sampling system for rapid-screening of the gas-phase reactivity of SPBCL wafers. Top right inset is the cross section of the capillary tube, with one gas-delivery tube in the middle, and several sampling tubes arranged concentrically.

As displayed, the local capillary tube method as described seeks to address the challenge of local screening of a library of diverse materials, but the low pressure environment of the capillary-based probe requires further design consideration. In this setup, the heating mechanism must be either amenable with a vacuum and highly oxidizing or reducing conditions (in the presence of the reactive feed gases). Thus a view-port and halogen lamp are the preferred strategy, with the focal length optimized for heating at the surface of the SPBCL wafer (roughly 10 cm away), and can heat to a temperature of 800 °C, although these temperatures are not practically necessary.

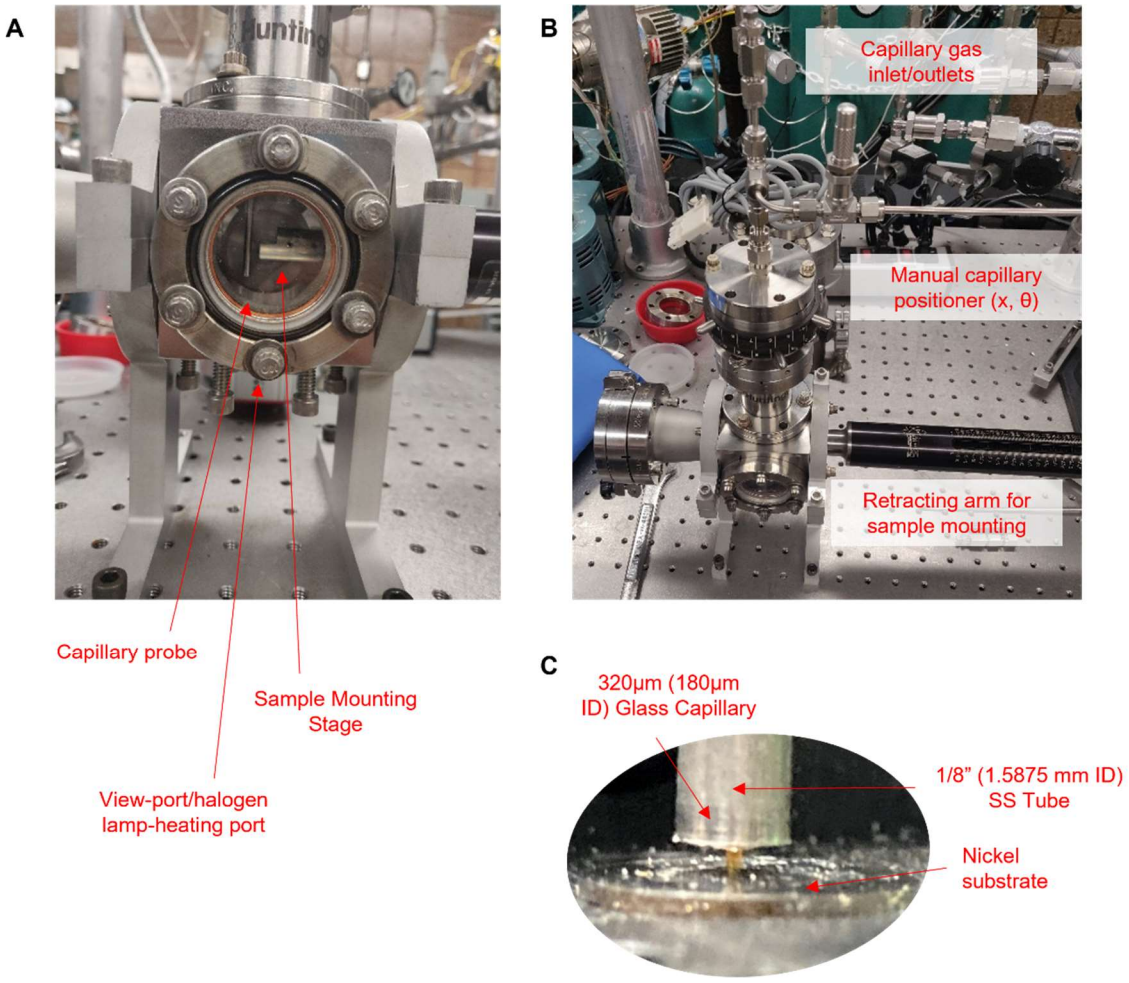

Figure 4.6: A), B) Fabrication-stage build of practical capillary probe for SPBCL planar catalyst, with a retracting arm for loading individual wafers. Capillary gas inlets can be delivered from an upstream manifold, and the capillary positioner allows manual positioning of the gas-stream position. C) Higher magnification image of the concentric capillary tube over a nickel substrate.

4.4 Conclusions and Outlook

Several key challenges remain towards the practical implementation of these reactor cells for gas-phase detection of SPBCL products. Firstly, the engineering challenges associated with implementing the custom reactor cells as designed is non-trivial, not to mention the practical question of the total time necessary to finally detect gaseous products. To minimize the time associated with these experiments, the following chapter will describe how a down-stream concentrator of product molecules can accelerate the measurement of gas-phase reactivity.

CHAPTER FIVE

Cryogenic Distillation for Detection of Low Concentration Reaction Products

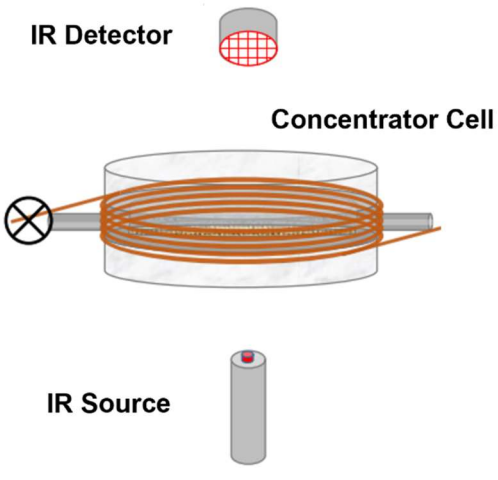

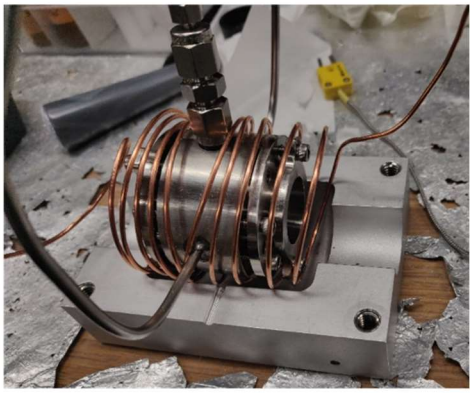

5.1 Introduction

In a continuous-flow setup, if the products are not of a high enough concentration to be measured by conventional products detection schemes, several strategies can be employed to address the challenge. Firstly, a reflux process can be applied to turn the system into a 'batch' setup effectively rather than continuous flow, in which case the reactant turnover should approach the equilibrium concentration as a function of time after multiple feed-throughs.[5,8,132] Alternatively, a separation process can be applied to the effluent stream, with the goal of isolating the products from the reactants to facilitate subsequent detection.[133] Of various separation strategies, one promising option is cryogenic distillation, which seeks to separate materials based on their boiling point, which is a function of the vapor-liquid equilibrium that develops in a mixture of disparate gases.[134] In particular, we propose distilling the gaseous reactants and products from the balance gas (e.g. He) which condenses at a significantly lower temperature (4 K) than the reaction gases.

5.2 Probing Low-Density Planar Catalyst Substrates via Cryogenic Distillation

The strategy to implement the cryogenic distillation of the reaction products is depicted visually in **Figure 5.1**. As evident from the schematic, after gaseous products are produced from the SPBCL catalytic particles, they are sent to the low temperature concentrator cell, where they can be isolated from the balance gas (He). In this context, the reaction of choice was 1-butene hydrogenation. This reaction was selected because the reaction is structure sensitive, depending on the catalyst surface,[135] it also results in isomerization reactions which are structure dependent and may require selectivity control,[135–137] and finally the condensation temperature of 1-butene and n-butane are both significantly distinguished from He (~270 K vs. 4 K).[135]

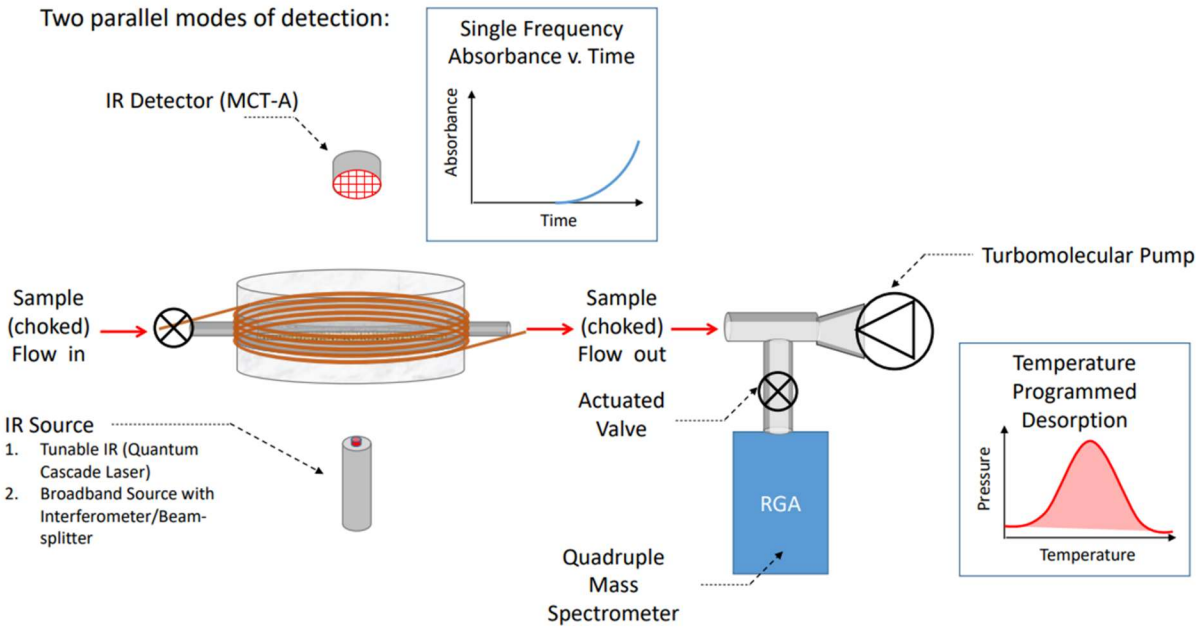

Figure 5.1: Schematic illustration of the operating mechanism for selective gas-phase adsorption and detection of both reactant and product molecules. After reaction on a catalytic surface, the reactant-product mixture is directed into the concentrator cell, which at low temperature enables condensation of the reaction gases. These molecules can be detected with infrared spectroscopy. Upon heating the molecules can be desorbed and measured by mass spectrometry.

Within the concentrator cell, a non-reactive species must be installed with a high surface area that is IR transparent, in order to facilitate the adsorption of gases. Based on our experiments, Nanodur (Durcrete Inc.) an alumina powder (SA ~10 m^2/g) was suitable for this role.

5.3 Experimental Setup for Infrared Spectroscopy-based Gas Concentration and Detection

The experimental demonstration of cryogenic gas distillation is represented pictorially in Figure x. The distillation of 1-butene proceeds in effectively 5 steps: 1) the concentrator cell is heated under Ar to 100 °C to sparge any adsorbates and water that may be on the adsorbent surface. 2) The concentrator is cooled to below the condensation point of the reactants and all products while flowing Ar continuously. 3) The reaction gases (or pure 1-butene in this proof-of-concept) are introduced to the reactor at low temperature (e.g. −20 °C) and the infrared spectrum (FTIR) of

the cell is monitored continuously. 4) After the gas appears to have saturated the surface of the adsorbent, Ar is spurged into the cell to remove any multilayers or molecules trapped in the cell in the gas phase, leaving only the condensed liquid. 5) The cell is heated under Ar which is applied rapidly should release the gases at a high enough pressure to be detected down-stream by mass spectrometry (MS).

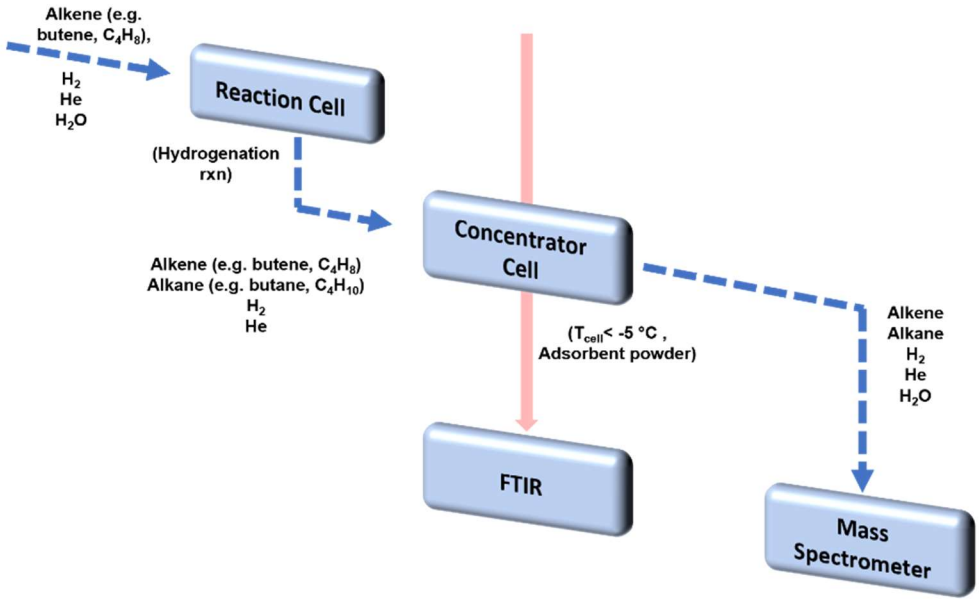

Figure 5.2: Schematic illustration of the operating principle of the gas-concentrator in the context of butene hydrogenation.

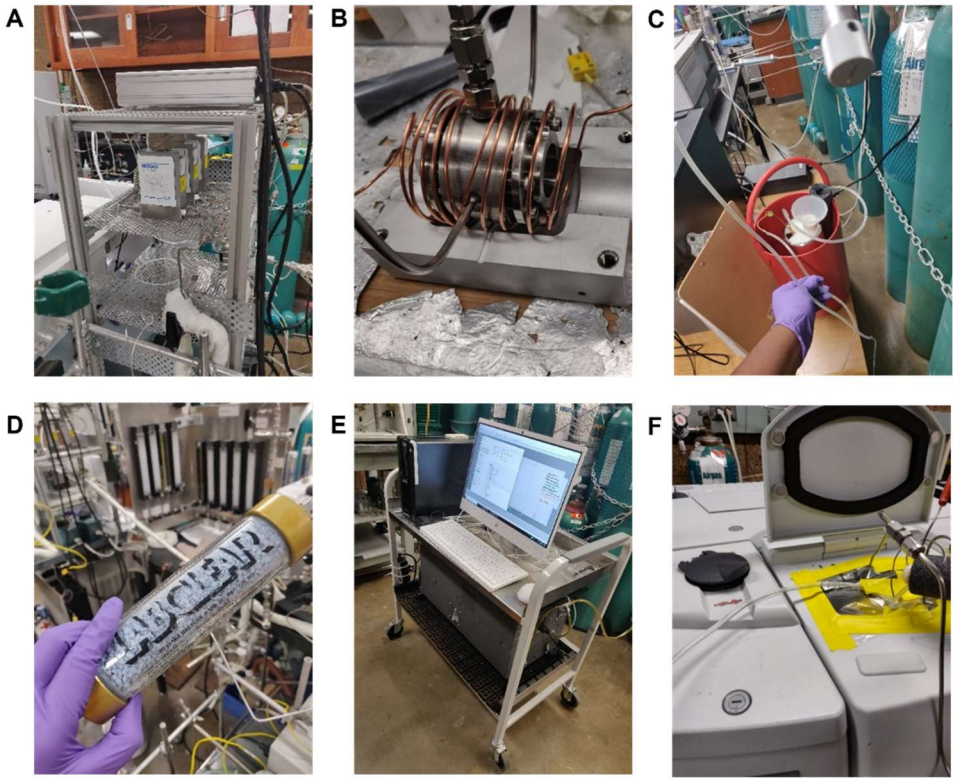

Figure 5.3: Photographs of the concentrator cell and peripheral equipment. A) Mass-flow controllers and manifold supply gases to the concentrator cell. B) Concentrator cell, with thermocouple inserted from above, and gas inlet/outlet supply on either end. Along the long axis are windows which allow IR spectroscopy. Copper coiling enables refrigeration of the cell to −20 °C. C) A precooling stage for inert gas supply to the IR chamber which houses the cell. D) Dessicant removes water from the inlet gases. E) Downstream MS measures outlet mass fragments. F) Final image of the IR setup as designed.

5.4 Demonstration of Selective Adsorption and IR Detection of n-Butene

Upon building the concentrator cell apparatus, the system was applied to detect the gas-phase adsorption of 1-butene by cryogenic distillation/condensation. Upon desiccation to remove water, the gas source contains 1-butene and He only. The experiment proceeds via the 5-step procedure described previously, which involves evolving residual H_2O from the adsorbent surface followed by locally condensing liquid 1-butene on the alumina surface. The stages can each be observed by FTIR, with stages 2 and 3 displayed in **Figure 5.4**.

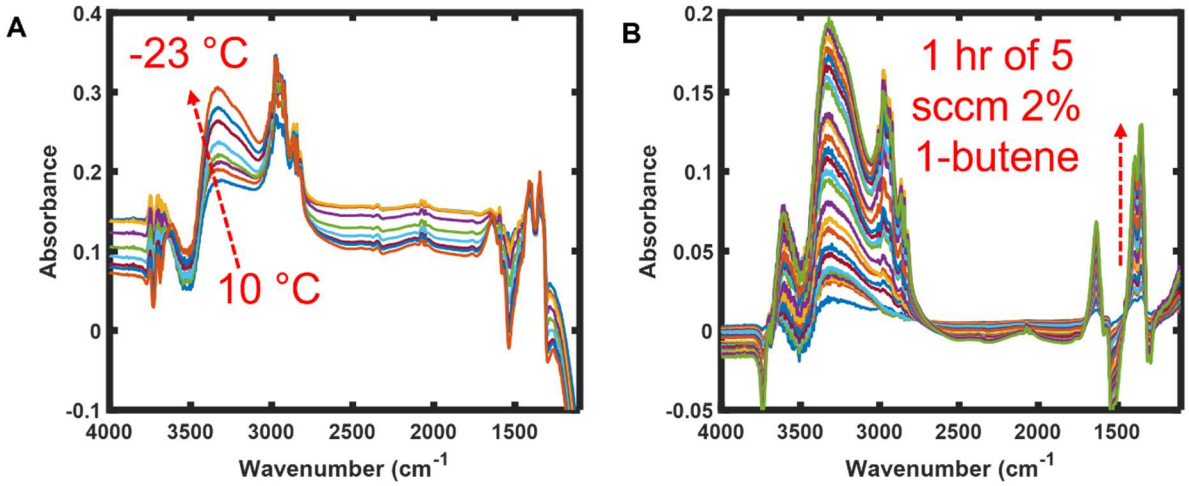

Figure 5.4: A) During cooling, small changes in the background spectra occur, which can be monitored by FTIR until they stabilize near −20 °C. B) Switching from Ar to 1-butene monitored by FTIR. The appearance of peaks corresponding to the 1-butene condensate arrive and stabilize over the course of 1 hr.

The background spectrum is collected as a function of temperature in order to subtract any effects of temperature on the IR stretch of the powder (alumina) and windows (CaF_2). As evident from the figure, the absorption peaks near 1400 and 3000 cm^{-1} corresponding to 1-butene[137] can be clearly seen to appear and grow after low-temperature introduction to the concentrator-cell. The spectral changes do not appear to change significantly after 50 mins to 1 hr under 1-butene, indicating the majority of surface sites are saturated.

A representative spectra can be taken at each step, to simplify identification of the 1-butene condensed within the concentrator cell **Figure 5.5**.

As evident from the time-series shown, at −23 °C under Ar there are no peaks present corresponding to 1-butene. However, the peaks arrive after saturating in butene, and persist even after Ar purging for 25 m. This implies that the peaks associated with 1-butene must be emerging from the liquid condensed phase, as all gaseous butene should be sparged by this point. This concept is supported by the observation that as the temperature is increased *in situ* using a resistive

heater, the peaks remain until the boiling point of butene, but disappear upon further heating to 45 °C.

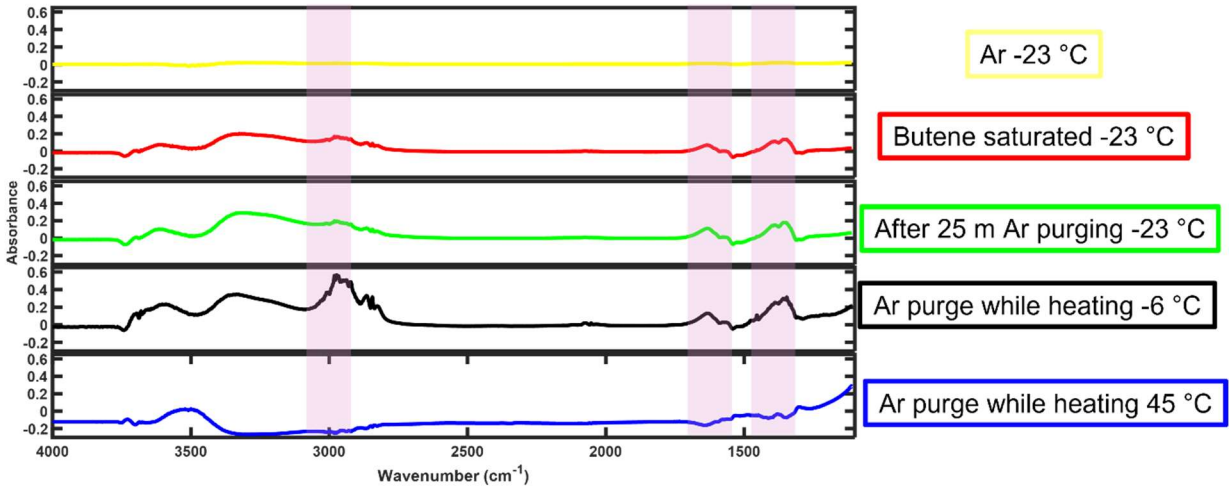

Figure 5.5: Time-steps of butene introduction to the concentrator cell overlaid. The appearance of peaks corresponding to 1-butene are evident in the spectra at −23 °C and are persistent even after the switch to Ar for 25 mins. The peaks have disappeared after heating to 45 °C.

5.5 Generalized Low-Temperature Accumulation and Detection of Gaseous Products

Gas concentrating while simultaneously detecting the products using IR spectroscopy is practically challenging, given a) the small dimensions of a concentrator cell suitable to fit within a commercial IR spectrometer, 2) the need for low pressure and low temperature compatible windows that seal and 3) the requirement that the total absorption from adsorbent and windows cannot contribute too significantly to the background preventing product detection. These challenges suggest that although cryogenic distillation appears to help isolate molecules for IR detection, various alternative detection schemes post-distillation may be suitable. For example, one option is to simply condense the reaction gases in the a condensing column followed by releasing the outlet in a rapid burst towards a GCMS. This strategy is perhaps somewhat more

general, sacrificing in-situ observation of the accumulation of products for a more facile experimental procedure (**Figure 5.6**, **Figure 5.7**).

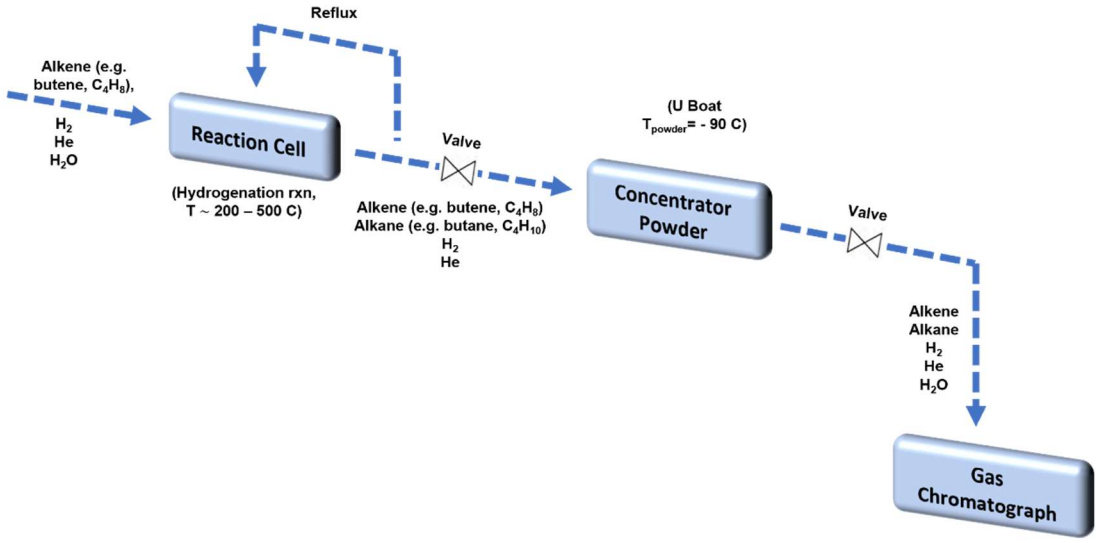

Figure 5.6: Schematic illustration of the operating principle of the gas-concentrator with an aluminum 'u-boat' replacing the IR-compatible concentrator cell.

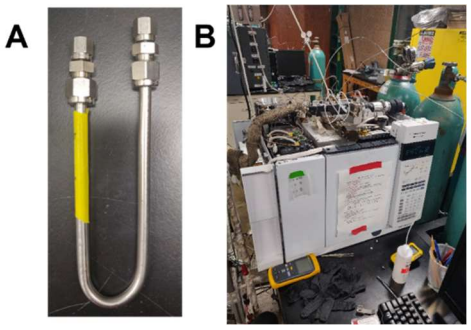

Figure 5.7: A) U-boat style cell containing 500 mg p25 TiO_2 adsorbent, suitable for adsorption of gas-phase products during cryo-condensation. B) Gas-chromatograph for down-stream separation of reactants and products.

5.6 Conclusions and Outlook

The concentrating mechanism described here appears to be quite robust, and has been demonstrated to effectively condense 1-butene within a reasonable time-frame of approximately 1 hr. However, a key challenge pertains to decreasing the total amount of time necessary to condense

the products desired. As the total pressure decreases, and the concentration of products decrease, the time necessary to condense a measurable amount of 1-butene will increase. In order to address this challenge, some possible strategies may be: 1) increase the surface area of the adsorbent, 2) decrease the temperature of the adsorbent, 3) redesign the concentrator cell to minimize slip around the adsorbent. These strategies all seek to accelerate the accumulation of products, and the use of the U-boat style large-scale concentrator may facilitate this experiment as well. The preliminary demonstration of accumulation of 1-butene from a 2% feed is a key first step, and depending on the reactivity of the particles in question, the concentrator as-designed may be suitable for condensing liquid phase products in a tenable time frame.

CHAPTER SIX

Conclusions and Outlook

At its heart, nanoreactor templated particle syntheses serve to democratize the field of nanoparticle synthesis and create opportunity for innovation from a variety of researchers with interests in materials chemistry, but potentially lacking a synthetic chemistry background. In this same vein, the research described here has focused on modular techniques that extrapolate lessons learned from solution-phase chemistry to decrease the barriers to robust nanomaterial synthesis.

In the context of anisotropic nanoreactors, key developments included the ability to synthesize a variety of nanomaterials without material-specific process development, while also increasing the scale and throughput of the procedure. Further, fundamental insight was developed on the ideal nucleation position of the particles synthesized, with potential for unprecedented control over particle position in an array. The work therein can be extended to multicomponent particles, but the key challenge of characterizing the complex particles synthesized remains difficult to overcome. Despite being conceptually amenable to synthesis of polyelemental systems, obtaining experimental evidence remains difficult, serving as an opportunity for development in the future.

In the context of hollow shell nanoreactors, the incorporation of polymer has been shown to be a key driving force for coarsening, validating many assumptions about the SPBCL system. The ideal nanoreactor in this context was determined to be one that can both 1) isolate the reactor contents effectively and 2) facilitate coarsening as effectively as possible within the reactor. Indeed, intra-reactor metal atom diffusion must be facilitated while inter/extra reactor diffusion must be strictly limited. This is a recurring theme within the field of nanoreactor-templated particle synthesis, and key to experimental realization of a high yield of individual particles within each reactor. Further avenues for study again consist of extension to multicomponent systems, but in this context, challenges pertain to ensuring metal atoms remain localized within the shells, while

still being able to coarsen into an individual particle. Preliminary results indicate that this may be feasible, but a robust experimental demonstration is required.

Finally, the engineering challenges associated with detecting minute amounts of gaseous products from SPBCL planar catalysts have been tackled, with preliminary results reported here. A gas-phase reactor cell, capillary probe for particle library screening, and concentrator cell for accumulating gas-phase products are all described to facilitate this goal. The vision for this project is the ability to screen a library of particles of varying size and composition for their gas-phase reactivity, and in so doing drastically accelerate the ability to both find exceptional catalysts and learn new structure-function relationships. However, the practical realization of this goal requires further engineering development. Catalyst discovery by sequential measurement of a variety of multicomponent particles is an exciting intermediate step, and these experiments are potentially quite close to reduction to practice.

Overall, the lessons learned here merely scratch the surface with regards to opportunities for further development in nanoreactor-based synthesis. In the future, one area for further meaningful development will be further extension of the ‘designer nanomaterial’ concept, towards multicomponent particle synthesis with precise, countable numbers of atoms, each in predetermined lattice positions, and a defined global crystal habit. Another area for investigation will be rapid synthesis and screening of nanomaterials for enhanced catalytic, optical or electronic properties. Besides contributions in the engineering of compatible screening platforms, key progress must be made on selection rules for which materials to incorporate within the library. This insight may be delivered from the materials prediction, theory, and artificial intelligence communities which can aid in short-listing materials, and rapid redesign of experiments to

efficiently probe the material-space. I look forward to learning how these research directions unfold.

REFERENCES

(1) Turkevich, J.; Stevenson, P. C.; Hillier, J. A Study of the Nucleation and Growth Processes in the Synthesis of Colloidal Gold. *Discussions of the Faraday Society*. 1951, pp 55–75. https://doi.org/10.1039/DF9511100055.

(2) Haruta, M.; Kobayashi, T.; Sano, H.; Yamada, N. Novel Gold Catalysts for the Oxidation of Carbon Monoxide at a Temperature Far Below 0 °C. *Chem. Lett.* **1987**, *16* (2), 405–408. https://doi.org/10.1246/cl.1987.405.

(3) Deutschmann, O.; Knözinger, H.; Kochloefl, K.; Turek, T. Heterogeneous Catalysis and Solid Catalysts. In *Ullmann's Encyclopedia of Industrial Chemistry*; Wiley-VCH Verlag GmbH & Co. KGaA: Weinheim, Germany, 2009. https://doi.org/10.1002/14356007.a05_313.pub2.

(4) Ciriminna, R.; Falletta, E.; Della Pina, C.; Teles, J. H.; Pagliaro, M. Industrial Applications of Gold Catalysis. *Angew. Chemie Int. Ed.* **2016**, *55* (46), 14210–14217. https://doi.org/10.1002/anie.201604656.

(5) Kakaei, K.; Esrafili, M. D.; Ehsani, A. Introduction to Catalysis. *Interface Sci. Technol.* **2019**, *27*, 1–21. https://doi.org/10.1016/B978-0-12-814523-4.00001-0.

(6) Weststrate, C. J.; Van Helden, P.; Van De Loosdrecht, J.; Niemantsverdriet, J. W. Elementary Steps in Fischer–Tropsch Synthesis: CO Bond Scission, CO Oxidation and Surface Carbiding on Co(0001). *Surf. Sci.* **2016**, *648*, 60–66. https://doi.org/10.1016/J.SUSC.2015.10.050.

(7) Meunier, F. C. Bridging the Gap between Surface Science and Industrial Catalysis. *ACS*

Nano **2008**, *2* (12), 2441–2444. https://doi.org/10.1021/nn800787e.

(8) Cao, A.; Lu, R.; Veser, G. Stabilizing Metal Nanoparticles for Heterogeneous Catalysis. *Phys. Chem. Chem. Phys.* **2010**, *12* (41), 13499–13510. https://doi.org/10.1039/c0cp00729c.

(9) Fang, H.; Yang, J.; Wen, M.; Wu, Q. Nanoalloy Materials for Chemical Catalysis. *Adv. Mater.* **2018**, *30* (17). https://doi.org/10.1002/adma.201705698.

(10) Teoh, W. Y.; Amal, R.; Mädler, L. Flame Spray Pyrolysis: An Enabling Technology for Nanoparticles Design and Fabrication. *Nanoscale* **2010**, *2* (8), 1324–1347. https://doi.org/10.1039/c0nr00017e.

(11) Hübner, S.; de Vries, J. G.; Farina, V. Why Does Industry Not Use Immobilized Transition Metal Complexes as Catalysts? *Adv. Synth. Catal.* **2016**, *358* (1), 3–25. https://doi.org/10.1002/adsc.201500846.

(12) Schlögl, R. Preparation and Activation of the Technical Ammonia Synthesis Catalyst. In *Catalytic Ammonia Synthesis: Fundamentals and Practice*; Jennings, J. R., Ed.; Springer Science: New York, 1991; Vol. 1, pp 19–108. https://doi.org/10.1007/978-1-4757-9592-9_2.

(13) Swisher, J. H.; Jibril, L.; Petrosko, S. H.; Mirkin, C. A. Nanoreactors for Particle Synthesis. *Nat. Rev. Mater.* **2022**. https://doi.org/10.1038/s41578-021-00402-z.

(14) Petrosko, S. H.; Johnson, R.; White, H.; Mirkin, C. A. Nanoreactors: Small Spaces, Big Implications in Chemistry. *J. Am. Chem. Soc.* **2016**, *138* (24), 7443–7445. https://doi.org/10.1021/JACS.6B05393.

(15) Ferrando, R.; Jellinek, J.; Johnston, R. L. Nanoalloys: From Theory to Applications of Alloy Clusters and Nanoparticles. *Chemical Reviews*. 2008, pp 845–910. https://doi.org/10.1021/cr040090g.

(16) Cao, S.; Tao, F. F.; Tang, Y.; Li, Y.; Yu, J. Size- and Shape-Dependent Catalytic Performances of Oxidation and Reduction Reactions on Nanocatalysts. *Chemical Society Reviews*. 2016, pp 4747–4765. https://doi.org/10.1039/c6cs00094k.

(17) Bai, L.; Wang, X.; Chen, Q.; Ye, Y.; Zheng, H.; Guo, J.; Yin, Y.; Gao, C. Explaining the Size Dependence in Platinum-Nanoparticle-Catalyzed Hydrogenation Reactions. *Angew. Chemie Int. Ed.* **2016**, *55* (50), 15656–15661. https://doi.org/10.1002/anie.201609663.

(18) Hashmi, A. S. K.; Hutchings, G. J. Gold Catalysis. *Angewandte Chemie - International Edition*. December 4, 2006, pp 7896–7936. https://doi.org/10.1002/anie.200602454.

(19) Johnson, B. F. G. From Clusters to Nanoparticles and Catalysis. In *Coordination Chemistry Reviews*; Elsevier S.A., 1999; Vol. 190–192, pp 1269–1285. https://doi.org/10.1016/S0010-8545(99)00202-7.

(20) Huang, X.; Li, Y.; Li, Y.; Zhou, H.; Duan, X.; Huang, Y. Synthesis of PtPd Bimetal Nanocrystals with Controllable Shape, Composition, and Their Tunable Catalytic Properties. *Nano Lett.* **2012**, *12* (8), 4265–4270. https://doi.org/10.1021/nl301931m.

(21) Wang, C.; Van Der Vliet, D.; More, K. L.; Zaluzec, N. J.; Peng, S.; Sun, S.; Daimon, H.; Wang, G.; Greeley, J.; Pearson, J.; Paulikas, A. P.; Karapetrov, G.; Strmcnik, D.; Markovic, N. M.; Stamenkovic, V. R. Multimetallic Au/FePt3nanoparticles as Highly Durable Electrocatalyst. *Nano Lett.* **2011**, *11* (3), 919–926. https://doi.org/10.1021/nl102369k.

(22) Cheng, D.; Xu, H.; Fortunelli, A. Tuning the Catalytic Activity of Au–Pd Nanoalloys in CO Oxidation via Composition. *J. Catal.* **2014**, *314*, 47–55. https://doi.org/10.1016/J.JCAT.2014.03.017.

(23) Gawande, M. B.; Goswami, A.; Felpin, F.-X.; Asefa, T.; Huang, X.; Silva, R.; Zou, X.; Zboril, R.; Varma, R. S. Cu and Cu-Based Nanoparticles: Synthesis and Applications in Catalysis. *Chem. Rev.* **2016**, *116* (6), 3722–3811. https://doi.org/10.1021/acs.chemrev.5b00482.

(24) Aslam, U.; Chavez, S.; Linic, S. Controlling Energy Flow in Multimetallic Nanostructures for Plasmonic Catalysis. *Nat. Nanotechnol.* **2017**, *12* (10), 1000–1005. https://doi.org/10.1038/nnano.2017.131.

(25) Bai, S.; Bu, L.; Shao, Q.; Zhu, X.; Huang, X. Multicomponent Pt-Based Zigzag Nanowires as Selectivity Controllers for Selective Hydrogenation Reactions. *J. Am. Chem. Soc.* **2018**, *140* (27), 8384–8387. https://doi.org/10.1021/jacs.8b03862.

(26) Gutić, S. J.; Dobrota, A. S.; Fako, E.; Skorodumova, N. V.; López, N.; Pašti, I. A. Hydrogen Evolution Reaction-From Single Crystal to Single Atom Catalysts. *Catal. 2020, Vol. 10, Page 290* **2020**, *10* (3), 290. https://doi.org/10.3390/CATAL10030290.

(27) Yao, Q.; Lu, Z. H.; Wang, Y.; Chen, X.; Feng, G. Synergetic Catalysis of Non-Noble Bimetallic Cu-Co Nanoparticles Embedded in SiO2 Nanospheres in Hydrolytic Dehydrogenation of Ammonia Borane. *J. Phys. Chem. C* **2015**, *119* (25), 14167–14174. https://doi.org/10.1021/acs.jpcc.5b02403.

(28) Choi, S.-I.; Xie, S.; Shao, M.; Odell, J. H.; Lu, N.; Peng, H.-C.; Protsailo, L.; Guerrero, S.; Park, J.; Xia, X.; Wang, J.; Kim, M. J.; Xia, Y. Synthesis and Characterization of 9 Nm Pt–

Ni Octahedra with a Record High Activity of 3.3 A/Mg Pt for the Oxygen Reduction Reaction. *Nano Lett.* **2013**, *13* (7), 3420–3425. https://doi.org/10.1021/nl401881z.

(29) Bera, A.; Bhattacharya, A.; Tiwari, N.; Jha, S. N.; Bhattacharyya, D. Morphology, Stability, and X-Ray Absorption Spectroscopic Study of Iron Oxide (Hematite) Nanoparticles Prepared by Micelle Nanolithography. *Surf. Sci.* **2018**, *669*, 145–153. https://doi.org/10.1016/j.susc.2017.11.022.

(30) Hansen, T. W.; Delariva, A. T.; Challa, S. R.; Datye, A. K. Sintering of Catalytic Nanoparticles: Particle Migration or Ostwald Ripening? *Acc. Chem. Res.* **2013**, *46* (8), 1720–1730. https://doi.org/10.1021/ar3002427.

(31) Bonetto, R.; Crisanti, F.; Sartorel, A. Carbon Dioxide Reduction Mediated by Iron Catalysts: Mechanism and Intermediates That Guide Selectivity. *ACS Omega* **2020**, *5* (34), 21309–21319. https://doi.org/10.1021/ACSOMEGA.0C02786/ASSET/IMAGES/ACSOMEGA.0C02786.SOCIAL.JPEG_V03.

(32) Liu, L.; Corma, A. Metal Catalysts for Heterogeneous Catalysis: From Single Atoms to Nanoclusters and Nanoparticles. *Chem. Rev.* **2018**, *118* (10), 4981–5079. https://doi.org/10.1021/acs.chemrev.7b00776.

(33) Pal, B.; Mukherjee, S.; Sarma, D. D. Probing Complex Heterostructures Using Hard X-Ray Photoelectron Spectroscopy (HAXPES). *J. Electron Spectros. Relat. Phenomena* **2015**, *200*, 332–339. https://doi.org/10.1016/J.ELSPEC.2015.06.005.

(34) Sun, S. S.; Zeng, H. Size-Controlled Synthesis of Magnetite Nanoparticles. **2002**. https://doi.org/10.1021/JA026501X.

(35) Chen, Y.; Yang, D.; Yoon, Y. J.; Pang, X.; Wang, Z.; Jung, J.; He, Y.; Harn, Y. W.; He, M.; Zhang, S.; Zhang, G.; Lin, Z. Hairy Uniform Permanently Ligated Hollow Nanoparticles with Precise Dimension Control and Tunable Optical Properties. *J. Am. Chem. Soc.* **2017**, *139* (37), 12956–12967. https://doi.org/10.1021/jacs.7b04545.

(36) Xie, S.; Choi, S. Il; Xia, X.; Xia, Y. Catalysis on Faceted Noble-Metal Nanocrystals: Both Shape and Size Matter. *Current Opinion in Chemical Engineering*. Elsevier Ltd 2013, pp 142–150. https://doi.org/10.1016/j.coche.2013.02.003.

(37) Xu, X.; Zhang, X.; Sun, H.; Yang, Y.; Dai, X.; Gao, J.; Li, X.; Zhang, P.; Wang, H.-H.; Yu, N.-F.; Sun, S.-G.; Xu, X.; Zhang, X.; Sun, H.; Yang, Y.; Dai, X.; Gao, J.; Li, X.; Zhang, P.; Wang, H.; Yu, N.; Sun, S. G. Synthesis of Pt-Ni Alloy Nanocrystals with High-Index Facets and Enhanced Electrocatalytic Properties**. *Angew. Chem. Int. Ed* **2014**, *53*, 12522–12527. https://doi.org/10.1002/anie.201406497.

(38) Shan, S.; Li, J.; Maswadeh, Y.; O'Brien, C.; Kareem, H.; Tran, D. T.; Lee, I. C.; Wu, Z. P.; Wang, S.; Yan, S.; Cronk, H.; Mott, D.; Yang, L.; Luo, J.; Petkov, V.; Zhong, C. J. Surface Oxygenation of Multicomponent Nanoparticles toward Active and Stable Oxidation Catalysts. *Nat. Commun.* **2020**, *11* (1), 1–9. https://doi.org/10.1038/s41467-020-18017-3.

(39) Yang, X.; Chen, D.; Liao, S.; Song, H.; Li, Y.; Fu, Z.; Su, Y. High-Performance Pd–Au Bimetallic Catalyst with Mesoporous Silica Nanoparticles as Support and Its Catalysis of Cinnamaldehyde Hydrogenation. *J. Catal.* **2012**, *291*, 36–43. https://doi.org/10.1016/J.JCAT.2012.04.003.

(40) Cattaneo, S.; Freakley, S. J.; Morgan, D. J.; Sankar, M.; Dimitratos, N.; Hutchings, G. J. Cinnamaldehyde Hydrogenation Using Au-Pd Catalysts Prepared by Sol Immobilisation.

Catal. Sci. Technol. **2018**, *8* (6), 1677–1685. https://doi.org/10.1039/c7cy02556d.

(41) Cushing, B. L.; Kolesnichenko, V. L.; O'Connor, C. J. Recent Advances in the Liquid-Phase Syntheses of Inorganic Nanoparticles. *Chem. Rev.* **2004**, *104* (9), 3893–3946. https://doi.org/10.1021/cr030027b.

(42) Thanh, N. T. K.; Maclean, N.; Mahiddine, S. Mechanisms of Nucleation and Growth of Nanoparticles in Solution. *Chem. Rev.* **2014**, *114* (15), 7610–7630. https://doi.org/10.1021/CR400544S.

(43) Murray, C. B.; Sun, S.; Doyle, H.; Betley, T. Monodisperse 3d Transition-Metal (Co, Ni, Fe) Nanoparticles and Their Assembly into Nanoparticle Superlattices. *MRS Bull.* **2001**, *26* (12), 985–991. https://doi.org/10.1557/mrs2001.254.

(44) Chen, M.; Liu, J. P.; Sun, S. One-Step Synthesis of FePt Nanoparticles with Tunable Size. *J. Am. Chem. Soc.* **2004**, *126* (27), 8394–8395. https://doi.org/10.1021/ja047648m.

(45) Chen, M.; Kim, J.; Liu, J. P.; Fan, H.; Sun, S. Synthesis of FePt Nanocubes and Their Oriented Self-Assembly. *J. Am. Chem. Soc.* **2006**, *128* (22), 7132–7133. https://doi.org/10.1021/ja061704x.

(46) Rutledge, R. D.; Morris, W. H.; Wellons, M. S.; Gai, Z.; Shen, J.; Bentley, J.; Wittig, J. E.; Lukehart, C. M. Formation of FePt Nanoparticles Having High Coercivity. *J. Am. Chem. Soc.* **2006**, *128* (44), 14210–14211. https://doi.org/10.1021/ja0633868.

(47) Gilroy, K. D.; Ruditskiy, A.; Peng, H.-C.; Qin, D.; Xia, Y. Bimetallic Nanocrystals: Syntheses, Properties, and Applications. *Chem. Rev.* **2016**, *116* (18), 10414–10472. https://doi.org/10.1021/acs.chemrev.6b00211.

(48) Habas, S. E.; Lee, H.; Radmilovic, V.; Somorjai, G. A.; Yang, P. Shaping Binary Metal Nanocrystals through Epitaxial Seeded Growth. *Nat. Mater.* **2007**, *6* (9), 692–697. https://doi.org/10.1038/nmat1957.

(49) Wang, X.; Vara, M.; Luo, M.; Huang, H.; Ruditskiy, A.; Park, J.; Bao, S.; Liu, J.; Howe, J.; Chi, M.; Xie, Z.; Xia, Y. Pd@Pt Core–Shell Concave Decahedra: A Class of Catalysts for the Oxygen Reduction Reaction with Enhanced Activity and Durability. *J. Am. Chem. Soc.* **2015**, *137* (47), 15036–15042. https://doi.org/10.1021/jacs.5b10059.

(50) Jin, M.; Zhang, H.; Xie, Z.; Xia, Y. Palladium Concave Nanocubes with High-Index Facets and Their Enhanced Catalytic Properties. *Angew. Chemie Int. Ed.* **2011**, *50* (34), 7850–7854. https://doi.org/10.1002/anie.201103002.

(51) Shon, Y.-S.; Dawson, G. B.; Porter, M.; Murray, R. W. Monolayer-Protected Bimetal Cluster Synthesis by Core Metal Galvanic Exchange Reaction. *Langmuir* **2002**, *18* (10), 3880–3885. https://doi.org/10.1021/la025586c.

(52) Fenton, J. L.; Steimle, B. C.; Schaak, R. E. Tunable Intraparticle Frameworks for Creating Complex Heterostructured Nanoparticle Libraries. *Science (80-.).* **2018**, *360* (6388), 513–517. https://doi.org/10.1126/science.aar5597.

(53) Steimle, B. C.; Fenton, J. L.; Schaak, R. E. Rational Construction of a Scalable Heterostructured Nanorod Megalibrary. *Science (80-.).* **2020**, *367* (6476), 418–424. https://doi.org/10.1126/science.aaz1172.

(54) Davies, C. J.; Miedziak, P. J.; Brett, G. L.; Hutchings, G. J. Vinyl Chloride Monomer Production Catalysed by Gold: A Review. *Cuihua Xuebao/Chinese Journal of Catalysis*. Science Press October 1, 2016, pp 1600–1607. https://doi.org/10.1016/S1872-

2067(16)62482-8.

(55) Jiang, Q.; Ward, M. D. Crystallization under Nanoscale Confinement. *Chemical Society Reviews*. The Royal Society of Chemistry April 7, 2014, pp 2066–2079. https://doi.org/10.1039/c3cs60234f.

(56) Durán-Olivencia, M. A.; Lutsko, J. F. Mesoscopic Nucleation Theory for Confined Systems: A One-Parameter Model. *Phys. Rev. E - Stat. Nonlinear, Soft Matter Phys.* **2015**, *91* (2). https://doi.org/10.1103/PhysRevE.91.022402.

(57) Dai, Y.; Lu, P.; Cao, Z.; Campbell, C. T.; Xia, Y. The Physical Chemistry and Materials Science behind Sinter-Resistant Catalysts. *Chem. Soc. Rev.* **2018**, *47* (12), 4314–4331. https://doi.org/10.1039/c7cs00650k.

(58) Zhao, M.; Crooks, R. M. Homogeneous Hydrogenation Catalysis with Monodisperse, Dendrimer- Encapsulated Pd and Pt Nanoparticles. *Angew. Chemie - Int. Ed.* **1999**, *38* (3), 364–366. https://doi.org/10.1002/(SICI)1521-3773(19990201)38:3<364::AID-ANIE364>3.0.CO;2-L.

(59) Crooks, R. M.; Zhao, M.; Sun, L.; Chechik, V.; Yeung, L. K. Dendrimer-Encapsulated Metal Nanoparticles: Synthesis, Characterization, and Applications to Catalysis. *Acc. Chem. Res.* **2001**, *34* (3), 181–190. https://doi.org/10.1021/ar000110a.

(60) Shin, D. O.; Mun, J. H.; Hwang, G. T.; Yoon, J. M.; Kim, J. Y.; Yun, J. M.; Yang, Y. B.; Oh, Y.; Lee, J. Y.; Shin, J.; Lee, K. J.; Park, S.; Kim, J. U.; Kim, S. O. Multicomponent Nanopatterns by Directed Block Copolymer Self-Assembly. *ACS Nano* **2013**, *7* (10), 8899–8907. https://doi.org/10.1021/nn403379k.

(61) Hamley, I. W. Nanostructure Fabrication Using Block Copolymers. *Nanotechnology*. October 2003. https://doi.org/10.1088/0957-4484/14/10/201.

(62) Glass, R.; Möller, M.; Spatz, J. P. Block Copolymer Micelle Nanolithography. *Nanotechnology* **2003**, *14* (10), 1153–1160. https://doi.org/10.1088/0957-4484/14/10/314.

(63) Wang, L.; Min, H. L.; Barton, J.; Hughes, L.; Odom, T. W. Shape-Control of Protein Crystals in Patterned Microwells. *J. Am. Chem. Soc.* **2008**, *130* (7), 2142–2143. https://doi.org/10.1021/ja077956v.

(64) Barton, J. E.; Odom, T. W. Mass-Limited Growth in Zeptoliter Beakers: A General Approach for the Synthesis of Nanocrystals. *Nano Lett.* **2004**, *4* (8), 1525–1528. https://doi.org/10.1021/nl049151g.

(65) Monnier, V.; Sanz, N.; Botzung-Appert, E.; Bacia, M.; Ibanez, A. Confined Nucleation and Growth of Organic Nanocrystals in Sol-Gel Matrices. *J. Mater. Chem.* **2006**, *16* (15), 1401–1409. https://doi.org/10.1039/b509833p.

(66) McCaffrey, R.; Long, H.; Jin, Y.; Sanders, A.; Park, W.; Zhang, W. Template Synthesis of Gold Nanoparticles with an Organic Molecular Cage. *J. Am. Chem. Soc.* **2014**, *136* (5), 1782–1785. https://doi.org/10.1021/ja412606t.

(67) Tsukamoto, T.; Kambe, T.; Nakao, A.; Imaoka, T.; Yamamoto, K. Atom-Hybridization for Synthesis of Polymetallic Clusters. *Nat. Commun.* **2018**, *9* (1), 3873. https://doi.org/10.1038/s41467-018-06422-8.

(68) Chai, J.; Huo, F.; Zheng, Z.; Giam, L. R.; Shim, W.; Mirkin, C. A. Scanning Probe Block Copolymer Lithography. *Proc. Natl. Acad. Sci.* **2010**, *107* (47), 20202–20206.

https://doi.org/10.1073/pnas.1014892107.

(69) Liu, G.; Eichelsdoerfer, D. J.; Rasin, B.; Zhou, Y.; Brown, K. A.; Liao, X.; Mirkin, C. A. Delineating the Pathways for the Site-Directed Synthesis of Individual Nanoparticles on Surfaces. *Proc. Natl. Acad. Sci. U. S. A.* **2013**, *110* (3), 887–891. https://doi.org/10.1073/pnas.1220689110.

(70) Chen, P. C.; Liu, G.; Zhou, Y.; Brown, K. A.; Chernyak, N.; Hedrick, J. L.; He, S.; Xie, Z.; Lin, Q. Y.; Dravid, V. P.; O'Neill-Slawecki, S. A.; Mirkin, C. A. Tip-Directed Synthesis of Multimetallic Nanoparticles. *J. Am. Chem. Soc.* **2015**, *137* (28), 9167–9173. https://doi.org/10.1021/jacs.5b05139.

(71) Chen, P.-C.; Liu, X.; Hedrick, J. L.; Xie, Z.; Wang, S.; Lin, Q.-Y.; Hersam, M. C.; Dravid, V. P.; Mirkin, C. A. Polyelemental Nanoparticle Libraries. *Science* **2016**, *352* (6293), 1565–1569. https://doi.org/10.1126/science.aaf8402.

(72) Chen, P.-C.; Liu, M.; Du, J. S.; Meckes, B.; Wang, S.; Lin, H.; Dravid, V. P.; Wolverton, C.; Mirkin, C. A. Interface and Heterostructure Design in Polyelemental Nanoparticles. *Science* **2019**, *363* (6430), 959–964. https://doi.org/10.1126/science.aav4302.

(73) Huang, L.; Chen, P.-C.; Liu, M.; Fu, X.; Gordiichuk, P.; Yu, Y.; Wolverton, C.; Kang, Y.; Mirkin, C. A. Catalyst Design by Scanning Probe Block Copolymer Lithography. *Proc. Natl. Acad. Sci. U. S. A.* **2018**, *115* (15), 3764–3769. https://doi.org/10.1073/pnas.1800884115.

(74) Kluender, E. J.; Hedrick, J. L.; Brown, K. A.; Rao, R.; Meckes, B.; Du, J. S.; Moreau, L. M.; Maruyama, B.; Mirkin, C. A. Catalyst Discovery through Megalibraries of Nanomaterials. *Proc. Natl. Acad. Sci. U. S. A.* **2019**, *116* (1), 40–45.

https://doi.org/10.1073/pnas.1815358116.

(75) Du, J. S.; Chen, P.-C.; Meckes, B.; Xie, Z.; Zhu, J.; Liu, Y.; Dravid, V. P.; Mirkin, C. A. The Structural Fate of Individual Multicomponent Metal-Oxide Nanoparticles in Polymer Nanoreactors. *Angew. Chemie Int. Ed.* **2017**, *56* (26), 7625–7629. https://doi.org/10.1002/anie.201703296.

(76) Huo, F.; Zheng, Z.; Zheng, G.; Giam, L. R.; Zhang, H.; Mirkin, C. A. Polymer Pen Lithography. *Science (80-.).* **2008**, *321* (5896), 1658–1660. https://doi.org/10.1126/science.1162193.

(77) Giam, L. R.; He, S.; Horwitz, N. E.; Eichelsdoerfer, D. J.; Chai, J.; Zheng, Z.; Kim, D.; Shim, W.; Mirkin, C. A. Positionally Defined, Binary Semiconductor Nanoparticles Synthesized by Scanning Probe Block Copolymer Lithography. *Nano Lett.* **2012**, *12* (2), 1022–1025. https://doi.org/10.1021/nl204233r.

(78) Chen, P.-C.; Du, J. S.; Meckes, B.; Huang, L.; Xie, Z.; Hedrick, J. L.; Dravid, V. P.; Mirkin, C. A. Structural Evolution of Three-Component Nanoparticles in Polymer Nanoreactors. *J. Am. Chem. Soc.* **2017**, *139* (29), 9876–9884. https://doi.org/10.1021/jacs.7b03163.

(79) Brailsford, A. D.; Wynblatt, P. The Dependence of Ostwald Ripening Kinetics on Particle Volume Fraction. *Acta Metall.* **1979**, *27* (3), 489–497. https://doi.org/10.1016/0001-6160(79)90041-5.

(80) Wang, D.; Schaaf, P. Solid-State Dewetting for Fabrication of Metallic Nanoparticles and Influences of Nanostructured Substrates and Dealloying. *Phys. Status Solidi Appl. Mater. Sci.* **2013**, *210* (8), 1544–1551. https://doi.org/10.1002/pssa.201200895.

(81) Lee, M. H.; Huntington, M. D.; Zhou, W.; Yang, J. C.; Odom, T. W. Programmable Soft Lithography: Solvent-Assisted Nanoscale Embossing. *Nano Lett.* **2011**, *11* (2), 311–315. https://doi.org/10.1021/nl102206x.

(82) Roy, S.; Bandyopadhyay, D.; Karim, A.; Mukherjee, R. Interplay of Substrate Surface Energy and Nanoparticle Concentration in Suppressing Polymer Thin Film Dewetting. *Macromolecules* **2015**, *48*, 25. https://doi.org/10.1021/ma501262x.

(83) Roy, S.; Ansari, K. J.; Jampa, S. S. K.; Vutukuri, P.; Mukherjee, R. Influence of Substrate Wettability on the Morphology of Thin Polymer Films Spin-Coated on Topographically Patterned Substrates. *ACS Appl. Mater. Interfaces* **2012**, *4* (4), 1887–1896. https://doi.org/10.1021/am300201a.

(84) Efremov, V. A.; Potolokov, V. N.; Nikolashin, S. V.; Fedorov, V. A. Chemical Equilibria in Hydrolysis of Germanium Tetrachloride and Arsenic Trichloride. *Inorg. Mater.* **2002**, *38* (8), 847–853. https://doi.org/10.1023/A:1019743231095.

(85) Ambreen, S.; Pandey, N. D.; Mayer, P.; Pandey, A. Characterization and Photocatalytic Study of Tantalum Oxide Nanoparticles Prepared by the Hydrolysis of Tantalum Oxo-Ethoxide Ta 8 (μ 3-O) 2 (μ-O) 8 (μ-OEt) 6 (OEt) 14. *Beilstein J. Nanotechnol* **2014**, *5*, 1082–1090. https://doi.org/10.3762/bjnano.5.121.

(86) Gangadoo, S.; Stanley, D.; Hughes, R. J.; Moore, R. J.; Chapman, J. The Synthesis and Characterisation of Highly Stable and Reproducible Selenium Nanoparticles. *Inorg. Nano-Metal Chem.* **2017**, *47* (11), 1568–1576. https://doi.org/10.1080/24701556.2017.1357611.

(87) Kluth, G. J.; Sung, M. M.; Maboudian, R. Thermal Behavior of Alkylsiloxane Self-Assembled Monolayers on the Oxidized Si(100) Surface. *Langmuir* **1997**, *13* (14), 3775–

3780. https://doi.org/10.1021/la970135r.

(88) Cros, A. Charging Effects in X-Ray Photoelectron Spectroscopy. *J. Electron Spectros. Relat. Phenomena* **1992**, *59* (1), 1–14. https://doi.org/10.1016/0368-2048(92)85008-U.

(89) Moulder, J. F.; Chastain, J. *Handbook of X-Ray Photoelectron Spectroscopy : A Reference Book of Standard Spectra for Identification and Interpretation of XPS Data*; Physical Electronics Division, Perkin-Elmer Corp, 1992.

(90) Giermann, A. L.; Thompson, C. V. Solid-State Dewetting for Ordered Arrays of Crystallographically Oriented Metal Particles. *Appl. Phys. Lett.* **2005**, *86* (12), 121903. https://doi.org/10.1063/1.1885180.

(91) Henzie, J.; Lee, M. H.; Odom, T. W. Multiscale Patterning of Plasmonic Metamaterials. *Nat. Nanotechnol.* **2007**, *2* (9), 549–554. https://doi.org/10.1038/nnano.2007.252.

(92) Schindelin, J.; Arganda-Carreras, I.; Frise, E.; Kaynig, V.; Longair, M.; Pietzsch, T.; Preibisch, S.; Rueden, C.; Saalfeld, S.; Schmid, B.; Tinevez, J.-Y.; White, D. J.; Hartenstein, V.; Eliceiri, K.; Tomancak, P.; Cardona, A. Fiji: An Open-Source Platform for Biological-Image Analysis. *Nat. Methods* **2012**, *9* (7), 676–682. https://doi.org/10.1038/nmeth.2019.

(93) Gandhi, A. C.; Pradeep, R.; Yeh, Y.-C.; Li, T.-Y.; Wang, C.-Y.; Hayakawa, Y.; Wu, S. Y. Understanding the Magnetic Memory Effect in Fe-Doped NiO Nanoparticles for the Development of Spintronic Devices. *ACS Appl. Nano Mater.* **2018**, *2* (1), 278–290. https://doi.org/10.1021/ACSANM.8B01898.

(94) Al-Bustami, H.; Koplovitz, G.; Primc, D.; Yochelis, S.; Capua, E.; Porath, D.; Naaman, R.; Paltiel, Y. Single Nanoparticle Magnetic Spin Memristor. *Small* **2018**, *14* (30), 1801249.

https://doi.org/10.1002/SMLL.201801249.

(95) Nagesetti, A.; Rodzinski, A.; Stimphil, E.; Stewart, T.; Khanal, C.; Wang, P.; Guduru, R.; Liang, P.; Agoulnik, I.; Horstmyer, J.; Khizroev, S. Multiferroic Coreshell Magnetoelectric Nanoparticles as NMR Sensitive Nanoprobes for Cancer Cell Detection. *Sci. Reports 2017 71* **2017**, *7* (1), 1–9. https://doi.org/10.1038/s41598-017-01647-x.

(96) Wang, L.; Kafshgari, M. H.; Meunier, M. Optical Properties and Applications of Plasmonic-Metal Nanoparticles. *Adv. Funct. Mater.* **2020**, *30* (51), 2005400. https://doi.org/10.1002/ADFM.202005400.

(97) Yu-xi Zhang; Yu-hua Wang. Nonlinear Optical Properties of Metal Nanoparticles: A Review. *RSC Adv.* **2017**, *7* (71), 45129–45144. https://doi.org/10.1039/C7RA07551K.

(98) Aslam, U.; Rao, V. G.; Chavez, S.; Linic, S. Catalytic Conversion of Solar to Chemical Energy on Plasmonic Metal Nanostructures. *Nat. Catal. 2018 19* **2018**, *1* (9), 656–665. https://doi.org/10.1038/s41929-018-0138-x.

(99) Gao, D.; Arán-Ais, R. M.; Jeon, H. S.; Roldan Cuenya, B. Rational Catalyst and Electrolyte Design for CO2 Electroreduction towards Multicarbon Products. *Nat. Catal. 2019 23* **2019**, *2* (3), 198–210. https://doi.org/10.1038/s41929-019-0235-5.

(100) He, Y.; Liu, J.-C.; Luo, L.; Wang, Y.-G.; Zhu, J.; Du, Y.; Li, J.; Mao, S. X.; Wang, C. Size-Dependent Dynamic Structures of Supported Gold Nanoparticles in CO Oxidation Reaction Condition. *Proc. Natl. Acad. Sci. U. S. A.* **2018**, *115* (30), 7700–7705. https://doi.org/10.1073/pnas.1800262115.

(101) Li, T.; Yao, Y.; Huang, Z.; Xie, P.; Liu, Z.; Yang, M.; Gao, J.; Zeng, K.; Brozena, A. H.;

Pastel, G.; Jiao, M.; Dong, Q.; Dai, J.; Li, S.; Zong, H.; Chi, M.; Luo, J.; Mo, Y.; Wang, G.; Wang, C.; Shahbazian-Yassar, R.; Hu, L. Denary Oxide Nanoparticles as Highly Stable Catalysts for Methane Combustion. *Nat. Catal.* **2021**, *4* (1), 62–70. https://doi.org/10.1038/s41929-020-00554-1.

(102) Glasscott, M. W.; Pendergast, A. D.; Goines, S.; Bishop, A. R.; Hoang, A. T.; Renault, C.; Dick, J. E. Electrosynthesis of High-Entropy Metallic Glass Nanoparticles for Designer, Multi-Functional Electrocatalysis. *Nat. Commun.* **2019**, *10* (1). https://doi.org/10.1038/s41467-019-10303-z.

(103) Zhang, W.; Zhang, Z.-P.; Zhang, X.-E.; Li, F. Reaction inside a Viral Protein Nanocage: Mineralization on a Nanoparticle Seed after Encapsulation via Self-Assembly. *Nano Res.* **2017**, *10* (10), 3285–3294. https://doi.org/10.1007/S12274-017-1541-3.

(104) Lohmüller, T.; Aydin, D.; Schwieder, M.; Morhard, C.; Louban, I.; Pacholski, C.; Spatz, J. P. Nanopatterning by Block Copolymer Micelle Nanolithography and Bioinspired Applications. *Biointerphases* **2011**, *6* (1), MR1–MR12. https://doi.org/10.1116/1.3536839.

(105) Pang, X.; Zhao, L.; Han, W.; Xin, X.; Lin, Z. A General and Robust Strategy for the Synthesis of Nearly Monodisperse Colloidal Nanocrystals. *Nat. Nanotechnol.* **2013**, *8* (6), 426–431. https://doi.org/10.1038/nnano.2013.85.

(106) Tsukamoto, T.; Kuzume, A.; Nagasaka, M.; Kambe, T.; Yamamoto, K. Quantum Materials Exploration by Sequential Screening Technique of Heteroatomicity. *J. Am. Chem. Soc.* **2020**, jacs.0c06653. https://doi.org/10.1021/jacs.0c06653.

(107) Huang, L.; Lin, H.; Zheng, C. Y.; Kluender, E. J.; Golnabi, R.; Shen, B.; Mirkin, C. A. Multimetallic High-Index Faceted Heterostructured Nanoparticles. *J. Am. Chem. Soc.* **2020**,

142 (10), 4570–4575. https://doi.org/10.1021/jacs.0c00045.

(108) Wu, S.-H.; Tseng, C.-T.; Lin, Y.-S.; Lin, C.-H.; Hung, Y.; Mou, C.-Y. Catalytic Nano-Rattle of Au@hollow Silica: Towards a Poison-Resistant Nanocatalyst. *J. Mater. Chem.* **2011**, *21* (3), 789–794. https://doi.org/10.1039/C0JM02012E.

(109) Jiang, H. L.; Umegaki, T.; Akita, T.; Zhang, X. B.; Haruta, M.; Xu, Q. Bimetallic Au-Ni Nanoparticles Embedded in SiO2 Nanospheres: Synergetic Catalysis in Hydrolytic Dehydrogenation of Ammonia Borane. *Chem. - A Eur. J.* **2010**, *16* (10), 3132–3137. https://doi.org/10.1002/chem.200902829.

(110) Li, X.; Zheng, W.; Chen, B.; Wang, L.; He, G. Rapidly Constructing Multiple AuPt Nanoalloy Yolk@Shell Hollow Particles in Ordered Mesoporous Silica Microspheres for Highly Efficient Catalysis. *ACS Sustain. Chem. Eng.* **2016**, *4* (5), 2780–2788. https://doi.org/10.1021/ACSSUSCHEMENG.6B00260.

(111) Baldizzone, C.; Mezzavilla, S.; Carvalho, H. W. P.; Meier, J. C.; Schuppert, A. K.; Heggen, M.; Galeano, C.; Grunwaldt, J.-D.; Schüth, F.; Mayrhofer, K. J. J. Confined-Space Alloying of Nanoparticles for the Synthesis of Efficient PtNi Fuel-Cell Catalysts. *Angew. Chemie Int. Ed.* **2014**, *53* (51), 14250–14254. https://doi.org/10.1002/ANIE.201406812.

(112) Jiang, H.-L.; Umegaki, T.; Akita, T.; Zhang, X.-B.; Haruta, M.; Xu, Q. Bimetallic Au–Ni Nanoparticles Embedded in SiO2 Nanospheres: Synergetic Catalysis in Hydrolytic Dehydrogenation of Ammonia Borane. *Chem. – A Eur. J.* **2010**, *16* (10), 3132–3137. https://doi.org/10.1002/CHEM.200902829.

(113) Shaik, F.; Zhang, W.; Niu, W. A Generalized Method for the Synthesis of Ligand-Free M@SiO2 (M = Ag, Au, Pd, Pt) Yolk–Shell Nanoparticles. *Langmuir* **2017**, *33* (13), 3281–

3286. https://doi.org/10.1021/ACS.LANGMUIR.7B00141.

(114) Lin, C. H.; Chang, J. H.; Yeh, Y. Q.; Wu, S. H.; Liu, Y. H.; Mou, C. Y. Formation of Hollow Silica Nanospheres by Reverse Microemulsion. *Nanoscale* **2015**, *7* (21), 9614–9626. https://doi.org/10.1039/c5nr01395j.

(115) Jibril, L.; Chen, P.-C.; Hu, J.; Odom, T. W.; Mirkin, C. A. Massively Parallel Nanoparticle Synthesis in Anisotropic Nanoreactors. *ACS Nano* **2019**, *13* (11), 12408–12414. https://doi.org/10.1021/acsnano.9b05781.

(116) Xue, C.; Shi, X.; Tian, Y.; Zheng, X.; Hu, G. Diffusion of Nanoparticles with Activated Hopping in Crowded Polymer Solutions. *Nano Lett.* **2020**, *20* (5), 3895–3904. https://doi.org/10.1021/acs.nanolett.0c01058.

(117) Link, S.; El-Sayed, M. A. Spectral Properties and Relaxation Dynamics of Surface Plasmon Electronic Oscillations in Gold and Silver Nanodots and Nanorods. *J. Phys. Chem. B* **1999**, *103* (40), 8410–8426. https://doi.org/10.1021/jp9917648.

(118) Steed, J. W. First- and Second-Sphere Coordination Chemistry of Alkali Metal Crown Ether Complexes. *Coord. Chem. Rev.* **2001**, *215* (1), 171–221. https://doi.org/10.1016/S0010-8545(01)00317-4.

(119) Yoo, C.; Dodge, H. M.; Miller, A. J. M. Cation-Controlled Catalysis with Crown Ether-Containing Transition Metal Complexes. *Chem. Commun.* **2019**, *55* (35), 5047–5059. https://doi.org/10.1039/C9CC00803A.

(120) Knetsch, D.; Groeneveld, W. L. Alcohols as Ligands: Part IV. Complexes of Ethylene Glycol with Some Metal(II) Sulfates and Nitrates. *Recl. des Trav. Chim. des Pays-Bas* **1973**,

92 (8), 855–864. https://doi.org/10.1002/RECL.19730920807.

(121) Tuzovskaya, I.; Bogdanchikova, N.; Simakov, A.; Gurin, V.; Pestryakov, A.; Avalos, M.; Farías, M. H. Structure and Electronic States of Gold Species in Mordenites. *Chem. Phys.* **2007**, *338* (1), 23–32. https://doi.org/10.1016/J.CHEMPHYS.2007.07.026.

(122) Khullar, P.; Mahal, A.; Singh, V.; Banipal, T. S.; Kaur, G.; Bakshi, M. S. How PEO-PPO-PEO Triblock Polymer Micelles Control the Synthesis of Gold Nanoparticles: Temperature and Hydrophobic Effects. *Langmuir* **2010**, *26* (13), 11363–11371. https://doi.org/10.1021/LA100734P/SUPPL_FILE/LA100734P_SI_001.PDF.

(123) Shou, Q.; Guo, C.; Yang, L.; Jia, L.; Liu, C.; Liu, H. Effect of PH on the Single-Step Synthesis of Gold Nanoparticles Using PEO–PPO–PEO Triblock Copolymers in Aqueous Media. *J. Colloid Interface Sci.* **2011**, *363* (2), 481–489. https://doi.org/10.1016/J.JCIS.2011.07.021.

(124) Wexler, R. M.; Tsai, M. C.; Friend, C. M.; Muetterties, E. L. Pyridine Coordination Chemistry of Nickel and Platinum Surfaces. *J. Am. Chem. Soc.* **2002**, *104* (7), 2034–2036. https://doi.org/10.1021/JA00371A046.

(125) Shephard, G. S.; Thornton, D. A. Crystal Field Aspects of Vibrational Spectra: VII. Derivation of a Spectrochemical Series of Ligands from Infrared Spectra. *J. Mol. Struct.* **1976**, *34* (1), 83–91. https://doi.org/10.1016/0022-2860(76)80082-8.

(126) Uflyand, I. E.; Kokoreva, I. V.; Starikov, A. G.; Sheinker, V. N.; Pomogailo, A. D. Polymers Containing Metal Chelate Units. IV. Immobilised Complexes of Transition Metal Acrylates with 2,2′-Dipyridyl and 1,10-Phenanthroline. *React. Polym.* **1989**, *11* (C), 221–226. https://doi.org/10.1016/0923-1137(89)90107-3.

(127) Mrudula, M. S.; Tiwari, N.; Jha, S. N.; Bhattacharyya, D.; Nair, M. R. G. Structural Studies on Transition Metal Ion Complexes of Polyethylene Oxide-Natural Rubber Block Copolymers. *J. Polym. Res. 2019 268* **2019**, *26* (8), 1–16. https://doi.org/10.1007/S10965-019-1837-Y.

(128) Roach, J. D.; Bondaruk, M. M.; Al-Abdulghani, A.; Shahrori, Z.; Roach, J. D.; Bondaruk, M. M.; Al-Abdulghani, A.; Shahrori, Z. Counterion Binding in Aqueous Solutions of Poly(Vinylpyridines) as Assessed by Potentiometric Titration. *Adv. Mater. Phys. Chem.* **2016**, *6* (9), 249–261. https://doi.org/10.4236/AMPC.2016.69025.

(129) Laia, C. A. T.; Brown, W.; Almgren, M.; Costa, S. M. B. Light Scattering Study of Water-in-Oil AOT Microemulsions with Poly(Oxy)Ethylene. *Langmuir* **2000**, *16* (2), 465–470. https://doi.org/10.1021/la990684s.

(130) Behafarid, F.; Roldan Cuenya, B. Towards the Understanding of Sintering Phenomena at the Nanoscale: Geometric and Environmental Effects. *Top. Catal.* **2013**, *56* (15–17), 1542–1559. https://doi.org/10.1007/s11244-013-0149-4.

(131) Hoyt, J. J. *Phase Transformations*; McMaster Innovation Press: Hamilton, Canada, 2011; Vol. 1. https://doi.org/10.31399/asm.tb.lmcs.t66560029.

(132) Heveling, J. Heterogeneous Catalytic Chemistry by Example of Industrial Applications. *J. Chem. Educ.* **2012**, *89* (12), 1530–1536. https://doi.org/10.1021/ed200816g.

(133) Elhenawy, S.; Khraisheh, M.; AlMomani, F.; Hassan, M. Key Applications and Potential Limitations of Ionic Liquid Membranes in the Gas Separation Process of CO2, CH4, N2, H2 or Mixtures of These Gases from Various Gas Streams. *Mol. 2020, Vol. 25, Page 4274* **2020**, *25* (18), 4274. https://doi.org/10.3390/MOLECULES25184274.

(134) Seader, J. D. .; Henley, E. J. *Separation Process Principles*, 2nd ed.; Welter, J., McFadden, P., Eds.; John Wiley & Sons, Inc, 2012; Vol. 1.

(135) Umpierre, A. P.; Machado, G.; Fecher, G. H.; Morais, J.; Dupont, J. Selective Hydrogenation of 1,3-Butadiene to 1-Butene by Pd(0) Nanoparticles Embedded in Imidazolium Ionic Liquids. *Adv. Synth. Catal.* **2005**, *347* (10), 1404–1412. https://doi.org/10.1002/ADSC.200404313.

(136) Hicks, K. E.; Rosen, A. S.; Syed, Z. H.; Snurr, R. Q.; Farha, O. K.; Notestein, J. M. Zr6O8 Node-Catalyzed Butene Hydrogenation and Isomerization in the Metal−organic Framework NU-1000. *ACS Catal.* **2020**, *10* (24), 14959–14970. https://doi.org/10.1021/ACSCATAL.0C03579/SUPPL_FILE/CS0C03579_SI_002.ZIP.

(137) Yang, Q.; Hou, R.; Sun, K. Tuning Butene Selectivities by Cu Modification on Pd-Based Catalyst for the Selective Hydrogenation of 1,3-Butadiene. *J. Catal.* **2019**, *374*, 12–23. https://doi.org/10.1016/J.JCAT.2019.04.018.

(138) Kaiser, S. K.; Chen, Z.; Akl, D. F.; Mitchell, S.; Pérez-Ramírez, J. Single-Atom Catalysts across the Periodic Table. *Chem. Rev.* **2020**, *120* (21), 11703–11809. https://doi.org/10.1021/ACS.CHEMREV.0C00576.